



University of Florence

SCHOOL OF MATHEMATICAL, PHYSICAL AND NATURAL SCIENCES

Master Degree in Physics

MASTER THESIS

GENERATION OF ARBITRARY OPTICAL POTENTIALS FOR
ATOMIC PHYSICS EXPERIMENTS USING A DIGITAL
MICROMIRROR DEVICE

Advisor:
Dr. Jacopo Catani

Candidate:
Elia Perego
5525340

Contents

| | |
|---|------------|
| Introduction | iii |
| 1 Theoretical background | 1 |
| 1.1 Ytterbium | 1 |
| 1.2 Optical dipole potentials | 4 |
| 1.3 Standard optical lattices | 9 |
| 1.4 Mott insulating phase | 11 |
| 2 DMD characterization | 15 |
| 2.1 DMD properties | 15 |
| 2.2 Optical set-up | 27 |
| 2.3 Spatial filtering | 31 |
| 2.4 Diffraction limit of the optical set-up | 35 |
| 2.5 Optical trapping with a DMD | 36 |
| 3 Digitization of static patterns | 41 |
| 3.1 Dithering and error diffusion | 42 |
| 3.2 Flat-tops | 46 |
| 3.3 Lattices | 48 |
| 3.4 Selection of the best dithering algorithm | 52 |
| 4 Control program and feedback process | 57 |
| 4.1 "DMD Easy" | 57 |
| 4.2 Feedback process | 59 |
| 4.3 Calibration of the DMD on the CCD | 66 |
| 5 Static patterns applications in Atomic Physics | 69 |
| 5.1 Characterization parameters | 69 |
| 5.2 Flat-tops | 72 |
| 5.3 Lattices | 79 |
| 5.3.1 Lattice | 79 |
| 5.3.2 Top-Lattice | 84 |
| 5.4 Other patterns | 88 |
| 5.5 Observation of the Talbot effect | 92 |

| | | |
|----------|---|------------|
| 6 | Dynamic patterns applications in Atomic Physics | 95 |
| 6.1 | Stimulated Raman effect and Bragg scattering with a DMD . . . | 95 |
| 6.2 | DMD in quantum computing | 103 |
| | Summary and outlook | 107 |
| | Bibliography | 109 |

Introduction

In 1958, C. H. Townes and A. L. Schawlow submitted a paper about their theoretical calculations and considerations on a device which was able to emit coherent light through a process of optical amplification based on the stimulated emission of electromagnetic radiation, the *laser*. Lasers became rapidly a fundamental tool in many fields of the scientific research, allowing to achieve extraordinary advances in science as well as in technology.

Initially lasers were employed to probe atomic and molecular structures, but in the 1970s it was realized that they could be used as powerful tools to control and manipulate the motion of the atoms. Immediately these possibilities were investigated and new results were obtained beyond the spectroscopy, as the invention of *laser cooling*: through lasers, atoms can be slowed and cooled to very low temperatures, not accessible with the traditional cryogenic techniques. The realization of ultra-cold atomic gases has paved the way to unimaginable developments, such as Bose-Einstein condensates, quantum degenerate Fermi gases, stable and accurate atomic clocks and interferometers with matter waves, just to cite the most remarkable [16].

Moreover, it was discovered that laser light can be used to confine atoms in small potential traps. Periodical array of these traps can be arranged, creating *optical lattices*, whose applications in atomic physics are various. For instance, ultra-cold atoms trapped in such potentials closely resemble systems in condensed matter physics. From late 1970s, optical lattice potentials have been implemented in several ultra-cold atoms experiments [39]. Following, some applications of optical periodical structures and lattices in the atomic physics field are presented.

Atom diffraction As a light beam is diffracted by a grating, as a collimated beam of cooled atoms can be separated in several beams with quantized transverse momentum $p_{\perp} = 2n\hbar k$ (where n is an integer number and k the wave-vector of the standing-wave electric field) by light periodical structures. (Gould, Ruff, and Pritchard, 1896 [31], Arimondo, Lev, and Oka, 1979 [4], Grinchuk, Kuzin, Nagaeva, et al., 1981 [34], Moskowitz et al., 1983 [57] and Martin et al., 1988 [54]).

Atom interferometry On the basis of the atomic diffraction, atomic interferometers were built through the optical splitting of an initial atomic beam into two different ones, recombined at a later stage. (Rasel, Oberthaler, Batelaan, et al., 1995 [62], Giltner, McGowan, and Lee, 1995 [29] and Adams, Sigel, and Mlynek, 1994 [1] for a review).

Atom trapping Evidences of quantized motion of particles in periodical structures were observed in laser-cooled atoms in optical standing waves. (Verkerk et al., 1992 [65] and Jessen et al., 1992 [45]). In other experiments, atoms were cooled to very low temperatures (μK regime) in optical lattices. (Grynberg et al., 1993 [35], Hemmerich and Hänsch, 1993 [37] and Hemmerich et al., 1995 [38]). Thanks to the development of the *velocity-selective coherent population trapping*, temperatures below the sub-recoil limit have been reached with the technique of *Raman cooling*. (Aspect et al., 1988 [6] and Kasevich and Chu, 1992 [46]).

Solid-state models demonstration and quantum computation Recently the innovative techniques in the field of ultra-cold atoms have allowed for fine control and manipulation of the system hamiltonians in order to simulate the complex condensed-matter systems. As foreseen by R. Feynman (Feynman, 1982 [23]), the final aim for this kind of experiments would be the realization of *quantum simulators*. They are laboratory systems in which theories or models of great interest in modern physics, hardly solvable with classical computational methods, can be implemented and studied by measuring directly the properties of the system quantum states. (Lloyd, 1996 [53], while for a review of this approach, see Lewenstein, Sanpera, and Ahufinger, 2012 [51]). For example, with potential arrangements such as that provided by optical lattices, trapped atoms can simulate the behaviour of electrons in a perfectly periodical ions potential, revealing the energy band structure and demonstrating the existence of Bloch oscillations, first observed by C. Salomon. (Dahan et al., 1996 [17]).

With the possibility of creating a Bose-Einstein condensate (Anderson et al., 1995 [3]) of neutral atoms using evaporation cooling techniques (first achieved successfully by Masuhara et al., 1988 [55]), a new and different approach was introduced. A Bose-Einstein condensate (BEC) can be adiabatically transferred into an optical lattice without any further cooling process. This provides the starting point to study and investigate other solid-state physics systems, as tunnelling processes, Josephson dynamics, superfluidity and Bloch oscillations (Anderson and Kasevich, 1998 [2], Cataliotti et al., 2001 [13], Burger et al., 2001 [10] and Morsch et al., 2001 [56]).

Measurements of fundamental constants With the aid of moving optical lattices, fundamental physics constants – like the fine-structure constant

α , the Rydberg constant R_∞ or the ratio h/m for several atoms – can be determined with remarkably small uncertainties (for example, Bradley et al., 1999 [9] and Cladé, Mirandes, Cadoret, et al., 2006 [15]).

Optical lattices are usually created by a pair of counter-propagating laser beams, i. e. exploiting their interference as explained in details in Sec. 1.3. Nevertheless this method can hardly create dynamic or adjustable patterns, because their characteristics are mainly determined by the beams geometry which may not be easily modifiable, in most cases. Moreover, only certain kinds of patterns – the ones based on the interference profiles – can be obtained, so there is no freedom to choose and create any other figure. Furthermore, in spite of the possibilities provided by using superlattice techniques [27], the dynamic control of such patterns is quite limited.

The main goal of the present master thesis work is to investigate the possibility of realizing with a *Digital Micromirror Device* arbitrary, dynamic and easily interchangeable optical patterns to be employed in experiments of atomic physics.

Invented by L. Hornbeck and W. E. Nelson of Texas Instruments in 1987 [47], a Digital Micromirror Device (DMD) is a semiconductor-based "light switch" array, core of Digital Light Processing (DLP) projection technology [41]. This device is used in a variety of display applications, from traditional static to interactive displays and also in non-traditional applications including medical, security and industrial uses. Mainly, DLP technology is employed in front projectors and rear projection television; furthermore, the most part of digital cinema projectors are based on this technology [47]. Recently, several new applications for the DMD have been explored, like digital photofinishing, volumetric display, lithography, holography and data storage, microscopy and medical purposes, just to cite a few [19]. In this regard, in Zhu et al., 2012 [66], a DMD has been used to create a single-photon patterned optical stimulation of a zebrafish's neurons.

In general, the DMD is a kind of SLM, Spatial Light Modulator, a wider family of tools which impose some form, completely arbitrary, of spatially varying modulation on a incident beam of light. Another types of SLM are, for example, the Liquid Crystal on Silicon devices (LCoS). These devices present some notable differences and extra requirements with respect to the DMD. First of all, LCoS devices manipulate the Fourier Transform of the image to be created, while DMDs operate on the real image, directly modulating the electric field amplitude without involving any phase change. This allows an easier and more immediate implementation and use. Moreover, LCoS devices have a low damage threshold and a slower refresh rate between the projected patterns compared with DMDs [7]. For these reasons, in the present work a DMD has been preferred over a LCoS device.

Due to their ability to rapidly refresh the arbitrary patterns displayed, the Digital Micromirror Devices have already been implemented in atomic physics experiments. For example, in Ha et al., 2015 [36], the DMD is used in order to perform Bragg spectroscopy in order to probe a roton-maxon excitation spectrum in an interacting Bose-Einstein condensate in a 1-D shaken optical lattice, created by a couple of counter-propagating laser beams. Instead, in Fukuhara et al., 2013 [26], a DMD is implemented to achieve a simultaneous multiple-site addressing on arrays of parallel 1-D Mott insulators created by rubidium-87 atoms trapped in periodical optical potentials. In Bellem, 2011 [7], the DMD is exploited to perform multi-site addressing and study single-spin impurity dynamics.

With this in mind, this master thesis work examines the possibility of manipulating the intensity profile of a laser beam through a Digital Micromirror Device in order to achieve, both static and dynamic, arbitrary optical potentials to be projected on ultra-cold atoms. Such an opportunity would allow for several different implementations in atomic physics experiments. First of all, "non-gaussian" static potentials could be created: this means that the original intensity profile – usually of gaussian shape – of a laser beam could be corrected. Moreover, one- and two-dimensional arrangements of optical trapping potentials could be achieved (without the superimposition of the previous laser beam intensity profile shape), opening the door to interesting utilizations in lattice physics. In the end, a dynamic control of arbitrary moving patterns would provide a powerful tool for directly manipulating the projected optical potentials, allowing for a new series of applications in cutting-edge experimental physics fields, as quantum simulation and quantum computation.

Outline

In the first chapter, the main features of Ytterbium atoms are reported along with the theoretical principles of the dipole forces arising from the interaction between the atoms and an optical radiation and the standard methods for realizing optical lattices. The theoretical framework of the Mott insulator phase is presented too.

The second chapter is devoted to the main characteristics of the Digital Micromirror Device model used during this work, the optical set-up implemented in order to test the device, the experimental procedure for realizing a spatial filtering of the images, the diffraction limits of the experimental set-up and some considerations about the possibility of creating trapping lattices for Yb atoms with the DMD.

Dithering processes and the digitization algorithms applied to the patterns

in order to obtain one-bit images to be projected by the DMD are explained in the third chapter.

In the fourth chapter, the control program designed during this work, "DMD Easy", is described along with the feedback process, developed in order to improve the images quality and obtain a better overlap with the target patterns projected by the DMD.

Chapter five shows some experimental images of some static patterns (Flat-Tops and lattices among the others) projected by the DMD and corrected by the feedback mechanism. Their quantitative characterization is given as well.

In the sixth chapter, some applications of dynamic patterns projected by the DMD, as the stimulated Raman effect and the Bragg scattering, are discussed. The possibility of realizing quantum registers and gates are investigated too. Eventually, experimental evidences of the Talbot effect are reported.

Chapter 1

Theoretical background

The work presented in this master thesis has been developed as a part of a wider experiment running at LENS (Florence), whose goal, among others, is to implement quantum computation techniques with ultra-cold neutral Ytterbium atoms. A "quantum computer" is a system able to perform operations on data exploiting quantum-mechanical effects such as state superposition and entanglement [58]. The realization of a quantum computer requests a series of requirements, as the possibility to trap atoms and the existence of two stable states characterized by a long coherence, which can be satisfied by the peculiar features of Ytterbium, as explained in the first section of this chapter. Moreover, atoms need to be confined in well-defined space arrangements without spoiling the states coherence. In order to perform this task, optical dipole potential induced by an external electromagnetic radiation – as described in the second section – is exploited to create "optical lattices" via a standard technique presented in the third section of this chapter. Provided some conditions – reported in the fourth section – are satisfied, single Ytterbium atoms can be trapped in single sites of such periodical potentials, realizing a prime candidate system for quantum information and computation purposes.

1.1 Ytterbium

Ytterbium is a rare-earth metal having atomic number 70, atomic weight 173.054 amu and several stable bosonic and fermionic isotopes. Its electronic configuration is $[\text{Xe}] 4f^{14} 6s^2$ with two electrons in the most external orbital, so its energetic levels structure – presented in Fig. 1.1 – is very similar to the Helium and the alkaline-earth elements ones, like Calcium. Its levels scheme can be divided into two branches, singlet and triplet, having total spin angular momenta $S = 0$ and $S = 1$, respectively, as shown in the Grotrian diagram along with some relevant transitions [11] following explained.

- $^1S_0 \rightarrow ^1P_1$ (398.9 nm, $\Gamma = 2\pi \cdot 28.9$ MHz) It is an allowed transition

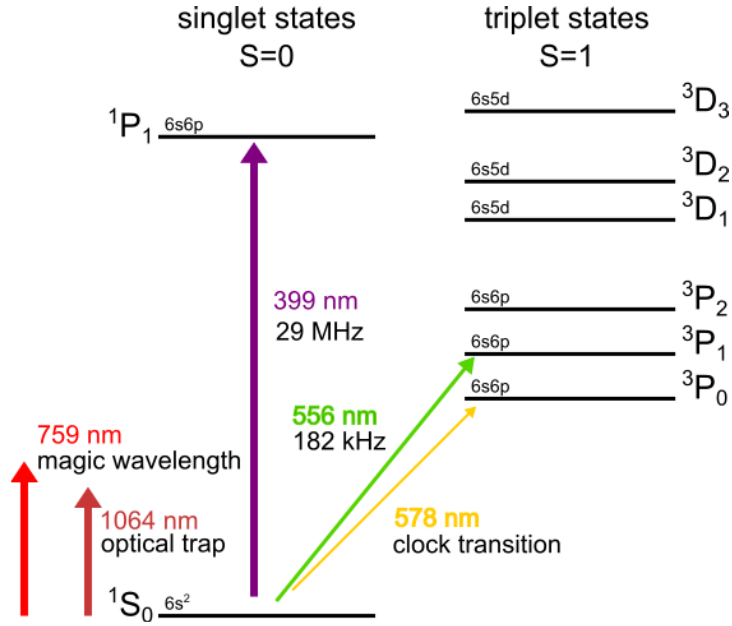


Figure 1.1: Ytterbium Grotrian diagram.

in the electric dipole approximation, characterized by a short mean lifetime (5.5 ns). In the experiments, this transition is employed in a first cooling step of the atoms with the aid of a Zeeman Slower [59].

- $1S_0 \rightarrow 3P_1$ (556 nm, $\Gamma = 2\pi \cdot 182$ kHz) It is an inter-combination transition because it violates the $\Delta S = 0$ selection rule of spin conservation, which is carefully respected in the LS coupling approximation, i. e. if the spin-orbit term in the atomic hamiltonian is negligible with respect to the Coulomb repulsion one. However, this condition is no more verified if the atomic number is much larger than 30: yet in this case, the two terms have comparable magnitude, so S can not be considered a good quantum number any more. Thus, the selection rule is not so rigorous as in the other case and the transition becomes weakly allowed. For Ytterbium atoms, the mean lifetime of the $3P_1$ state is 850 ns. This transition is used for trapping the atoms in a magneto-optical trap (MOT).
- $1S_0 \rightarrow 3P_0$ (578,42 nm, $\Gamma \simeq 2\pi \cdot 10$ mHz) It is a doubly forbidden transition because it violates both the $\Delta S = 0$ selection rule – as the previous one – and the total orbital angular momentum (J) conservation, which would not allow the transition $J_i = 0 \rightarrow J_f = 0$. Still, in fermionic isotopes of Ytterbium, this transition is very weakly allowed due to the level mixing with upper manifolds: actually its mean lifetime has been measured to be about 20 s, so it can be considered stable within

the experimental time-scale. The fermionic isotopes actually own an hyperfine structure which makes J not a good quantum number any more and, consequently, the total angular momentum conservation a "less prohibitive" rule. The bosonic isotopes have not any hyperfine structure because their nuclear spin I vanishes. Nevertheless, applying a constant magnetic field, it is possible to mix the 3P_0 state with the 3P_1 one, making the former accessible as well from the 1S_0 ground state. In these cases, the transition to the 3P_0 state would be slightly allowed, having a linewidth which depends on the external magnetic field magnitude and on the exciting radiation intensity. This transition is generally known as clock transition. (Poli et al., 2008 [61] and Lemke et al., 2009 [50]).

Ytterbium, as the other alkaline-earth-like and alkaline-earth atomic species, is an interesting candidate to address challenges in quantum computing (see Sec. 6.2) with neutral atoms due to its peculiar characteristics, mainly arising from the singlet-triplet levels configuration and the richness of the levels structure [18], described following.

First of all, Ytterbium has an energy structure particularly stable against the external magnetic perturbations which would easily shift the energy levels bringing undesired decoherence into the system.

The hamiltonian which describes the interaction between the atomic system and a magnetic field \mathbf{B} is

$$\mathcal{H} = -\hat{\boldsymbol{\mu}} \cdot \mathbf{B} \quad (1.1)$$

where the magnetic dipole momentum operator $\hat{\boldsymbol{\mu}}$ is given by

$$\hat{\boldsymbol{\mu}} = -\frac{\mu_B}{\hbar} \hat{\mathbf{L}} - g_S \frac{\mu_B}{\hbar} \hat{\mathbf{S}} + g_I \frac{\mu_N}{\hbar} \hat{\mathbf{I}} \quad (1.2)$$

where $\hat{\mathbf{L}}$ is the orbital angular momentum operator, $\hat{\mathbf{S}}$ the spin angular momentum operator, $\hat{\mathbf{I}}$ the nuclear spin angular momentum operator, $\mu_B = e\hbar/2m_e$ the Bohr magneton, $\mu_N \simeq \mu_B/2000$ the nuclear magneton, g_S the electron gyromagnetic factor and g_I the nuclear Landé factor.

The ground state 1S_0 and the metastable one 3P_0 have both a zero total orbital angular momentum J , so the first contribution in Eq. 1.2 is null. Bosonic isotopes – which have also nuclear momentum $I = 0$ – in the ground state are not influenced at all by external magnetic fields. For bosonic atoms in the metastable state, there is only the electronic spin contribution. The same holds for fermionic isotopes, although the nuclear spin contribution has to be taken into account: actually they have nuclear momentum not-null – $I = 1/2$ for ^{171}Yb and $I = 5/2$ for ^{173}Yb –, but the corresponding energy

1. Theoretical background

shift due to magnetic fields is a factor of 2000 lower than for alkalis because of the small coupling constant μ_N .

Hence, one could expect that Ytterbium shows a light rejection to spurious magnetic fields fluctuations, avoiding detrimental decoherence processes of the levels.

Second, Ytterbium clock transition provides a meta-stable state (3P_0) with a mean lifetime of tens of seconds. Therefore it can be considered as an "extra" ground state, in addition to the 1S_0 state. The existence of two stable and addressable states during the typical experimental time-scale is a requirement for quantum computing: actually, data can be encoded by localized atoms populating these two different states (see Sec. 6.2).

Third, Ytterbium has a so-called "magic wavelength" in an accessible spectrum range, 759 nm. In order to trap atoms, the dipole force exerted by an external light field is employed, so the consequent light shift of the energy levels must be considered. However certain wavelengths, called magic, have the characteristic of performing the same energy shift for two different states. In the case of Ytterbium these are the 1S_0 and the 3P_0 states. This means that the system constituted by those two levels evolves coherently if it is trapped in such potential.

1.2 Optical dipole potentials

The interaction between an electromagnetic wave and the atomic energy levels generates an optical dipole potential which can be employed in order to trap or confine ultra-cold atomic gases.

In the following treatment of this phenomenon, a two-levels atom has been considered for simplicity. Afterwards, the results will be generalized for more realistic multi-level atoms.

A two-levels system is composed by two states: the "ground state" described

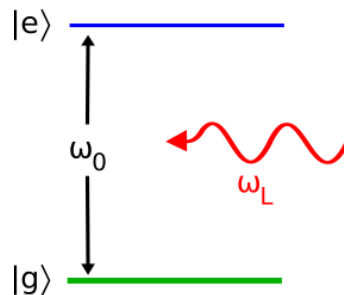


Figure 1.2: Two-levels system scheme.

by the wave function $|g\rangle$ with energy $E_g = 0$ and the excited state $|e\rangle$ with

energy $E_e = \hbar\omega_0$ as can be seen in Fig. 1.2. A generic state of this system is given by a superposition of those two states

$$\psi = a_g|g\rangle + a_e|e\rangle \quad (1.3)$$

where a_g and a_e are two complex coefficients such that $|a_g|^2 + |a_e|^2 = 1$. In order to solve this problem, the density matrix operator will be used, defined as follows

$$\hat{\rho} = |\psi\rangle\langle\psi| = \begin{pmatrix} |a_g|^2 & a_e^*a_g \\ a_g^*a_e & |a_e|^2 \end{pmatrix} \quad (1.4)$$

where the diagonal elements represent the probability to find an atom in a level (ground or excited), while the off-diagonal elements the coupling strength of the levels.

In general, neutral atoms can interact with light in both dissipative and conservative way: the first kind of interaction can be used to cool the atoms down to a μK regime, whereas the latter can be employed to create conservative trapping potential.

When an atom is immersed in a laser light field, the oscillatory electrical field (Eq. 1.5) induces an atomic electric dipole moment \mathbf{D} .

$$\mathbf{E}_L(\mathbf{r}, t) = \boldsymbol{\varepsilon}_L(\mathbf{r}) E_L(\mathbf{r}) \cos(\omega_L t + \phi(\mathbf{r})) \quad (1.5)$$

where $\boldsymbol{\varepsilon}_L(\mathbf{r})$ is the polarization vector, $E_L(\mathbf{r})$ is the field amplitude, ω_L the laser angular frequency (also called pulsation) and $\phi(\mathbf{r})$ its phase.

The dipole moment \mathbf{D} oscillates at the same frequency $\nu_L = \omega_L/2\pi$ of \mathbf{E}_L and with amplitude given by

$$\mathbf{D} = \alpha(\omega_L)\mathbf{E} \quad (1.6)$$

where $\alpha(\omega_L)$ is the atomic polarizability, which depends on the pulsation ω_L .

In the density matrix frame, the electric dipole moment \mathbf{D} can be expressed as the expectation value of the electric dipole operator $\hat{\mathbf{d}} = -e\hat{\mathbf{r}}$ on the state described by the density matrix

$$\begin{aligned} \mathbf{D} &= \text{Tr}[\hat{\rho}\hat{\mathbf{d}}] \\ &= -e(\rho_{eg}\mathbf{d}_{ge} + \rho_{ge}\mathbf{d}_{eg}) \\ &= -e\left(\tilde{\rho}_{eg}\mathbf{d}_{ge}e^{-i\omega_L t} + \tilde{\rho}_{ge}\mathbf{d}_{eg}e^{i\omega_L t}\right) \end{aligned} \quad (1.7)$$

where in the last passage the rotating-wave approximation has been invoked, which consists in taking into account only the near resonant terms of the electric field in the description of the interaction between atoms and

1. Theoretical background

radiation [25]. Actually, an external linearly polarized electric field can be decomposed into two counter-rotating circularly polarized fields. Through an opportune reference frame change, a phase with a pulsation equal to ω_L can be added to a_e , as shown in Eq. 1.8. In this rotating reference frame, one of the external field becomes quasi-static if the laser beam is quasi-resonant with transition frequency, while the frequency of the other field $-(\omega_L + \omega_0)$ is doubled, hence its contribution is neglected because atoms are not influenced by electric field oscillations with such a fast frequency.

$$\begin{cases} \tilde{a}_g = a_g \\ \tilde{a}_e = a_e e^{i\omega_L t} \end{cases} \quad (1.8)$$

At this point, an explicit expression of $\tilde{\rho}_{ge} = \tilde{a}_e^* \tilde{a}_g$ is requested: it can be obtained by solving the optical Bloch equations (see Cohen-Tannoudji and Guéry-Odelin, 2011 [16]). The optical Bloch equations, also known as Maxwell-Bloch equations, describe the dynamics of a two-state quantum system interacting with an monochromatic electromagnetic radiation providing the temporal variations of the two coherences and the population difference between the two states $|g\rangle$ and $|e\rangle$.

Hence $\tilde{\rho}_{eg}$ can be expressed as follows

$$\tilde{\rho}_{eg} = \tilde{\rho}_{ge}^* = \frac{\Omega}{2} \frac{\delta - i\frac{\Gamma}{2}}{\delta^2 + \frac{\Gamma^2}{4} + \frac{|\Omega|^2}{2}} \quad (1.9)$$

where $\Omega = \mathbf{d}_{eg} \cdot \boldsymbol{\varepsilon}(\mathbf{r}) \mathbf{E}_L(\mathbf{r}) / \hbar$ is the Rabi frequency, $\delta = \omega_L - \omega_0$ is the detuning between the laser and atomic resonance frequencies and

$$\Gamma = \frac{\omega_0^3}{3\pi\epsilon_0\hbar c^3} d_{eg}^2 \quad (1.10)$$

is the radiative decay rate. Therefore the electric dipole moment can be rewritten as following

$$\mathbf{D} = -\frac{e^2 d_{ge}^2}{\hbar} \frac{\delta - i\frac{\Gamma}{2}}{\delta^2 + \frac{\Gamma^2}{4} + \frac{|\Omega|^2}{2}} \frac{\mathbf{E}}{2} e^{-i\omega_L t} + h.c. \quad (1.11)$$

where the transition dipole moment is supposed to be parallel to the external electric field.

Thus, comparing the expression for $\mathbf{E}_L(\mathbf{r}, t)$ and with Eq. 1.6, the atomic polarizability turns out to be

$$\alpha(\omega_L) = -\frac{e^2 d_{ge}^2}{\hbar} \frac{\delta - i\frac{\Gamma}{2}}{\delta^2 + \frac{\Gamma^2}{4} + \frac{|\Omega|^2}{2}} \quad (1.12)$$

Now, with the analytic expression of the atomic polarizability, the electric dipole moment can be calculated from the external field applied. Moreover,

the induced electric dipole moment interacts in turn with \mathbf{E} . The resulting dipole potential energy is given by the equation Eq. 1.13.

$$V_{\text{dip}}(\mathbf{r}) = -\frac{1}{2} \langle \mathbf{D} \cdot \mathbf{E} \rangle = -\frac{1}{2\epsilon_0 c} \text{Re}(\alpha) I(\mathbf{r}) \quad (1.13)$$

where the mean is intended over time and the $1/2$ extra factor is due to the fact that the electric dipole is induced by the same electric field with which interacts.

Substituting Eqs. 1.10 and 1.12 in Eq. 1.13, an expression for the dipole potential energy can be obtained in far-off resonance approximation¹

$$V_{\text{dip}}(\mathbf{r}) = \frac{3\pi c^2}{2\omega_0^3} \left(\frac{\Gamma}{\delta} \right) I(\mathbf{r}) \quad (1.14)$$

from which it can be noticed the explicit dependence of the potential nature from the detuning sign: for so-called red detuning ($\delta < 0$), the dipole potential energy is negative, so the atoms will tend to be trapped in the intensity maxima. Other treatments can be found in Grimm and Weidemüller, 2000 [33] or in Cohen-Tannoudji and Guéry-Odelin, 2011 [16].

"Dressed states" picture The dipole potential energy can be described also with an alternative (but equivalent under certain approximations) representation in which the atom structure and the electrical field are considered together [32]. The energy in the ground and excited states of the system are

$$\begin{cases} E_g = n\hbar\omega_L \\ E_e = (n-1)\hbar\omega_L + \hbar\omega_0 = -\hbar\delta + n\hbar\omega_L \end{cases} \quad (1.15)$$

where n is the photons number of the quantized field and the internal ground state energy is assumed to be null. The energy shift due to the external perturbation can be evaluated with the second order perturbation theory: for non-degenerate states, the corrections are

$$\Delta E_i = \sum_{j \neq i} \frac{|\langle j | \mathcal{H} | i \rangle|^2}{E_i - E_j} \quad (1.16)$$

where $\mathcal{H} = -\hat{\mathbf{d}} \cdot \mathbf{E}$ with $\hat{\mathbf{d}}$ is the electric dipole operator $\hat{\mathbf{d}} = -e\hat{\mathbf{r}}$. This energy shift is often called "light-shift" or "AC-Stark shift".

For a two-levels system, the numerator is simply $|d_{eg}|^2 |\mathbf{E}|^2$, which can be rewritten as a function of Γ via Eq. 1.10. The denominator is instead

¹In the far-off resonance approximation the detuning δ is considered larger than the radiative linewidth Γ and the Rabi frequency Ω .

1. Theoretical background

$$\begin{aligned}
\pm (E_g - E_e) &= \pm \hbar (\omega_g - \omega_e) \\
&= \pm \hbar (\omega_g - \omega_e + \omega_L) \\
&= \pm \hbar (\omega_L - \omega_0) \\
&= \pm \hbar \delta
\end{aligned} \tag{1.17}$$

where the rotating-wave approximation has been taken into account. Therefore, for the ground state, the light-shift yields

$$\Delta E_g = \frac{|d_{eg}|^2 |\mathbf{E}|^2}{\hbar \delta} = \frac{3\pi c^2}{2\omega_0^3} \left(\frac{\Gamma}{\delta} \right) I(\mathbf{r}) \tag{1.18}$$

where $I(\mathbf{r}) = c\epsilon_0 |E(\mathbf{r})|^2 / 2$ and Eq. 1.10 have been used.

This result is in full agreement with the one obtained previously.

The "dressed states" picture can be particularly useful if a multi-level atom is taken into account. In this case, all the transitions from the ground state $|g\rangle$ to the excited levels $|i\rangle$ have to be considered in Eq. 1.16. The energy shift for the ground state can be expressed as

$$\Delta E_g = \sum_{i \neq g} \frac{|\langle i | \mathcal{H} | g \rangle|^2}{E_i - E_g} = \sum_{i \neq g} \frac{\hbar |\Omega_i|^2}{4(\omega - \omega_{ig})} \tag{1.19}$$

where $|i\rangle$ is an unperturbed state of the atomic hamiltonian having energy E_i , Ω_i are the Rabi frequencies for the transitions connecting the ground state to the i -th excited state with an associated energy $\hbar\omega_{ig}$.

Regarding Ytterbium atoms, the atomic polarizability can be evaluated with Eq. 1.12 for the magic wavelength 759 nm. The proportional constant $C(\omega_L)$ between V_{dip} and I ,

$$V_{\text{dip}}(\mathbf{r}) = C(\omega_L) I(\mathbf{r}) \tag{1.20}$$

can be calculated with no RWA and taking into account the nearest transitions², as follows

$$C(\omega_L) = \sum_i \frac{3\pi c^2}{2\omega_i^3} \left(\frac{\Gamma_i}{\omega_i - \omega_L} + \frac{\Gamma_i}{\omega_i + \omega_L} \right) \tag{1.21}$$

where the index i runs over the atomic transitions.

If $I(\mathbf{r})$ is expressed in Watt/cm² and $V_{\text{dip}}(\mathbf{r})$ is desired in nK ,

²The transitions between the ground state $6s^2 \ ^1S_0$ and the following states have been considered: $6s6p \ ^3P_1$, $6s6p \ ^1P_1$, $(7/2, 5/2) \ j = 1$, $6s7p \ ^1P_1$ and $6s8p \ ^1P_1$.

$$V[\text{nK}] = 0.4 I[\text{W}/\text{cm}^2] \quad (1.22)$$

This means that the depth of an optical potential created by a laser beam having waist $w_L = 150 \mu\text{m}$, an overall power $P = 500 \text{ mW}$ and wavelength $\lambda = 759 \text{ nm}$ is 572 nK in case of Ytterbium atoms.

When an atom is placed into a light field having a non-uniform spatial intensity profile, it undergoes an optical dipole force which arises from the conservative optical dipole potential expressed by Eq. 1.14.

$$F_{\text{dip}}(\mathbf{r}) = -\nabla V_{\text{dip}}(\mathbf{r}) = \frac{3\pi c^2}{2\omega_0^3} \left(\frac{\Gamma}{\delta} \right) \nabla I(\mathbf{r}) \quad (1.23)$$

This force can be used to manipulate the atomic motion or to confine neutral atoms: actually, a common application of F_{dip} is the far-off resonance trap (FORT) in which the atoms can be stored for several seconds practically without heating effects due to the spontaneous fluorescence scattering. In this sense, the first successful optical trapping was obtained by S. Chu and co-workers [5].

For red detuning, the potential minima correspond to the intensity maxima, which can be achieved in a very simple way with a focused laser beam with a frequency lower than ω_0 , for example.

For a TEM₀₀ gaussian beam, the maximum of the intensity is reached on the propagation axis at the beam waist³. Therefore, the dipole force will be more attractive in that point: the atoms will be forced to stay along the beam propagation axis, in proximity of the beam waist [39]. Similarly, with two orthogonal laser beams crossed in their waists, a FORT in which the atoms are trapped in the crossing area can be implemented. Fig. 1.3 shows the trapping geometries described.

1.3 Standard optical lattices

By exploiting the FORT scheme, many different kinds of trapping potentials can be created through the interference between several coherent laser beams. In the simplest geometry, two laser beams with the same polarization can cross forming an angle θ between the beams axes, as shown in Fig. 1.3. In this configuration, the spatial intensity modulation due to the interference (represented in Fig. 1.4) is given by

$$d = \frac{\lambda}{2 \sin(\theta/2)} \quad (1.24)$$

1. Theoretical background

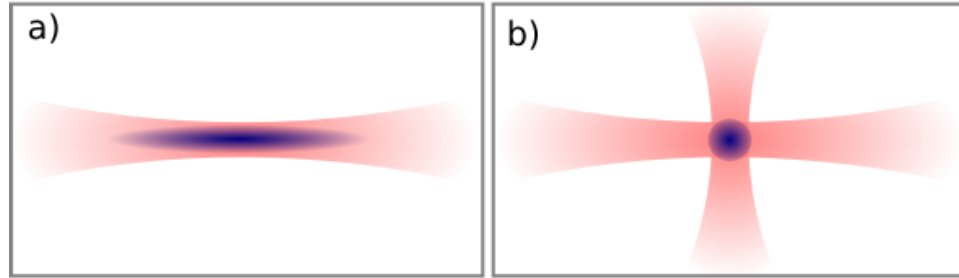


Figure 1.3: Optical dipole force, arising from the interaction between the atoms and the optical radiation, traps atoms where the intensity is higher (in case of red detuning). a) Gaussian laser beam, red-detuned with respect to the trapping atomic transition, confines atoms along its axis at its waist. b) Pair of gaussian laser beams: the atoms are confined in the crossing area.

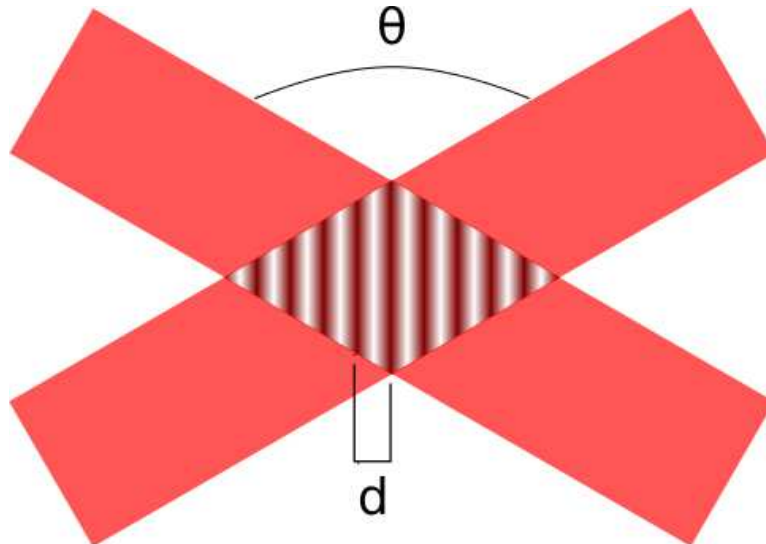


Figure 1.4: Interference pattern created by two crossed laser beams.

If the two beams were counter-propagating (or if only one laser beam incident normally on a mirror were made interfere with itself), the interference fringes would be separated by a length $d = \lambda/2$.

Exploiting this phenomenon, periodical arrangements, called "optical lattices", of trapping potentials can be achieved by using couples of counter-propagating laser beams, as shown in Fig. 1.5. In the frame a), a 1-D optical lattice is shown: ultra-cold atoms loaded into this kind of potentials are organized in parallel planes, orthogonal with respect to the beams axes. In the frame b), two couples of counter-propagating laser beams form a 2-D optical lattice where the loaded atoms are arranged in wires. The frame c) of

³See Sec. 4.2 for further details on the gaussian beam intensity profile.

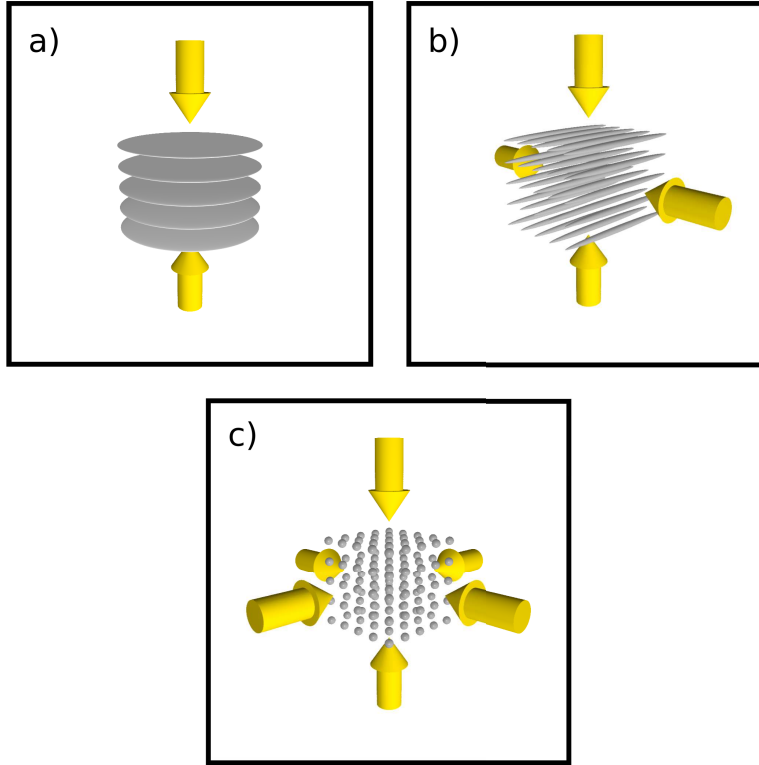


Figure 1.5: Optical lattices in one dimension a), two dimensions b) and three dimensions c). Courtesy of L. Fallani.

Fig. 1.5 reports three couples of beams which create a periodical trapping potential along the three dimensions where cooled atoms are confined in an optical arrangement. It can simulate, for example, the behaviour of electrons moving in an ionic potential.

1.4 Mott insulating phase

The system formed by an ultra-cold atomic gas loaded into an optical lattice can be quantum-mechanically well described by the Bose-Hubbard model [43], whose hamiltonian is

$$\mathcal{H} = -J \sum_{\langle i,j \rangle} \hat{a}_i^\dagger \hat{a}_j + \sum_i (\varepsilon_i - \mu) \hat{n}_i + \frac{U}{2} \hat{n}_i (\hat{n}_i - 1) \quad (1.25)$$

In Eq. 1.25, \hat{a}_i^\dagger and \hat{a}_i are the creation and annihilation operators, respectively, at the i -th lattice site, ε_i is the i -th site energy offset, $\hat{n}_i = \hat{a}_i^\dagger \hat{a}_i$ is the number operator and μ is the chemical potential. The parameter J is the tunneling matrix element, while U is the on-site interaction energy

1. Theoretical background

between two atoms. The sum is meant over the nearest neighbours, denoted by $\langle i, j \rangle$.

Regarding the eigenfunctions of this system, the single particle is described by delocalized Bloch states. However, a transformation to a different basis of localized eigenfunctions is requested in order to obtain the second-quantized hamiltonian presented in Eq. 1.25: in general, the Wannier basis is used. It is a set of orthonormal localized states represented by $w_n(x - x_j)$, where j is the lattice site and n identifies the energy band.

The tunneling matrix element J in Eq. 1.25 can be written as follows

$$J = - \int_{-\infty}^{\infty} w^*(x + d_{\text{lat}}) \left[-\frac{\hbar^2}{2m} \frac{\partial}{\partial x} + V(x) \right] w(x) dx \quad (1.26)$$

where d_{lat} is the lattice pitch and V is the lattice potential.

The on-site interaction energy U between two atoms is instead given by

$$U = \frac{4\pi\hbar^2 a}{m} \int |w_n(r)|^4 dr^3 \quad (1.27)$$

where a is the s-wave scattering length. It well described the interactions if their range is short compared to the lattice spacing. This interaction term tends to localize atoms to lattice sites.

The system properties are influenced by the relative magnitudes of J and U , which can be tuned by either adjusting the lattice potential V or by exploiting eventual Feshbach resonance in order to vary the scattering length a [14].

In the system formed by an ultra-cold atomic gas trapped in a lattice potential, the transition from a superfluid (atoms delocalized all over the lattice sites) to a Mott insulating phase can be induced by manipulating the parameters U and J .

If in the hamiltonian Eq. 1.25, interactions dominate such that $U/J \gg 1$, then the variation of the atoms number on a single lattice site becomes energetically unfavourable. In this regime, the ground state of the system consists of localized atomic wave functions which minimize the interaction energy. Such a system is an ideal starting point in order to perform operations on single atoms: actually, if the number of the atoms is chosen carefully, this phase can provide a system in which each lattice site is occupied by exactly one atom.

In order to achieve this experimental conditions, ultra-cold atoms have to be trapped in an optical lattice structure with the sites deep enough to guarantee the Mott insulating phase. Considerations about the sites depth

of a lattice for trapping Ytterbium atoms will be reported in Sec. 2.5.

In this chapter, the characteristics of the Ytterbium atoms and the reasons why Ytterbium is an ideal candidate for the implementation of quantum computing experiments have been explained along with the optical dipole potentials theory and the "traditional" methods used in order to create optical lattices. During this master thesis work, a new method to achieve 2-D optical lattices for trapping Ytterbium atoms is investigated (see Sec. 2.5). This innovative technique is based on the possibility of directly manipulating the laser beam intensity profiles in arbitrary shapes through a Digital Micromirror Device. The DMD and its properties will be presented in the next chapter along with the experimental set-up implemented and its features.

Chapter 2

DMD characterization

The general technical properties of a Digital Micromirror Device will be explained in this chapter.

In the first section the attention is mainly focused on the technical features of the DMD model used, including its behaviour as a diffraction grating, its effects on the incoming laser polarization and its main timing characteristics. In the second section, the experimental optical set-up is explained in its components. In the third, a theoretical treatment of the spatial filtering method is presented. In the fourth, considerations about the set-up diffraction limit are reported, while in the last section theoretical simulations about the projection of a suitable lattice for atomic physics experiments will be presented.

2.1 DMD properties

The DMD model used and characterized in this master thesis work is DLP Discovery 4100, type 0.7" XGA 2xLVDS, produced by Vialux, with a v-7000 board. It is shown in Fig. 2.1.

The DLP Discovery 4100 chip-set includes the following four components

- DLPC410 DMD Digital Controller. It provides high speed data and control interface to the user. It drives the Mirror Clocking Pulses and the timing information to the driver (see below for the details). It also supports random row addressing.
- DLPR410 EEPROM, which stands for Electrically Erasable Programmable Read-Only Memory. DLPR410 contains start-up configuration information.
- DLPA200 DMD Micromirror Driver. It generates the Micromirror Clocking Pulses.

2. DMD characterization

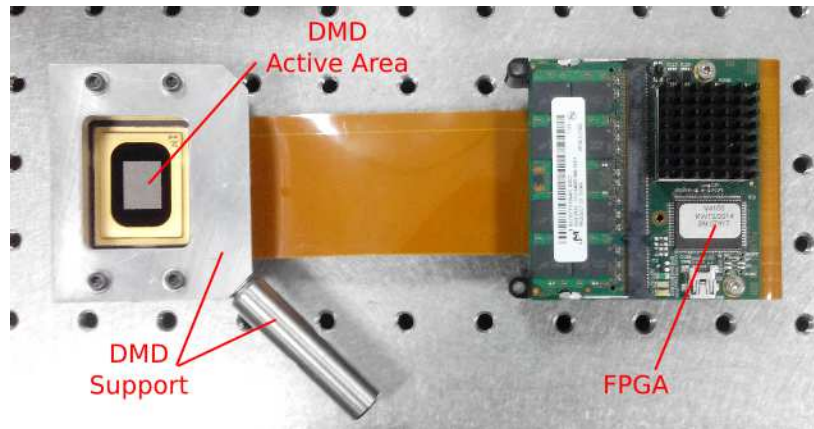


Figure 2.1: The DMD model used with the support designed for it.

- DLP7000 DMD. is the digital micromirror device (DMD) at the heart of the 0.7" XGA¹ chip-set.

The DLP4100 is coupled with a V-7000 board to ease the use of DLP digital micromirror systems. With this board, 22 727 global array updates per second are achieved taking advantage of the 50 Gbit/s bandwidth of the DLP Discovery 4100 chipset. The V-7000 controller board comes with completely configured high-speed FPGA (Field Programmable Gate Array), USB controller firmware and a 64 Gbit RAM in which the data of the images to be projected are stored. The latter will be simply referred to as "DMD Memory Board" from now on.

The DLP7000 Digital Micromirror Device is a digitally controlled MOEMS (micro-opto-electromechanical system) spatial light modulator (SLM). When coupled to an appropriate optical system, the DLP7000 can be used to modulate the amplitude of incoming light. Electrically, it consists of a two-dimensional array of 1-bit CMOS memory cells, organized in a grid of 1024 memory cell columns by 768 memory cell rows. Optically, the DLP7000 consists of highly reflective micrometer-sized mirrors (micromirrors), organized in a two-dimensional array of 1024 columns by 768 rows [40]. Each micromirror is approximately 13.68 μm in size and it can digitally switch between two discrete angular positions: -12° and $+12^\circ$, with respect to the surface normal.

Each individual micromirror is positioned over a corresponding CMOS memory cell and its angular position is determined by the binary state, 0 or 1, of the corresponding CMOS memory cell contents. The angular position of

¹In the field of visual displays, the 1024 by 768 pixels resolution is referred to as "XGA".

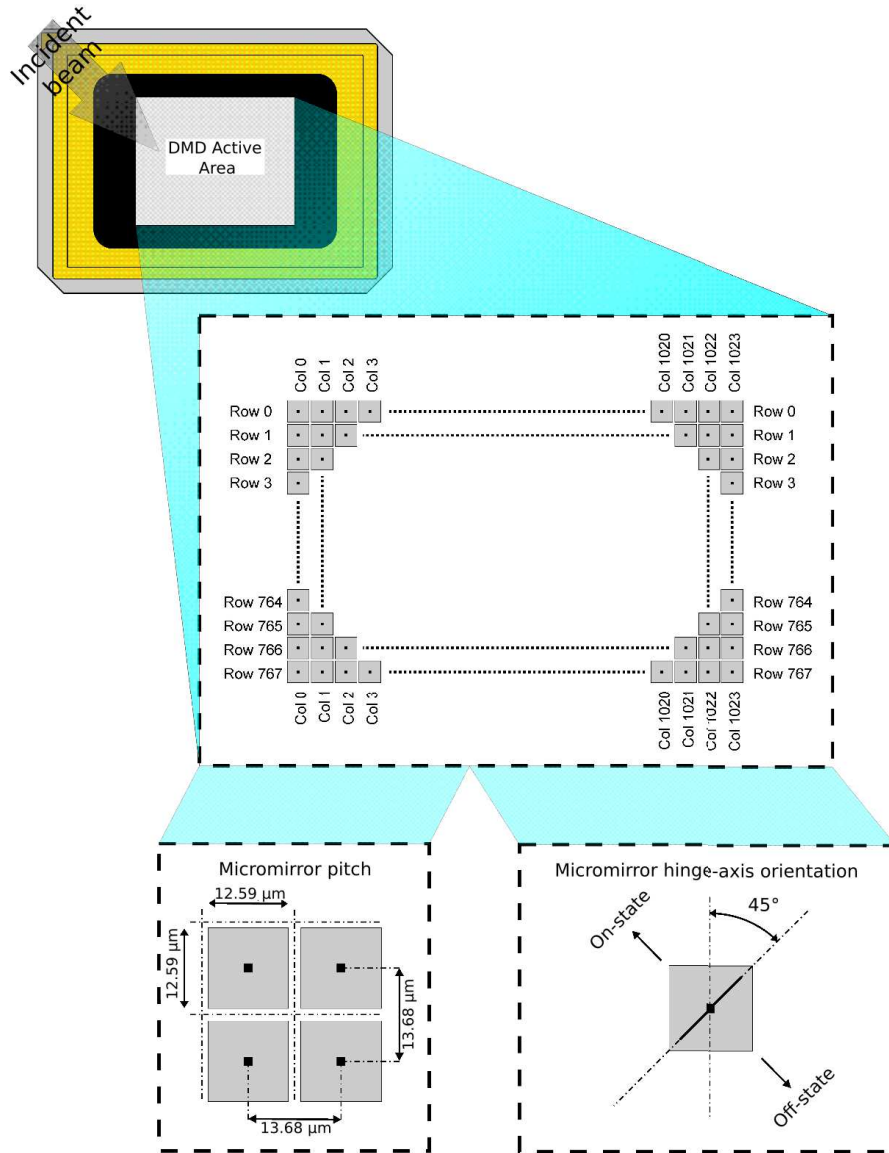


Figure 2.2: DMD Active Area scheme.

the every micromirror changes synchronously with a "Micromirror Clocking Pulse", rather than with the CMOS memory cell data update. Therefore, writing a logic state into a memory cell will switch the corresponding micromirror in the chosen position only if this operation is followed by a Micromirror Clocking Pulse.

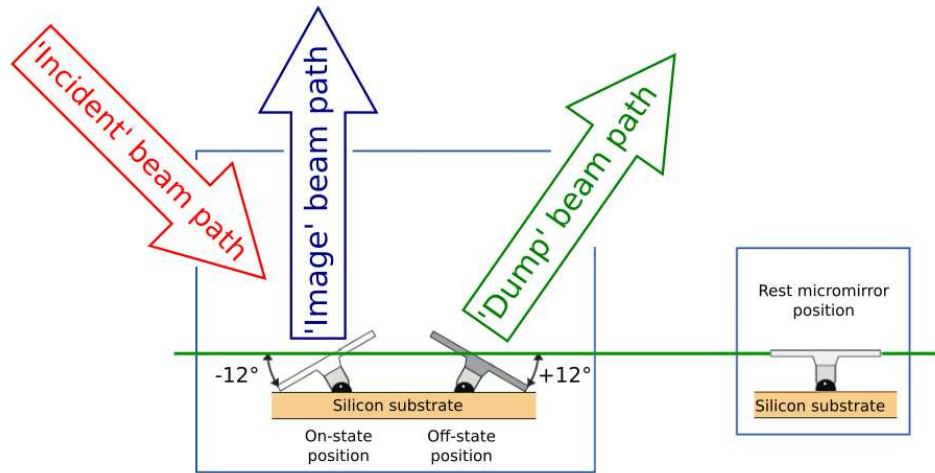


Figure 2.3: Scheme of the incident and reflected beams.

In Fig. 2.2 a schematic representation of the DMD Active Area² structure is reported. It is worth noticing that the tilt direction is perpendicular to the hinge-axis which is positioned diagonally relative to the overall array, thus the micromirrors rotation axis forms an angle of 45° with the DMD vertical axis: this feature has to be taken into account during the set-up planning (see Sec. 2.2).

When the projection is switched off, the micromirrors are set in their "rest" position, that is parallel to the device surface. Instead, when the projection is switched on, they can be individually tilted *only* by an angle $\pm 12^\circ$ with respect to the surface normal, assuming their so-called "on" or "off" state³, as shown in Fig. 2.3. When a micromirror is in its on-state, it reflects a little portion of the incoming light in order to form the image displayed; whereas, if it is in the off-state, it reflects the light portion in the other direction, typically into a beam-dumper. In principle, there is no difference between the two reflected beams (called "image" and "dump" beams), so they are interchangeable as well as the role of the two possible states assumed by the micromirrors. The ones set in the on-state can create both the image or the dump beam and the same holds for the ones in the off-state.

As said, the micromirrors pitch is $13.68 \mu\text{m}$, so the overall dimensions of the DMD screen are (14.0×10.5) mm. However, the micromirrors area is not

²The whole DMD Active Area is protected by a glass windows made in *Corning 7056*, which has a broadband anti-reflection coating for the visible region.

³Further technical information about DMD electronic and mechanical working can be found in Lee, 2013 [49].

$(13.68 \mu\text{m})^2 = 187.14 \mu\text{m}^2$, but is actually smaller by a factor – called "Fill Factor" – equal to 92% for the DMD model used, so the effective micromirror area is $172.17 \mu\text{m}^2$. The remaining 8% is occupied by a substrate.

The pattern displayed on the DMD screen can be thought as a gray-scale raster image⁴. Each pixel thereof is related to a DMD micromirror with a one-to-one correspondence: for example, the first top-left pixel of the raster corresponds to the (0,0) micromirror of the device. As the available states of the micromirrors during a projection are two (on-state and off-state), the possible values assumed by a pixel can be only two. Therefore these pixels form a one-bit raster image, i. e. a "bitmap", which are images formed by just two colors (black and white). The value of each pixel (0 or 1) of the bitmap determines the position of the related micromirror ($\pm 12^\circ$). Bitmaps can be directly loaded into the DMD Memory Board with the aid of the supplied software and projected at a later stage (the DMD control software developed during this thesis work is presented in Chap. 4).

Technically, a gray-scale image (having a pixel-depth higher than one) could be loaded into the DMD Board Memory too. In order to emulate it, the device divides such image into a collection of one-bit sub-images which are displayed with suitable different "reproduction time" calculated by the DMD itself. Thanks to this expedient, toggling the mirrors on and off quickly, the device is able to simulate an image which is perceived in grey-scale to an human eye. However, it is not effectively static as it could appear. Moreover this time dependence is not suitable for atoms trapping due to their fast response time. In order to avoid this inconvenient and obtain a really static gray-scale image (pixel-depth higher than one), digitization methods can be employed to reduce it into a bitmap having only two colors (black and white). Every digitization method is based on the manipulation of the data stored in the matrix standing for the raster image. For example, let the image matrix data be normalized in the range (0,1): the simpler and most immediate digitization algorithm consists in rounding each pixel value to 0 or 1. The former represents a black pixel, while the latter a white one. So, if a certain matrix element were 0.6 (0.35), then it would be changed in 1 (0) and the corresponding image pixel would appear white (black). The image produced by this method is called "Rounded version" of the initial one.

Further details about these processes and dithering algorithms, which are more sophisticated digitization methods than the one described above, are presented in Chap. 3.

⁴A raster graphics image is a matrix data structure representing a generally rectangular grid of pixels, viewable via a display medium as a monitor. A raster is technically characterized by width and height of the image, expressed in pixels, and by the number of bits per pixel, called pixel-depth.

2. DMD characterization

Due to the composite nature of the device, the images projection with the DMD is not particularly convenient in terms of optical efficiency. This can be estimated for broadband visible light (400 nm - 700 nm) with the aid of the following factors (also resumed in Tab. 2.1)

- Fill Factor. It has already been discussed previously.
- Diffraction Efficiency. The DMD works as a grating due to its pixelated nature, so a diffraction efficiency can be defined: it is the power diffracted into the zero-th order with respect to the overall incoming beam power. As the zero-th order is the used one, this factor has to be considered.
- Surface Reflectivity. It is evaluated for a single micromirror and is defined as the ratio of the incoming beam power to the reflected beam power, which is smaller because of absorption phenomena.
- Windows Transmission. It is meant as the power percentage of a light beam which passes through the glass protection window (a single pass through two faces is considered).

| | |
|--|---------------------|
| DMD Micromirror Array | 1024 × 768 |
| Micromirror Pitch | 13.68 μm |
| Micromirror Side | 12.59 μm |
| Active Mirror Array Area | 14.0 mm × 10.5 mm |
| Flipping Angle | ± 12° |
| RAM Capacity on Board | 64 Gbit |
| Binary Patterns on Board | 87 380 |
| Windows Option | VIS, UV |
| Damage Threshold | 25 $\frac{W}{cm^2}$ |
| Array Switching Rate 1 bit B/W | 22 727 Hz |
| Array Switching Rate 6 bit Gray | 1091 Hz |
| Array Switching Rate 8 bit Gray | 290 Hz |
| Micromirror Array Fill Factor | 92% |
| Micromirror Array Diffraction Efficiency | 86% |
| Micromirros Surface Reflectivity | 88% |
| Window Transmission (VIS region) | 97% |

Table 2.1: Technical specifications of the DMD model used, DLP7000.

Hence, the DMD theoretical optical efficiency turns out to be about 66%. An experimental evaluation of the optical efficiency has been carried out. After having displayed on the DMD screen a completely white image (all the micromirrors set in the same state), the powers of the incident and reflected laser beams ($\lambda_L = 578$ nm) are measured by a power meter. The image beam power is recorded far enough from the DMD in order to separate the several diffraction orders and take into account only the zero-th one. The ratio of the two measured powers gives the experimental optical efficiency. It is estimated to be about 61%.

Diffraction Properties Basically a Digital Micromirror Device is a matrix of tiny mirrors arranged in a checkerboard, with gaps between the mirrors sides. Therefore, due to the discrete nature of the device, it behaves like a diffraction grating [42], and, during a projection, it works like a blazed diffraction grating, which is characterized by a further degree of freedom with respect to the usual one: the tilting angle of the reflecting slits.

In general, the angular position of the diffraction orders depends only on the wavelength λ and the spacing a of the slits, as shown in Eq. 2.1.

$$m\lambda = a (\sin(\alpha) + \sin(\beta)) \quad (2.1)$$

where m is the diffraction order, α is the angle of incidence of the incoming beam on the grating surface and β is the angle of the m -th diffraction order⁵. Fig. 2.4 reports in the left panel a variable scheme used to study the diffraction caused by a 2-D object: ignoring the y -axis, it shows the variables used for treating the 1-D object diffraction.

The intensity distribution of a diffraction grating (not blazed) is formed by a central peak of the zero-th order ($\alpha = \beta$) and lateral smaller peaks of the other ones. Mathematically, the Fraunhofer diffraction (far-field approximation) describes this intensity distribution (Eq. 2.2) through the product of a sinc^2 function – one per dimension, which represents the diffraction of a single slit – and a factor which stands for the interference between the beams diffracted by the slits arrays.

$$I(p, q) = I_0 \left(\text{sinc}^2(kpa) \frac{\sin^2\left(N \frac{kpd}{2}\right)}{\sin^2\left(\frac{kqd}{2}\right)} \right) \left(\text{sinc}^2(kqa) \frac{\sin^2\left(M \frac{kpd}{2}\right)}{\sin^2\left(\frac{kqd}{2}\right)} \right) \quad (2.2)$$

where $k = 2\pi/\lambda$ is the wave vector, N (M) is the number of enlightened slits along x -axis (y -axis), a is the slit dimension, d is the grating spacing and

⁵The angles are measured from the grating surface normal. For a reflective grating, an angle is considered positive if measured in counter-clockwise direction, otherwise it is negative.

2. DMD characterization

I_0 is the intensity reflected in the center of the diffraction pattern. Instead, p and q are defined as follows

$$\begin{cases} p = \sin(\alpha) - \sin(\beta) = \frac{m\lambda}{d} \\ q = \sin(\gamma) - \sin(\delta) = \frac{m'\lambda}{d} \end{cases} \quad (2.3)$$

where m and m' are the diffraction orders along the x and y directions, α (γ) is the angle between the x-axis (y-axis) and the incident beam, while β (δ) is instead the angle formed by the x-axis (y-axis) and the observation direction, as can be seen in the scheme to the left in Fig. 2.4. The last passage can be easily deduced by maximizing the multi-slits interference in Eq. 2.1.

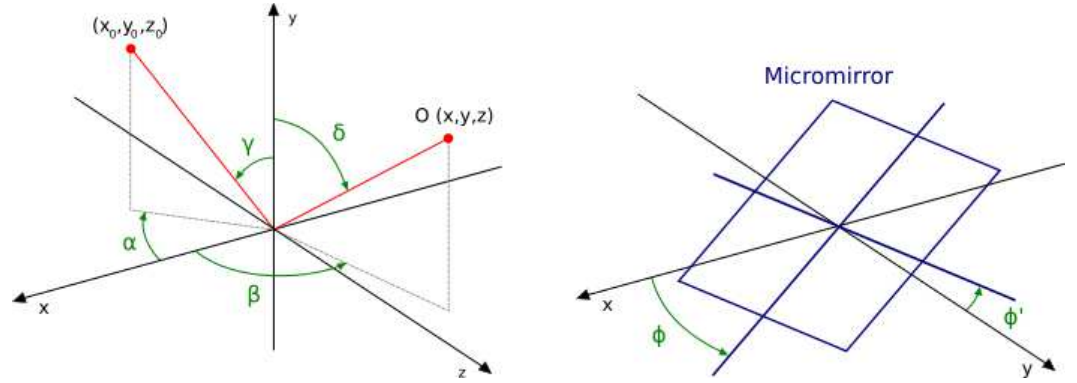


Figure 2.4: Diffraction variables schemes. The 2-D grating lies on the $x - y$ plane.

However the intensity distribution for a blazed grating is different because the groove faces have a normal that is not collinear with the grating one: the result is that the center of the sinc^2 envelope is decoupled from the zero-th order. In this case, Eqs. 2.3 become

$$\begin{cases} p = \sin(\alpha + \phi) - \sin(\beta - \phi) \\ q = \sin(\gamma + \phi') - \sin(\delta - \phi') \end{cases} \quad (2.4)$$

where ϕ and ϕ' are the blazing angles along the grating dimensions (see the image to the right in Fig. 2.4).

The location of the zero-th interference order only depends on the incident angles α and γ , whereas all the other orders also depend on the grating pitch d and on the wavelength λ . Furthermore, the location of the center of the diffraction envelope depends only on the incident angles α and γ and on the tilting angles ϕ and ϕ' of the groove faces, while its minima are dependent on the grooves width a and the wavelength λ . Hence, by changing the incident angle, it is possible to align the center of the envelope with a diffraction order.

In Tab. 2.2 the relative powers measured for the zero-th and first orders are reported. For these measurements, the DMD has been enlightened by a laser beam forming an angle of 12° with respect to the DMD surface normal. Its waist is about 5.8 mm. The overall beam power has been measured before the device with a power-meter; instead, the powers of the first diffraction orders have been measured by a power-meter far enough from the DMD in order to properly separate them. The direct reflection (zero-th order) is the most powerful and actually is the order used for the experiments, instead of the other ones which have been blocked.

| | |
|---------------|---------|
| Zero-th Order | 36.74 % |
| First Orders | 7.16 % |
| | 5.88 % |
| | 1.67 % |
| | 1.12 % |

Table 2.2: Relative power of different orders. The beam forms an angle of 12° with respect to the DMD surface normal. The image projected by the DMD is completely white (all mirrors switched on).

Effects on polarization Technically there are not apparent reasons why a DMD should change the polarization of a well-defined polarized incoming laser beam, but a variation of polarization can be noticed, probably due to the coated protective glass plate placed upon the DMD Active Area.

During this work, it has been verified that an input beam with a horizontal or vertical linear polarization is reflected into a beam having a quasi-circular polarization (49% V and 51% H). This statement has been verified making use of a half-wave plate, a quarter-wave plate, a polarizing beam splitter and a power-meter; furthermore different patterns have been tested. The output beam does not have a linear polarization, i.e. a linear combination of H and V ones, but effectively an elliptic polarization, practically circular. Moreover, if the polarization of the input beam were circular, the output one would be linear. A quarter-wave plate has been placed just before the DMD in order to obtain an output vertical linear polarization.

Due to the cylindrical symmetry of the optical set-up, the light polarization does not have a particular relevance for the results of the experiments carried out in this work. However, knowing the effects of the DMD on the polarization is of high relevance for atomic physics applications.

Timing Properties The images projection with a DMD is divided in different phases: here some details about their timing characteristics will be given. In the DMD Memory Board, several images can be organized in a sorted sequence. Some timing properties, which cannot be changed during

2. DMD characterization

the projection, can be associated to each sequence. They are explained below and represented in Fig. 2.5.

- *Illuminate Time* (IT), which is the duration of the display of a single picture in a given sequence.
- *Picture Time* (PT), i.e. the time occurring between two consecutive frames.
- the so-called *Dark Phase* (DP), namely the time-interval existing between the end of an *Illuminate Time* and the consecutive one's start.

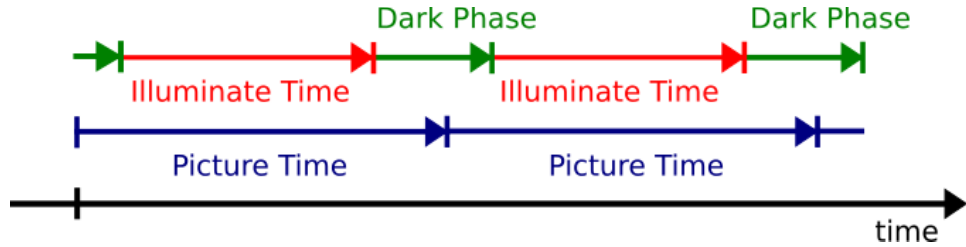


Figure 2.5: DMD time properties scheme. The Dark Phase minimum value is $44 \mu m$, while the *Illuminate Time* assumes values between tens of μs and 10 s.

Basically, the single frame projection occupies a part of the *Picture Time*, the *Illuminate Time*. Afterwards it takes some time – *Dark Phase* – to initialize and prepare to projection the next frame. During this lapse, the DMD micromirrors can oscillate among the on-state, the rest position and the off-state due to the mechanical stimulation received.

While the user can choose the *Illuminate Time* and *Picture Time*, the *Dark Phase* cannot be modified manually but it is automatically set by the device. The more convenient choice is to select only the *Illuminate Time* and let the *Picture Time* assume its default value: in this case, the DMD will set autonomously the *Picture Time* in order to minimize the *Dark Phase*. Nevertheless there is a minimum for the *Dark Phase* (called Δt_1 in the technical data-sheets), depending on the device model. For the XGA types it is $44 \mu s$: actually, it is just the time needed to change the position of each mirror. This gives a maximum frame refresh rate of 22.7 kHz.

In mathematical terms, the DMD timing properties can be expressed as follows

$$\begin{aligned} PT - IT &= DP \\ PT - IT &\geq \Delta t_1 \end{aligned} \tag{2.5}$$

The continuous projection⁶ is forbidden by the existence of a maximum value for the Illuminate Time, that is 10 s. This means that if a sequence contains a single frame, its projection will not be continue: after an Illuminate Time of 10 s, the DMD will anyway moves its micromirrors to display the same image, as if the sequence were formed by lots of identical images.

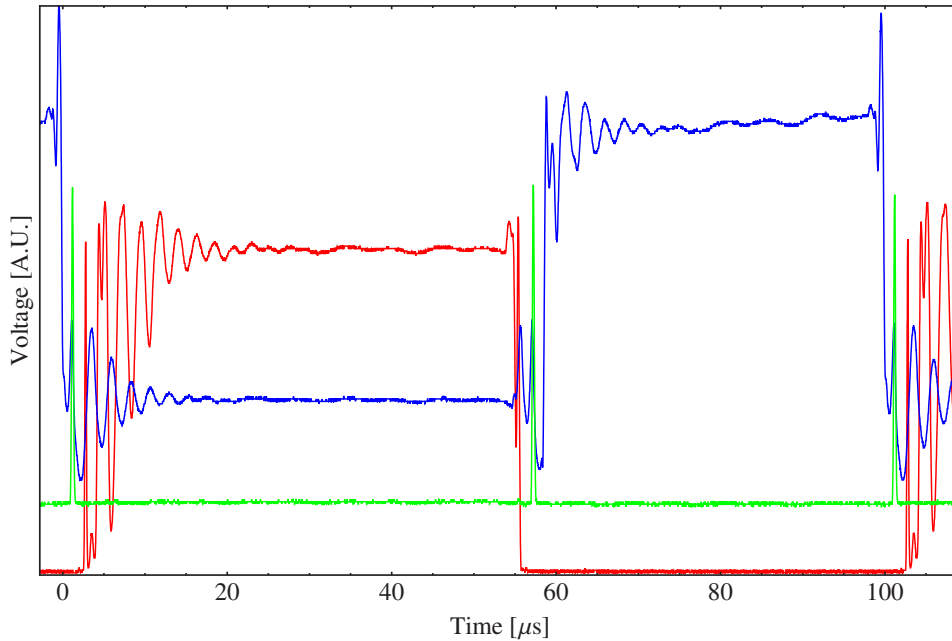


Figure 2.6: In red, the signal returned by the photo-diode placed along the image beam path; in blue, the complementary signal referred to the dump beam; in green, the signal given by the light reflected in the normal direction to the DMD (rest position).

In order to experimentally verify the DMD timing properties, the power of the image and dump beams are recorded by two photodiodes as a function of the time. A third photodiode is placed exactly in front of the DMD surface in order to detect the light reflected by the micromirrors in the rest position. A Flat-top pattern of 400 pixels per side has been displayed on the DMD (for further details about Flat-tops see Sec. 3.2 and Sec. 5.2). In Fig. 2.6 the three traces are reported.

The Picture Time is set to 100 μs , while the Illuminate Time is forced to be 60 μs , although its effective value is 56 μs in order to respect the Dark Phase minimum value, 44 μs . These values can be checked on the graph: the green

⁶There is a projection option called "Bin Uninterrupted" which allows to eliminate the excess of Dark Phase but not the minimum. With this option set, the Illuminate Time is ignored because it is implicitly determinate by the Picture Time and the minimum value of the Dark Phase.

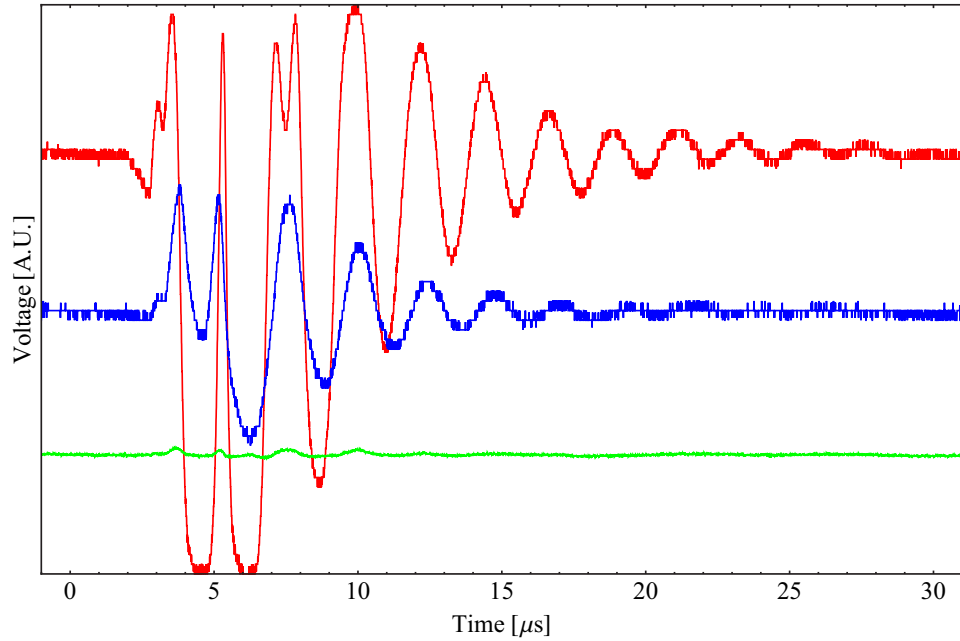


Figure 2.7: Micromirrors flickering. In red, the signal of the image beam; in blue, the signal of the dump beam; in green, the signal of the rest position. In this case, the green trace is supposed to be flat because the micromirrors oscillate around on-state or off-state positions without passing through the rest one: actually there are no peaks, as in Fig. 2.6.

peaks delimit the Illuminate Time before and the Dark Phase after. Moreover, the Illuminate Time has been chosen of the order of hundreds of μs in order to highlight another DMD projection characteristic: the micromirrors flickering. This effect can be better appreciated in Fig. 2.7. After the micromirrors reach their target position, they suffer several oscillations with frequency of about 450 kHz. The oscillation phase lasts about 20 μs . Afterwards, they enter in a rest state till next refresh.

2.2 Optical set-up

The optical set-up scheme used to study the DMD properties has been designed on the basis of the scheme proposed in [7] and it is shown in Fig. 2.8.

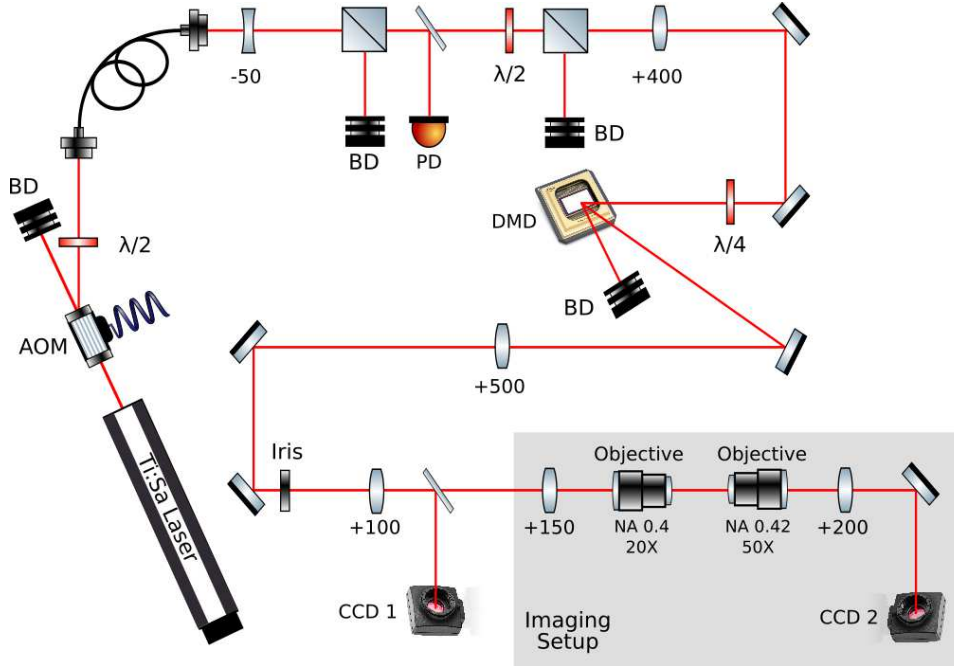


Figure 2.8: Optical set-up scheme. The focal lengths are expressed in mm. "DB" stands for beam dumper.

The laser source used – which is employed for the generation of the lattice for Yb atoms – is a Coherent MBR110 Ti:Sa at 759 nm, pumped by a Verdi V18. The laser light is sent via a polarization-maintaining fiber to the DMD set-up, so the working mode is the fundamental gaussian mode (TEM_{00}). In order to avoid – or, at least, minimize – polarization oscillations due to the fiber, the linear polarization of the incoming beam ought to be coincident with the one of the fiber axes. This matching is obtained by a half-wave plate. After the fiber stage there is a telescope, made with a divergent lens ($f_1 = -50$ mm) and a convergent one ($f_2 = +400$ mm) at distance of 35 cm, in order to enlarge the beam waist and obtaining a more uniform illumination of the DMD active surface.

A first polarizing beam splitter (PBS) is used to transform any possible polarization fluctuation after the fiber into power fluctuations. The power is stabilized by taking a small portion of the laser light with a pellicle beam splitter (Thorlabs BP108) and by sending it onto a photodiode (Thorlabs DET36A). The photodiode (PD) output is fed as error signal to a "PI" Servo

2. DMD characterization

which acts on an acousto-optic modulator (AOM) placed before the fiber (See Fig.2.8). The power stabilization is a fundamental requirement for the feedback process to work properly. See Sec. 4.2 for the details about the feedback.

The DMD axes form a 45° angle with respect to the vertical direction and lay on a plane that is orthogonal to the table top. In this configuration, both incident and reflected beams are horizontal. In this set-up, an angle of -12° is created by the incoming laser beam with respect to the DMD surface normal. In this way, the dump beam is reflected at an angle of 24° , as can be seen in the scheme in Fig. 2.8; but, mostly of all, a direct imaging can be performed (avoiding image distortions) because the outgoing image beam is perpendicular to the DMD surface.

A half-wave plate is set just before the DMD in order to shift the beam polarization into a linear vertical one.

After the Digital Micromirror Device a second telescope, formed by a $f_3 = +500$ mm lens followed by a $f_4 = +100$ mm one at distance of 600 mm, is placed. It has a total demagnification of 5 to reduce the beam dimensions in order to allow the feedback CCD (see below) to completely detect it. The telescope is coupled with an iris placed in the focus position of the first lens and is also exploited in order to perform a spatial filtering of the beam and to clear the image from high frequency components in the Fourier domain (see Sec. 2.3).

With a beam sampler (Thorlabs BSF20-B), a small portion of light is taken and delivered to a CCD camera (Thorlabs DCC1545M-GL, named in this set-up CCD 1) in order to perform the feedback on the projected images (see Sec. 4.2). As also underlined in Liang et al., 2009 [52], the protective glass plate of CCD used for this aim should be removed in order to minimize the arising of fringes or diffraction patterns caused by parallel surfaces, etalon effects and dirty spots.

The imaging set-up is formed by two facing microscopes, each one composed by an infinity-conjugated objective and its respective tube lens. The objective which is meant to be implemented in order to project the images (first one) has a numerical aperture of 0.7 and a magnification of 80X. Anyway, as it was not available during the set-up implementation, a different one has been used to test and characterize the DMD and its projected images quality. This objective (CFI "Plan Fluor" 20x/0.50 by Nikon), has a numerical aperture of 0.50 and a magnification of 20X, if coupled with its tube lens. The second one (50X Plan Apo NUV by Mitutoyo) is used for performing the imaging. It has a numerical aperture of 0.42 and a magnification of 50X with its tube lens (200 mm). Therefore, totally, the second telescope and the first microscope should achieve a demagnification of 100X. The patterns after the image set-up are recorded by a second CCD (IDS UI-1220LE, called CCD 2 in this set-up).

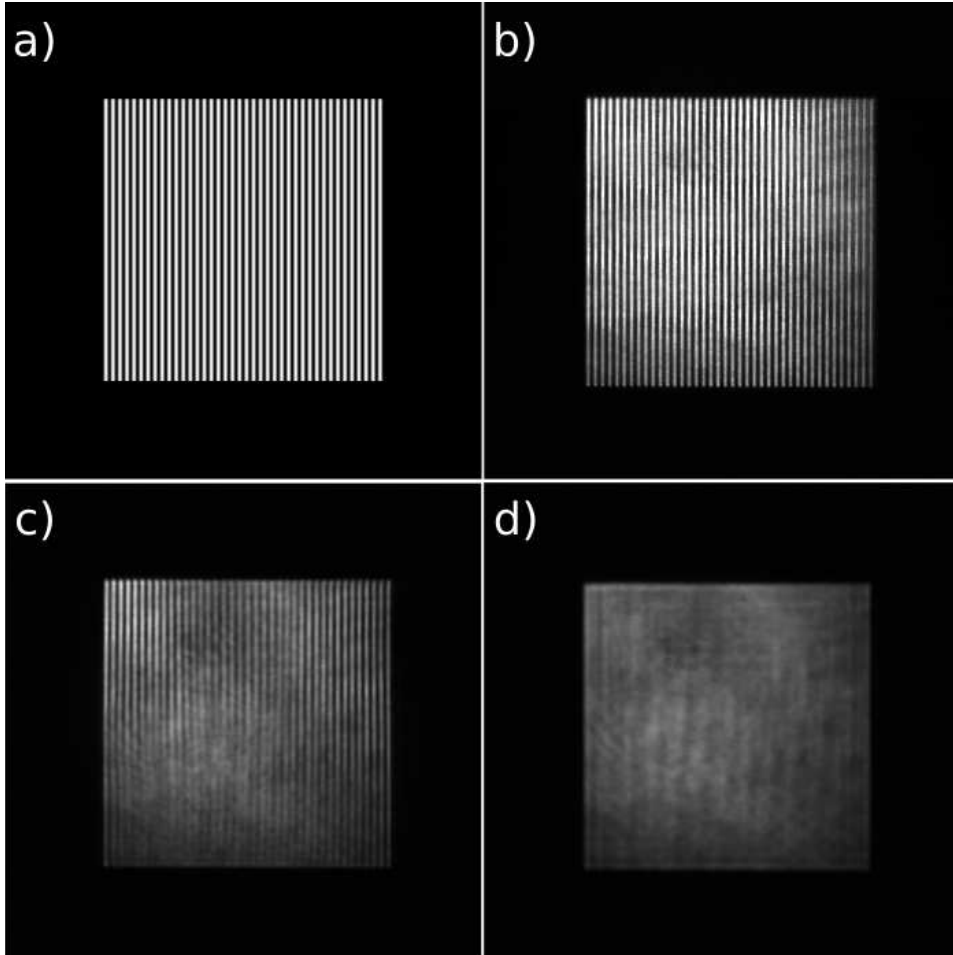


Figure 2.9: a) Pattern projected by the DMD and its several images captured by the CCD 1 with different iris diameter: iris wide open b), iris diameter equal to 0.4 mm c) and to 0.3 mm d). Regarding the iris and the spatial filtering, see Sec. 2.3.

The frame a) in Fig. 2.9 shows the density-plot of a 1-D sinusoidal function plotted in a (400×400) area (see Sec. 3). The image of this pattern projected by the DMD captured by the CCD 1 (before the imaging set-up) is reported by the frame b) in Fig. 2.9, while the image recorded by the CCD 2 is shown in the frame a) in Fig. 2.10.

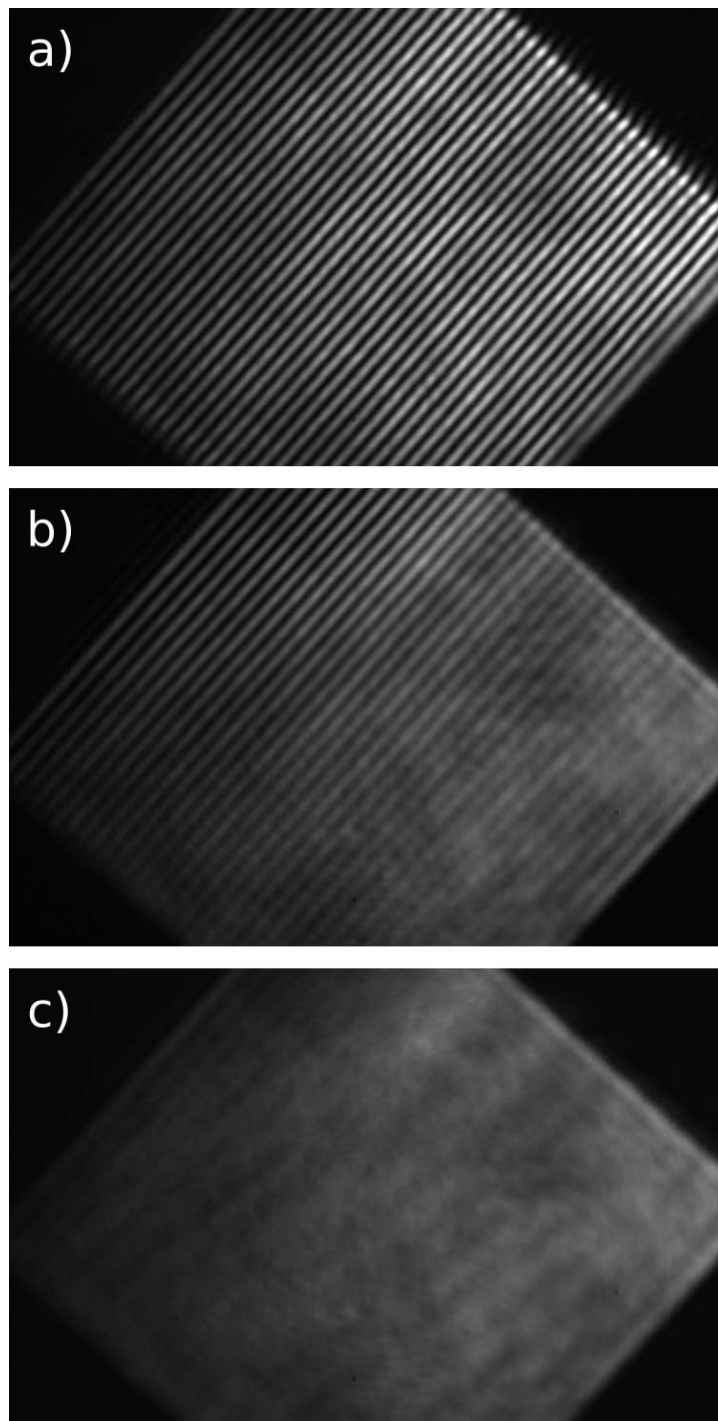


Figure 2.10: Images of the pattern shown in the frame a) of Fig. 2.9 captured by the CCD 2 with different iris diameter: iris wide open a), iris diameter equal to 0.4 mm b) and to 0.3 mm b). Regarding the iris and the spatial filtering, see Sec. 2.3.

2.3 Spatial filtering

An image can be digitally encoded by the raster graphics. In this representation, the image is discretized in a grid structure, whose elements stand for pixels or points of color. Therefore, numerically, a picture is equivalent to a data matrix on which several operations could be applied. One of the most important global operation⁷ that could be performed on a graphical object is the Discrete Fourier Transform (DFT) [20]. In the case of an image, the DFT maps all the pixels of the coordinate space to a new representation (with the same size) where the brightness of each new element describes the amount of a particular spatial frequency component occurring in the original picture. This spatial frequency corresponds to a wave-vector k .

In mathematical terms, the Discrete Fourier Transform of a 2-D function $f(x, y)$ which has been sampled at discrete intervals Δx can be expressed as

$$\mathcal{F}(p, q) = \sum_{n=-\infty}^{\infty} \sum_{m=-\infty}^{\infty} f(x, y) e^{-2\pi i(pn\Delta x + qm\Delta x)} \quad (2.6)$$

If the number of the samples are finite, they can be arranged in a finite matrix M . Therefore a DFT can be performed on an matrix standing for a raster image as follows

$$\mathcal{F}(p, q) = \sum_{n=0}^{N_W-1} \sum_{m=0}^{N_H-1} M(n, m) e^{-2\pi i(pn\Delta x + qm\Delta x)} \quad (2.7)$$

where Δx is the squared pixel size, N_W and N_H the pixel numbers along the two dimensions and $M(n, m)$ the value contained in the (n, m) pixel. It can be noticed that $\mathcal{F}(0, 0)$ represents the DC-component of the image which corresponds to its average brightness.

In general, this operation applied on a vector of real numbers returns a vector with the same dimension of complex numbers which can be graphically represented through the magnitude and phase diagrams.

Along one of the two image axes (vertical or horizontal), the lowest frequency of the image that can be obtained by the DFT depends on the real image dimension and it is $(N\Delta x)^{-1}$, while the higher spatial frequency can be deduced via the Nyquist-Shannon theorem. It states that an sinusoidal signal has to be sampled at a rate greater than two samples per period in order to avoid information loss or aliasing. This means that the maximum frequency is $(2\Delta x)^{-1}$. In most graphical representations, the image in the Fourier domain is shifted in such a way that the DC-value $\mathcal{F}(0, 0)$ is displayed in the center of the image. The further away from the center an image point is, the higher is its corresponding spatial frequency till the maximum frequency available

⁷If each pixel of the output image is the result of a transformation which involves all the pixels of the initial image, then this transformation is called "global".

(positive or negative), bounded to the pixel dimension.

Fig. 2.11 reports an example of image and the magnitude diagram of its Fourier Transform. The latter shows that the image contains components of all frequencies, although their magnitude gets smaller for higher frequencies.

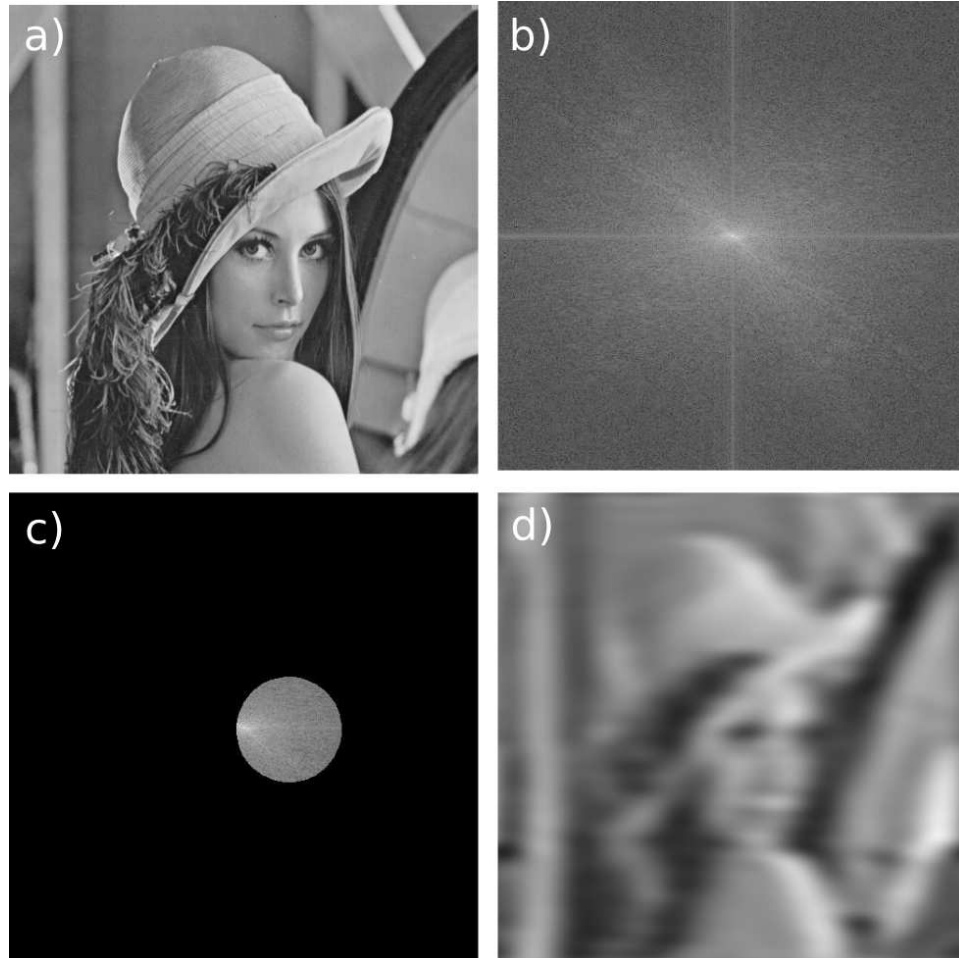


Figure 2.11: a) A classical example in field of graphical elaboration, Lena's portrait. b) Its Fourier Transformed version. c) The application of a spatial filter in the Fourier Space. d) The Anti-transformed Lena's portrait.

Generally, any local modification of $\mathcal{F}(p, q)$ is a filtering operation as it involves the modification of the contribution of certain spatial frequency components. The image c) in Fig. 2.11 shows the application of a circular filter in the Fourier domain: all the spatial frequencies which fall out of the filter are eliminated. The image d) in Fig. 2.11 reports the result of the Fourier Anti-transform applied on the modified Fourier space: without the contribution of the suppressed frequency components, Lena's portrait now

appears blurred.

In Fig. 2.12 three kinds of passband filters performed on the Fourier Transformed Lena's portrait are reported, along with the anti-transformed real images produced by their application.

The implementation of a low-pass filter in the optical set-up would be useful to block and avoid the transmission of the image high-frequency components. In this way, the image projected could be cleaned from the high-frequency noise introduced, for example, by the spurious DMD effects or interference fringes.

Physically, such a filter can be performed by exploiting the Fourier properties of the lenses. Since a lens is a finite circular object, a laser beam passing through it undergoes the Fresnel-Kirchhoff diffraction (see next Sec. 2.4). If an object is placed in the lens focus of the object space, then its Fourier Transform will be formed in the lens focus of the image space. This can be deduced from the mathematical formulation of the diffraction, for example treated in Born and Wolf, 1970 [8]. Therefore a low-pass filter can be created by

- A first lens, which performs the Fourier Transform of the incoming beam.
- An iris⁸ placed in the first lens focus in order to block the most external part of the beam, i. e. the higher frequencies/wave-vectors. Adjusting the iris diameter, a different cut-off for the higher spatial frequency can be achieved.
- A second lens, which performs the Fourier Anti-transform of the beam and returns in the real space the filtered image imprinted on the laser beam through its intensity modulation.

As this kind of filter eliminates the higher spatial frequencies of an image, it will be referred to as "spatial filter" from now on.

The frame c) in Fig. 2.9 and the frame b) in Fig. 2.10 report the image of the density-plot (frame a) of Fig. 2.9) of a 1-D sinusoidal function plotted in a (400×400) area (see Sec. 3) projected by the DMD, manipulated by a spatial having iris diameter equal to 4 mm, captured by the CCD 1 and CCD 2, respectively. Comparing the two images with the frames b) of Fig. 2.9 and a) in Fig. 2.10, the effect of the spatial filter can easily be noticed. Reducing the iris diameter, the filter cuts an higher number of spatial frequencies and

⁸The beam travelling through the first lens is not a gaussian one due to the previous intensity spatial modulation of the DMD, so it is not necessary using an obstacle with a particularly narrow aperture to perform the filtering. That is the reason why an iris is preferred over a pinhole.

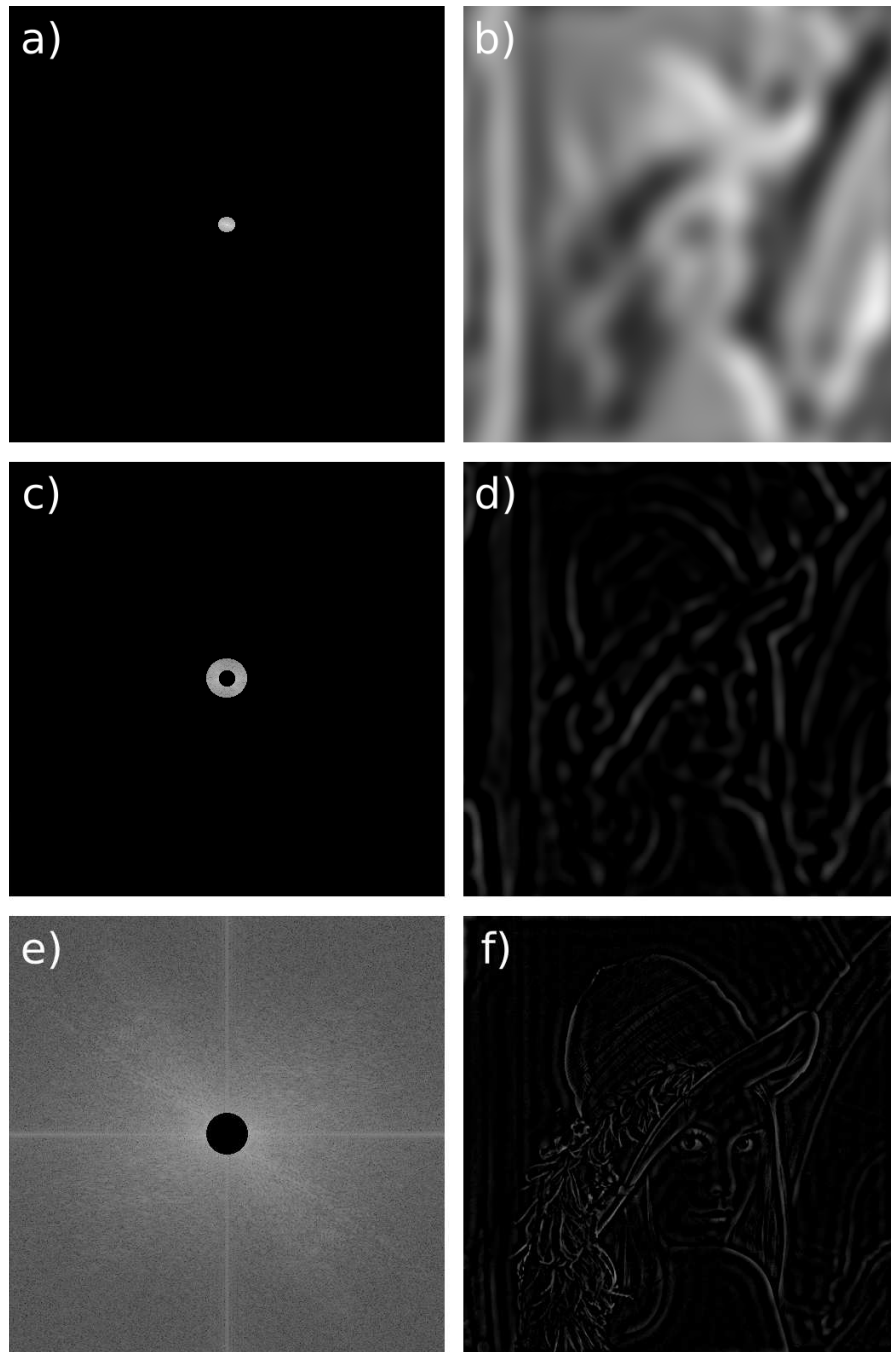


Figure 2.12: Examples of bandpass filters. a) A low-pass filter and b) its effect in the real space. c) A bandpass filter and d) its effect in the real space. e) A high-pass filter and f) its effect in the real space.

the resulting patterns appeared averaged in intensity (frames d) of Fig. 2.9

and c) of Fig. 2.10).

2.4 Diffraction limit of the optical set-up

A light beam incident on a finite aperture exhibits its wave nature through an intensity distribution characterized by maxima and minima, instead of the expected aperture shadow, due to the diffraction. This limits the imaging system optical resolution, which is the ability to resolve details of the observed object. More precisely, the resolution is defined as the minimum distance Δx_{\min} at which two different points of the object can be distinguished as single ones. In order to express this definition in quantitative terms (Eq. 2.8), several criteria can be followed, but the most common is known as Rayleigh criterion, which states that two points are resolved if the Airy disk⁹ maximum of a point overlaps the first dark ring in the Airy pattern of the other one.

$$\Delta x_{\min} = \frac{1.220 \lambda}{2 \text{N.A.}} = 1.220 \lambda \frac{f}{D} \quad (2.8)$$

where the Numerical Aperture $\text{N.A.} = n \sin(\theta)$ has been expressed in terms of the pupil diameter D and focal length f in the second passage; θ is instead the half-angle of the maximum cone of light that can enter or exit the optical object. The second expression in Eq. 2.8 can be more useful for evaluating the Δx_{\min} of a lens, for example. The diffraction limits of the two lenses f_3 and f_4 of telescope which performs the spatial filtering are $9.1 \mu\text{m}$ and $1.8 \mu\text{m}$, respectively.

The iris contributes to the diffraction limit too: actually, as said, it operates a cut of the higher spatial frequencies depending on its diameter, in this way the smaller details appear blurred or are directly eliminated. If the iris diameter were the maximum possible, 12 mm, then the cut-off spatial frequency would be

$$\nu_{co} = \frac{D}{2 \lambda f} \approx 16 \text{ mm}^{-1} \quad (2.9)$$

where D is the iris diameter and f is the distance from the first lens. So the maximum distance resolvable if the beam is skimmed by the iris is about $63 \mu\text{m}$ and it increases with the decreasing diameter.

Therefore, after the telescope and the iris stage, the minimum resolvable feature in the projected image is $13 \mu\text{m}$ due to the demagnification of 5. In the microscope system, the objective is more limiting than its tube lens in terms of resolution: actually it can resolve a minimum distance of 926 nm in the sample plane which corresponds to about $18.5 \mu\text{m}$ in its back-focal plane.

⁹The diffraction pattern resulting from a uniformly-illuminated circular aperture has a bright central region, known as *Airy disk*, which is surrounded by a series of concentric bright rings, called *Airy pattern*.

Hence, the diffraction limit of the whole optical set-up is determined by the objective¹⁰: it means that two points distant less than 7 pixels on the DMD can not be distinguished by this optical set-up.

2.5 Optical trapping with a DMD

The main and ultimate aim of this master thesis work is to find out if acceptable lattice structures can be created modulating a laser beam with a Digital Micromirror Device rather than using pairs of counter-propagating laser beams as in the standard way (see Sec. 1.3). Surely a generic lattice pattern can be projected by a DMD, nevertheless some constraints, which might not be satisfied *a priori* or might be hard to achieve practically, have to be established in order to employ it in atomic physics experiments. These requirements are reported below

- In order to trap efficiently the atoms, a lattice potential should have sites deep enough to provide the necessary dipole potential energy to avoid, with a certain probability, the atoms "escape".
- The projected pattern should be as close as possible to the analytical one.
- If, for instance, measurements which involve the inter-sites tunneling probability have to be carried out, then the depth of each lattice sites has to be constant.
- For the most common lattice applications, a reasonable sites number is requested.

A 2-D lattice were supposed to be created with almost 30 sites per side and lattice pitch of $1\ \mu\text{m}$, manipulating the intensity profile of a laser beam mode TEM_{00} at $759\ \text{nm}$ ¹¹. This means that the final pattern would have the dimensions of $(30\ \mu\text{m} \times 30\ \mu\text{m})$. Obviously, due to the DMD mirrors size (see Sec. 2.1), a projection system which performs a demagnification needs to be implemented. In the future, that system will be composed by a telescope 1 : 3 coupled with an objective 80X, for an overall demagnification of 240X. Therefore in the "DMD frame" (reference system defined by the DMD), the pattern would be $(7.2\ \text{mm} \times 7.2\ \text{mm})$, i. e. about $(527\ \text{pixels} \times 527\ \text{pixels})$. Hence for each single site almost 18 micromirrors would be available to manipulate the intensity profile. It is a reasonable number of pixels: if this number were smaller, then the final pattern would suffer from

¹⁰If the iris diameter were smaller than 8.2 mm, it would be the spatial filter itself to limit the resolution and not the objective.

¹¹See Sec. 6.2 for a practical application of this kind of pattern. For further information on the laser source, see Sec. 2.2.

lack of precision because the intensity profile would assume a "step" aspect (see Chap. 3); at the same time, the pixels number should not be too large because, otherwise, a sufficient sites number would be impossible to create for absence of micromirrors. In this sense, a satisfying trade-off must be reached by choosing carefully the overall demagnification, the sites pitch and the patterns dimension as a function of the intrinsic characteristics of the device.

Now, a constraint on the site depth should be imposed. Normally the height of a lattice is measured in unit of recoil energy, which is the energy that an atom would gain by absorbing a lattice photon

$$V_{\text{dip}} = s E_{\text{rec}} \quad (2.10)$$

where

$$E_{\text{rec}}(\lambda) = \frac{1}{2} \frac{\hbar^2}{m} \left(\frac{2\pi}{\lambda} \right)^2 \quad (2.11)$$

which is equal to 96.2 nK for Ytterbium atoms at $\lambda = 759$ nm (the magic wavelength, see Sec. 1.1).

The desired lattice should be deep and have almost $s = 30$: with this lattice depth, a sample of ultra-cold atoms can be considered trapped with a tunneling time much greater than the experimental cycle time. In approximation of deep lattice (satisfied, for example, by systems in Mott insulating phase, which is the starting point for ideal quantum register implementation. See Sec. 1.4), the tunnelling probability can be estimated with the following formula [67]

$$\Gamma = \frac{1}{\hbar} \frac{4}{\sqrt{\pi}} E_{\text{rec}} \left(\frac{V_{\text{dip}}}{E_{\text{rec}}} \right)^{3/4} e^{-2 \left(\frac{V_{\text{dip}}}{E_{\text{rec}}} \right)^{1/2}} \quad (2.12)$$

For Ytterbium atoms trapped in a lattice created by a laser at 759 nm and with depth of $s = 30$, $\Gamma = 6.36$ Hz; in other words, an atom can tunnel between adjacent sites of the potential every 157 ms, a time interval longer than the experimental cycle duration.

The laser mode TEM_{00} has an intensity profile described by

$$I(r, z) = \left(\frac{2P}{\pi w(z)^2} \right)^2 e^{-\frac{2r^2}{w(z)^2}} \quad (2.13)$$

where P is the overall power carried by the laser beam, r is the radial distance from the center axis, z is instead the axial distance from the beam waist and $w(z)$ is the radius at which the intensity drops $1/e^2$ of its axial value.

If the squared pattern for creating the lattice is supposed to be displayed in

2. DMD characterization

the center of the DMD Active Area and the incoming beam hits in its center, then a constraint on the waist could be obtained: actually, the central area of the beam, delimited by its waist, should cover completely the pattern till its farther points, that is the vertexes. Hence, in the DMD frame, the minimum waist would be

$$w_{\min} = \sqrt{2} \left(d \frac{n}{2} \right) \chi \simeq 5.1 \text{ mm} \quad (2.14)$$

where $d = 1 \mu\text{m}$ is the lattice pitch, $n = 30$ is the sites number and $\chi = 240$ is the overall demagnification.

In the end, depending on the desired lattice depth, a constraint upon the power P in Eq. 2.13 can be deduced. In the vertexes the local intensity $I(r, z)$ should be at least enough to guarantee the lattice depth. In mathematical terms, this condition can be expressed as follows

$$\frac{s E_{\text{rec}}}{C} = \left(\frac{2P}{\pi w(z)^2} \right)^2 e^{-\frac{2(n d/2)^2}{w(z)^2}} \quad (2.15)$$

where C is the proportional constant between the local intensity $I(\mathbf{r})$ and the dipole potential energy $V_{\text{dip}}(\mathbf{r})$ ¹² and r , the radial coordinate, has been rewritten in terms of n and d .

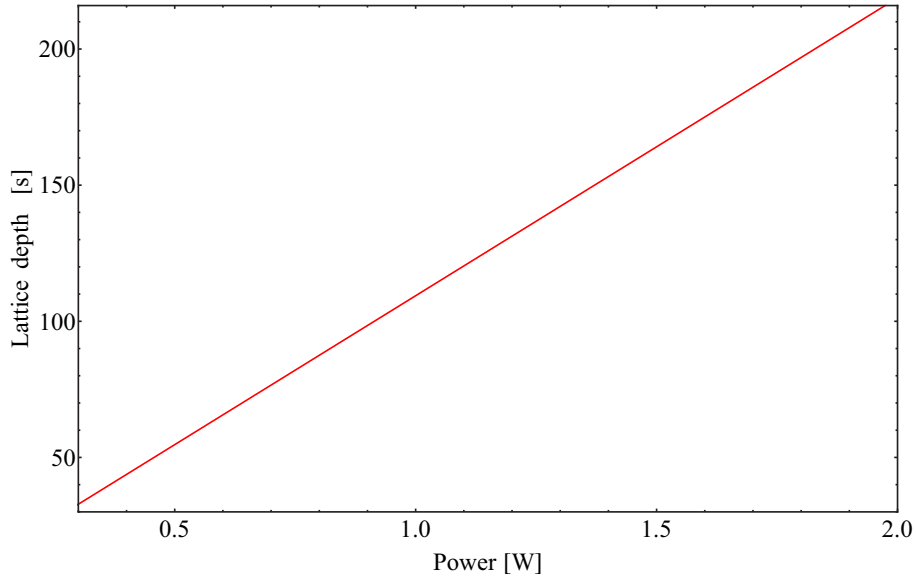


Figure 2.13: The lattice depth is plotted as a function of the incoming beam overall power. The waist has been kept fixed at w_{opt} and the sites number at $n = 30$. The losses due to the DMD and the projection system have not been considered in this graph.

¹²See Sec. 1.1 for further details.

Resolving for power P , Eq. 2.16 can be written

$$P = \frac{s E_{\text{rec}}}{C} \frac{\pi w^2}{2} e^{(\frac{dn}{w})^2} \quad (2.16)$$

So, the minimum power requested is $P = 370$ mW having taken into account the waist calculated previously. Nevertheless, from Eq. 2.16, the waist in the DMD frame which minimizes the power can be found

$$w_{\text{opt}} = dn \chi = 7.2 \text{ mm} \quad (2.17)$$

In Fig. 2.13, the linear dependence of the lattice depth on the power is presented.

This treatment is just theoretical: possible power losses due to the optical set-up (Sec. 2.2), the dithering (Chap. 3) and feedback process (Sec. 4.2) must be taken into account in operative phase. For the experimental results, see Sec. 5.3.

Chapter 3

Digitization of static patterns

A Digital Micromirror Device is able to statically project only black-and-white bitmaps, which are images with pixel-depth equal to one, as anticipated in Sec. 2.1. Nevertheless, physics experiments could require the projection of smoothed patterns, as lattices, which are instead represented by gray-scale images. In order to reduce them into two-colors bitmaps, digitization methods can be used.

Generally, the digitization methods are mathematical operations applied to the data matrices¹ which describe the raster images. In Sec. 2.1, the simple Round method has been introduced: it consists in rounding all the data of an image matrix normalized in the range $(0, 1)$ to 0 (white pixel) or 1 (black pixel). The Round digitization method is an image binarization process and the starting point of dithering algorithms (see Sec. 3.1).

In Fig. 3.1, Lena's portrait is proposed again along with its Rounded version. As can be seen, the original image (having a pixel-depth of 8 bits, i. e. 256 colors) has been transformed into a one-bit image.

Other digitization methods have been implemented, as dithering algorithms. In the first section of this chapter, two dithering algorithms will be described: Floyd-Steinberg and serpentine Floyd-Steinberg algorithms. The second and third sections present the results of the application of these three digitization methods presented on Flat-top and lattice patterns, respectively. In the last section, instead, a quantitative comparison between these methods will be reported in order to select the best algorithm for the aims requested in physics experiments.

¹The image data matrix on which this operations are applied are usually normalized in the range $(0, 1)$.



Figure 3.1: Left, Lena's portrait. Right, its rounded version.

3.1 Dithering and error diffusion

"Dither" is a graphic elaboration technique which consists in randomizing the quantization errors produced during the binarization process (i. e. the application of the round method described above) applying on purpose a form of noise or performing an "error diffusion", that is the distribution of the quantization errors to the image pixel values. Dither converts a given grey-scale image to a black-and-white bitmap, so that the density of the black pixels in the new picture approximates the average level of grey in the original one.

Several algorithms designed to perform dithering have been developed, but the most popular is certainly the Floyd–Steinberg (FS) one [24]. With its aid, the visual artifacts produced through the binarization process are minimized by the error diffusion.

The operating principle of the Floyd-Steinberg algorithm involves the redistribution of the error made by rounding a pixel value to the closest integer (0 or 1) to certain neighbour pixels with different weights², as depicted in Fig. 3.2.

In mathematical terms, the Floyd-Steinberg algorithm is shown below.

$$\begin{bmatrix} I_{(i-1,j-1)} & I_{(i-1,j)} & I_{(i-1,j+1)} \\ I_{(i,j-1)} & I_{(i,j)} & I_{(i,j+1)} \\ I_{(i+1,j-1)} & I_{(i+1,j)} & I_{(i+1,j+1)} \end{bmatrix} =$$

²With any error diffusion algorithm, every pixel value (except the initial one) is correlated to the neighbours ones.

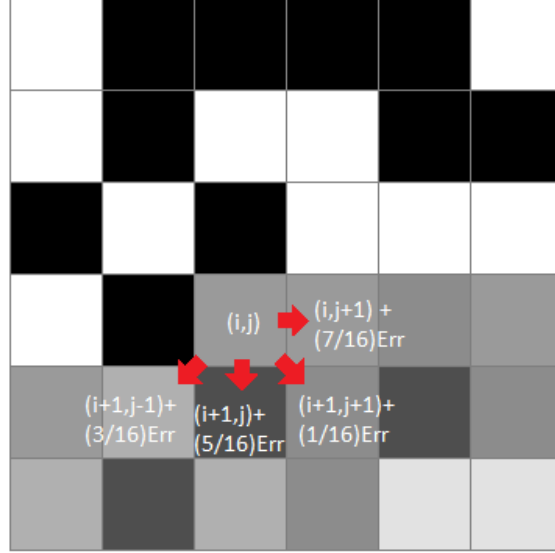


Figure 3.2: Graphic representation of the Floyd-Steinberg algorithm.

$$\begin{bmatrix} I_{(i-1,j-1)} & I_{(i-1,j)} & I_{(i-1,j+1)} \\ I_{(i,j-1)} & I_{(i,j)} & I_{(i,j+1)} \\ I_{(i+1,j-1)} & I_{(i+1,j)} & I_{(i+1,j+1)} \end{bmatrix} + \begin{bmatrix} 0 & 0 & 0 \\ 0 & 0 & \frac{7}{16} \\ \frac{3}{16} & \frac{5}{16} & \frac{1}{16} \end{bmatrix} \text{Err}$$

where

$$\text{Err} = I_{(i,j)} - \text{Round}[I_{(i,j)}]$$

and $I_{(i,j)}$ is the value contained in the image matrix "I" (normalized in the range $(0, 1)$) at the i -th row and j -th column, while $\text{Round}[I_{(i,j)}]$ is a function which rounds the $I_{(i,j)}$ value to 0 or to 1.

The weights which multiply the "Err" have selected in order to transform a grey image (having each pixel value equal to 0.5) into a black-and-white chequerboard. An example of image created with this algorithm is reported in Fig. 3.3 (left).

The first pixel to be processed is the topmost left, then the algorithm proceeds in row-major order. In this classical version of the Floyd-Steinberg algorithm, the error is propagated from the top-left corner to the opposite one. For this reason, as highlighted in [64], the pictures created by this dithering algorithm suffer from directional "worm" features and other disturbing distortions which occur for those patterns close to the perfect chequerboard with 50% grey (see Fig. 3.4).



Figure 3.3: Left, Lena's portrait created from the original portrait (fig. 3.1, to the left) by the standard Floyd-Steinberg algorithm. Right, the version of the portrait elaborated by the Serpentine Floyd-Steinberg algorithm.

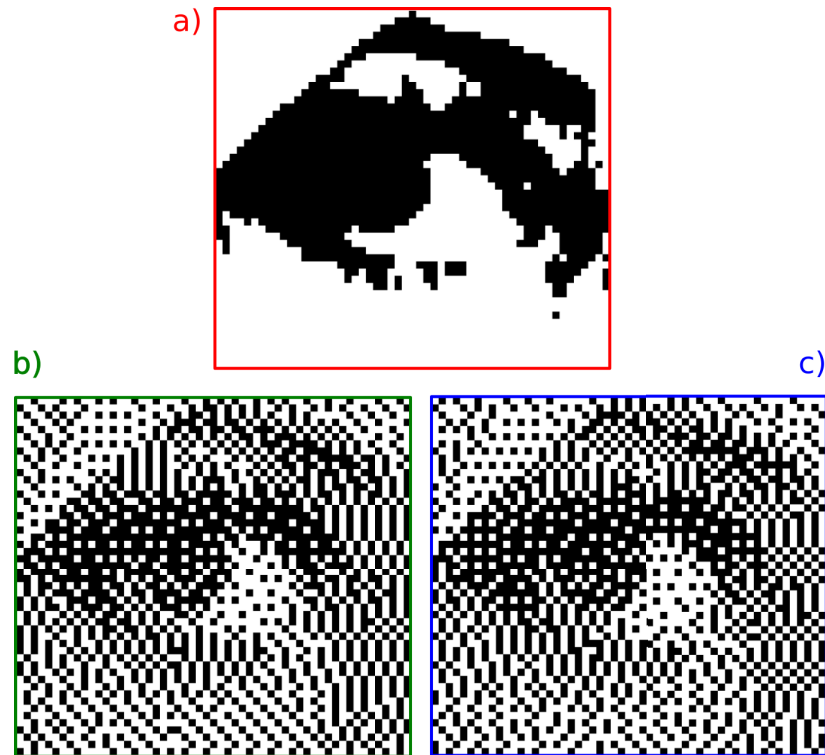


Figure 3.4: Pictures above report the same detail (right eye) from the different versions of Lena's portrait. a) Rounded version. b) Classical FS version. c) Serpentine FS version. In b), mostly in the lower part, the presence of the "worm" can be noticed, partially resolved by the Serpentine FS algorithm as can be seen in c).

In order to break up these structures that would occur as unwanted texture, the input image is processed in the row-major order but alternating the column order between column-major and column-minor order. In other words, this means that after having scanned the first row, from the first column to the last one, the second row is processed starting from the last column up to the first one. This version of Floyd-Steinberg algorithm is called Serpentine version. An example of image produced by this method is reported in Fig. 3.3 (right).

Root-Mean-Square error In order to quantitatively establish how much a one-bit version of an image is similar to the original, a parameter ϵ_{RMS} can be associate to each picture³, defined as the Root-Mean-Square error of the variances of every single pixel as expressed in Eq. 3.1.

$$\epsilon_{\text{RMS}}[\%] = 100 \sqrt{\frac{1}{IJ} \sum_{(i,j)}^{(I,J)} \left(\frac{T_{(i,j)} - D_{(i,j)}}{C} \right)^2} \quad (3.1)$$

where "T" and "D" are the data matrices of the initial image and its dithered version, respectively, I (J) is the total number of the images rows (columns), while "C" is the difference between the image maximum and minimum values⁴.

Tab. 3.1 reports the ϵ_{RMS} for the three final versions of Lena's portrait; the last two are similar to each other, as could be noticed.

| Image version | ϵ_{RMS} [%] |
|----------------------------------|-----------------------------|
| Lena, Rounded | 36.10 |
| Lena, Floyd-Steinberg | 46.20 |
| Lena, Floyd-Steinberg serpentine | 46.22 |

Table 3.1: Root-Mean-Square Errors for the the three versions of Lena's portrait.

In general, the ϵ_{RMS} of Rounded versions is tightly related to the average level of the original image: the greyer the initial figure is, the higher the error. It can assume values between 0% – initial image having only completely white or black pixels – or 50% – the initial image is completely grey (each pixel value equal to 0.5) –, so it could be interpreted as an index of "how much" an image is grey.

³The ϵ_{RMS} provides a "local" error which can not be used in order to select the best dithering algorithm among the ones presented. See Sec. 3.4 for further details.

⁴The sum is extended over the image pixels, therefore, in the case of Flat-tops, only the pixels of the plateau will be considered and the "C" will be ignored.

3.2 Flat-tops

A digital Flat-top image is a totally black pattern with a central and (usually) squared bright area, whose pixels show the same level. This pattern is very useful if a laser beam with an uniform and flat intensity profile is desired (see Sec. 5.2 for the experimental results).

An example of Flat-top is reported in Fig. 3.5, image a). In this work, Flat-tops have been created by displaying on the DMD Active Area a squared figure with steep edges and the same values for each pixel which forms it. In others, e. g. in [22], this pattern is simulated by a 2-D density-plot of a super-lorentzian function.

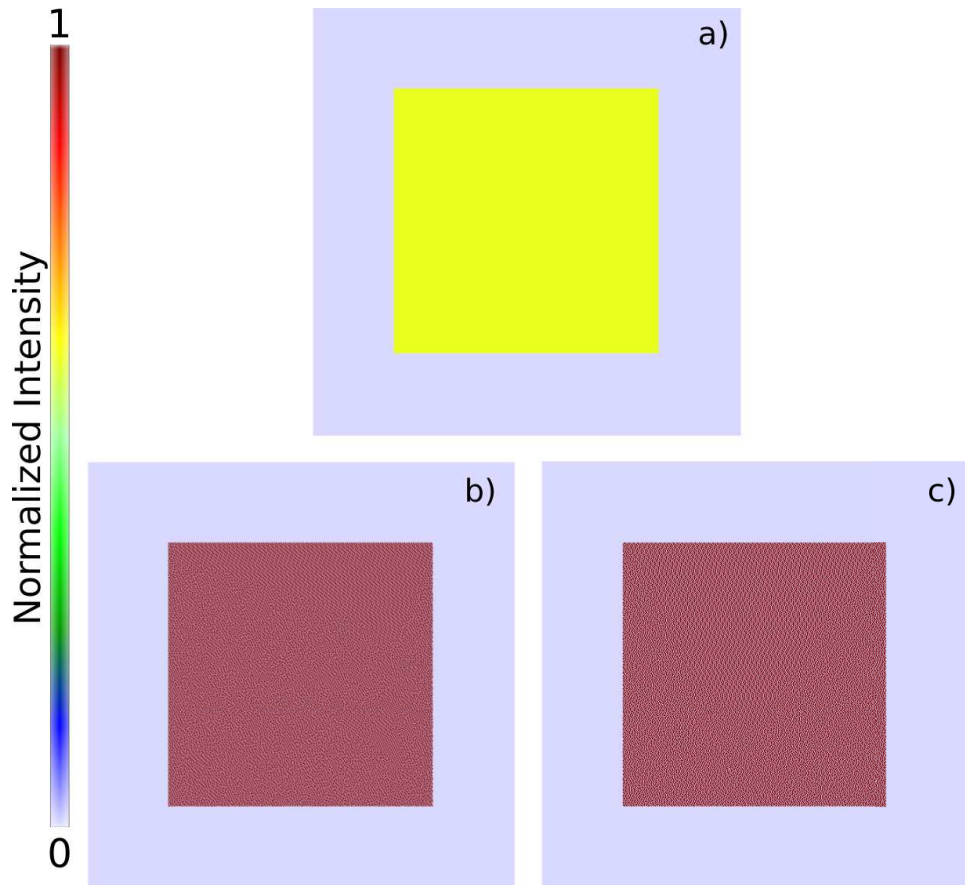


Figure 3.5: a) Example of Flat-top. The 300^2 central pixels which form the squared figure have values equal to 0.6 in the usual scale where 0 stands for black and 1 for white. b) Its standard FS version. c) Serpentine Floyd-Steinberg version. Only the central (500×500) section of the patterns has been reported.

Fig. 3.6 reports the ε_{RMS} , evaluated via Eq. 3.1, as a function of the gray level (value of the pixels which form the central squared pattern) of the

one-bit Flat-top versions obtained through the dithering method presented in Sec. 3.1.

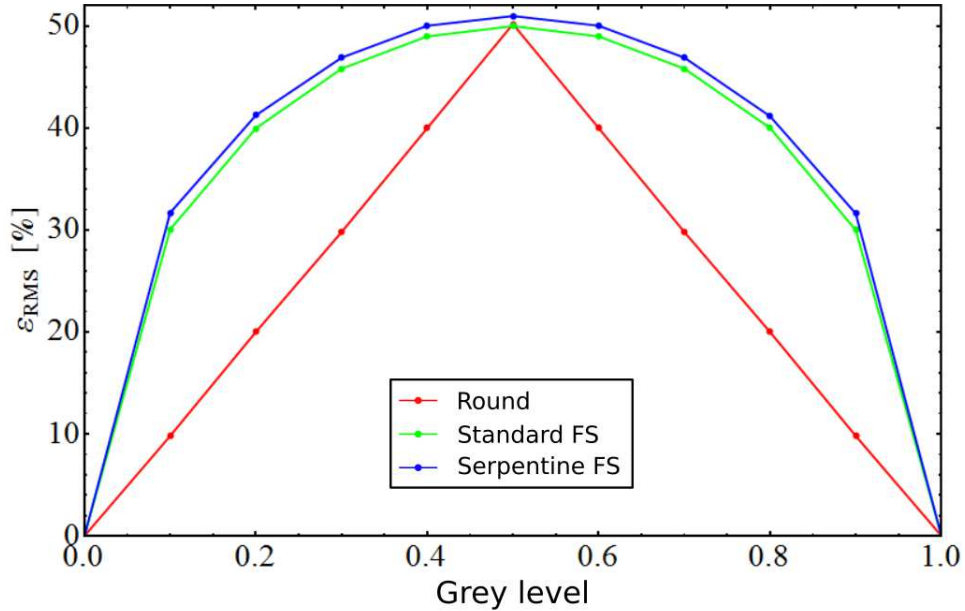


Figure 3.6: Dithering errors for Flat-top images as a function of gray level in the usual scale where 0 represents the color black and 1 the color white.

The Flat-top images with a grey level equal to 0 or 1 are already binary images: the versions created by the application of the digitization methods are identical to the initial one, so the ϵ_{RMS} is null. The Rounded version errors exhibit a linear trend: this is due to the fact that the Eq. 3.1 compares the initial grey-scale Flat-tops image to the same result of the dithering process. Actually, for gray levels smaller than 0.5, the final Rounded version image is a completely black image; whereas for gray levels equal or bigger than 0.5, the resulting image is a Flat-top with value of the pixels which form the central squared pattern equal to 1.

The green and blue tracks show a similar trend: this means that the two algorithms return almost the same results in absence of articulated structures in the original image, as in this case.

3.3 Lattices

A periodical modulation of the incoming laser beam intensity could be achieved by displaying on the Digital Micromirror Device screen a 2-D density-plot image of the function reported in Eq. 3.2. This intensity profile can be used in order to create an optical lattice potential on atoms as discussed in Sec. 2.5. Fig. 3.7 reports an example of a lattice density-plot with 128 pixels per site and its digitized versions.

$$L(x, y) = \frac{1}{2} (\sin^2(x) + \sin^2(y)) \quad (3.2)$$

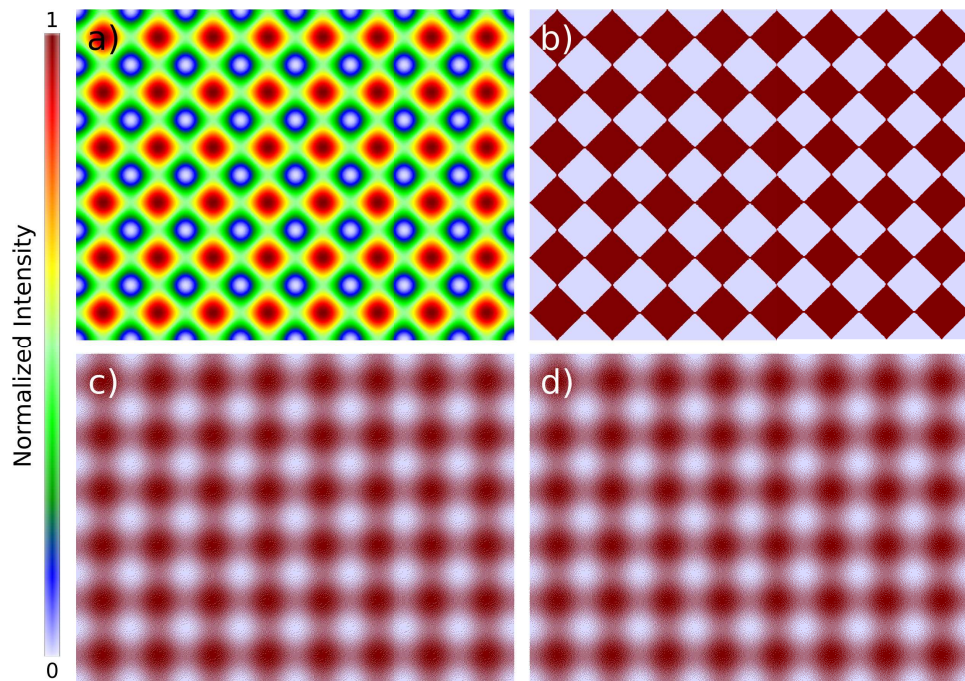


Figure 3.7: An example of lattice a) with 128 pixels per site. b) Its Rounded version. c) Standard Floyd-Steinberg version. d) Serpentine FS version.

A density-plot is a two-dimensional representation of a two variables function (as Eq. 3.2), where the values assumed by the function are represented by a color of a defined color-scale. Such image can be described by a matrix (as a raster picture), whose elements correspond to the values returned by the function evaluated at the coordinates (i, j) , that is the position of the matrix elements. The analytic function has to be evaluated in a finite number of samples equal to the elements number of the matrix, so the density-plot is itself a first approximation of the function.

In addition to this, the errors introduced by the digitization process have

to be considered too. Fig. 3.8 shows a one-dimensional example of the approximations introduced by the discretization of the analytic function and by the dithering processes.

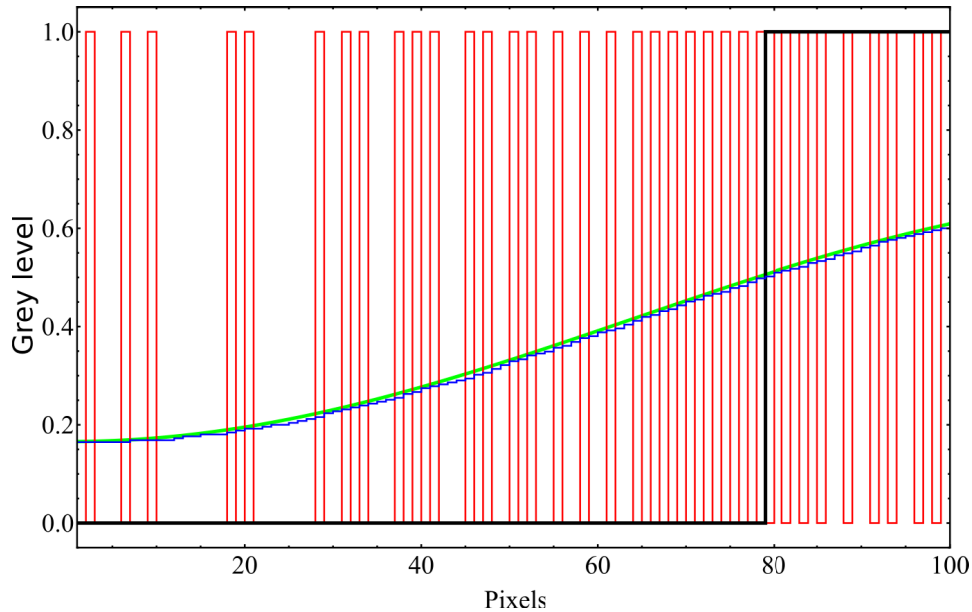


Figure 3.8: In green, the analytic function. In blue, its discretized version. Round and serpentine FS versions of the blue track are reported in black and red, respectively. The grey levels are normalized in the range $(0, 1)$.

A 1-D profile of the lattice function Eq. 3.2 with 256 pixels per site is plotted in green in Fig. 3.8, while the values of the corresponding array are reported in blue through a "step-function" which assumes the constant value of a pixel over the pixel length: it is a first and "intrinsic" approximation of the analytic function reported in green. The profile of the serpentine Floyd-Steinberg version is reported in red. Around the 80-th pixel, the target profile (green) approaches values near to 0.5, so the values assumed by the red plot are alternately equal to 0 and 1, in accordance with the operating principle of this dithering algorithm. The black profile represents the Rounded version of the initial curve and exhibits a sudden jump from 0 to 1 where the target line reaches the value 0.5, as can be expected.

Fig. 3.9 reports the plots of the Root-Mean-Square errors for the three kinds of digitization methods previously under analysis as a function of the mirrors number per site. As can be seen, the traces show the same trend, but the Rounded version errors are lower of about 23% with respect to the other two. Moreover, the errors are pretty constant with the number of micromirrors per site (MPS), when this number drops below 10 MPS: independently of the algorithm employed, a lower number of MPS causes

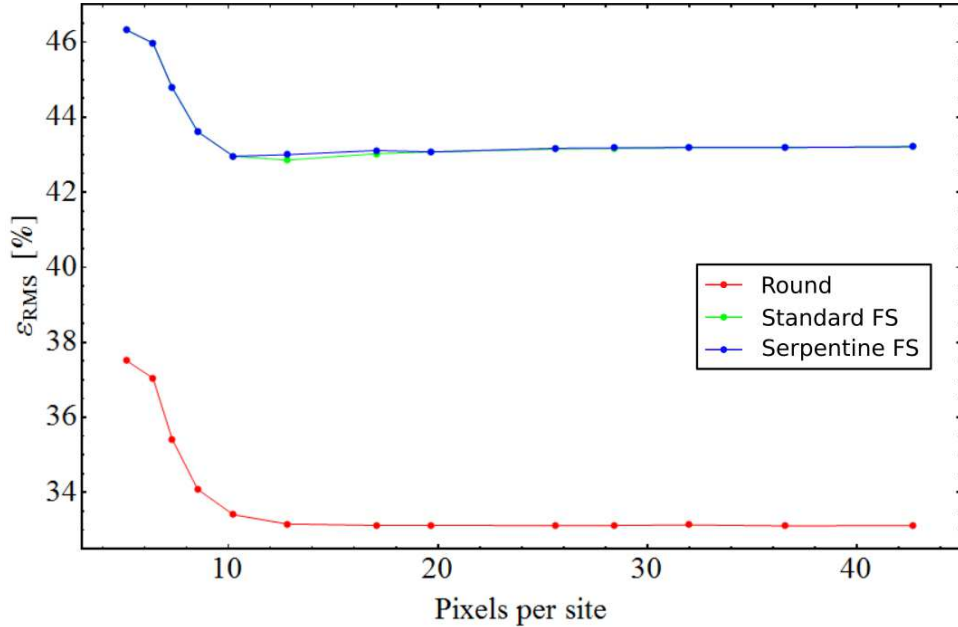


Figure 3.9: Dithering errors for different lattices. The red track refers to the Rounded version, the green one to the classical Floyd-Steinberg version and the blue one to the serpentine Floyd-Steinberg version.

a Root-Mean-Square error increase of about 12% for the Rounded version and of about 9% for the other two dithered versions. The standard and serpentine FS versions traces are practically coincident: it is reasonable to presume that these two dithering algorithms show appreciable differences only for non-periodical and structured initial images.

The Root-Mean-Square errors presented in Fig. 3.9 have been calculated via Eq. 3.1 without taking into account the intrinsic approximation due to the discrete nature of the data matrix standing for the density-plot image. This systematic error has been evaluated via Eq. 3.3.

$$\varepsilon [\%] = 100 \sqrt{\frac{1}{N^2} \int_0^N dx \int_0^N dy \left(\frac{I(x,y) - L(x,y)}{C} \right)^2} \quad (3.3)$$

where " $I(x,y)$ " is the step function created with image matrix: for all the values contained between (i,y) and $(i+1,y)$, " $I(x,y)$ " returns the value of the function " $L(x,y)$ " (Eq. 3.2) evaluated in (i,y) . The same holds for the ordinates. " C " is instead the difference between the " L " matrix data maximum and minimum, while N is the number of pixels per site. The integral is extended only over one lattice site. From their own definition, it is clear that the errors are meant per single pixel.

Fig. 3.10 shows the errors obtained through Eq. 3.3 as a function of the pixels number per lattice site: with this number decreasing, the volume

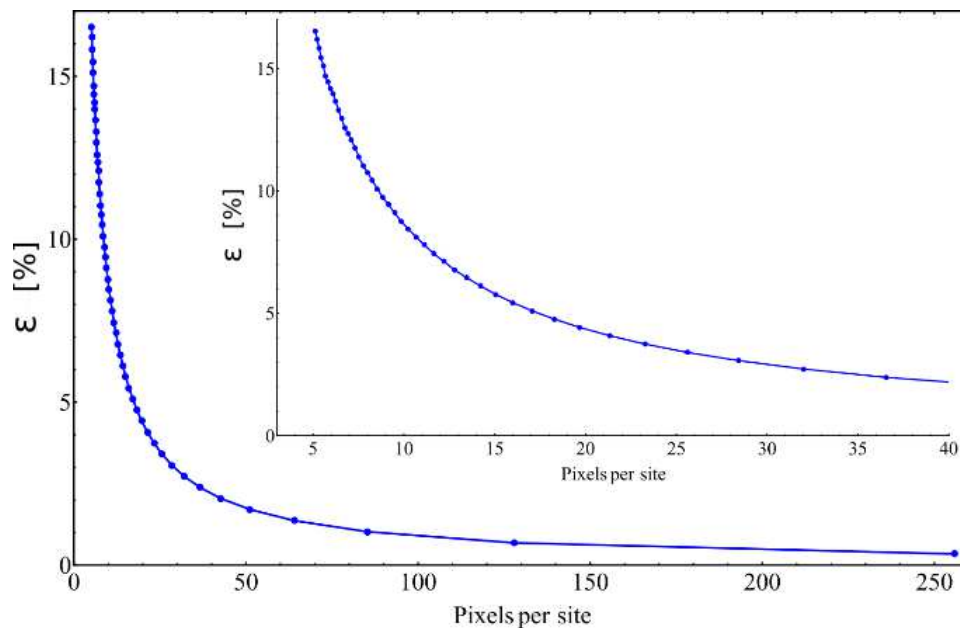


Figure 3.10: Systematic errors between the exact lattice function and its graphical representation.

between the two curves increase, so does the error.

3.4 Selection of the best dithering algorithm

It is now worth asking the question: which is the best digitization algorithm among the ones presented in this chapter? If the judgement were based only on the value of ϵ_{RMS} expressed in Eq. 3.1, then the Rounded version would be the best, even though the final images which produces are the worst in terms of global fidelity in the "far field", as can be noticed in Fig. 3.7 or comparing Fig. 3.1 with Fig. 3.3. The key point is that the diffraction limit of the experimental set-up (see Sec. 2.4) has to be taken into account when dithered images are projected: actually it reduces or eliminates the high frequency features of the images, exalting the lower frequency components. The atoms interacting with the optical lattice potentials created by projecting this kind of patterns with the DMD will not be influenced by structures of dimensions below the diffraction limit.

Considering the set-up diffraction limit effects, the Discrete Fourier Transform expressed in Eq. 2.7 in Sec. 2.3 can be an useful tool to obtain a better quality estimation. In Fig. 3.11 the Fourier spectra of the lattice and its three dithered version presented in Fig. 3.7 are reported.

In order to evaluate the Root-Mean-Square error considering the diffraction limit of the optical system, the procedure described below has been followed.

- The difference between the lattice image and its dithered version is achieved by subtracting their data matrices.
- A Discrete Fourier Transform of the difference image is performed. Fig. 3.12 shows the magnitude diagram of the result.
- A circular low-pass filter is applied to the Fourier spectrum: practically, this means to crop the image out of a circle centred in the lowest frequency of the difference spectrum and having a radius which corresponds to a length in the real space equal to the diffraction limit of the optical system, i. e. $92.5 \mu\text{m}$ on the DMD Active Area (see Sec. 2.4). In this way only the features which the optical system is able to resolve are taken into account.
- The filtered spectrum is Fourier Anti-transformed.
- The error ϵ_{RMS} is estimated via the following formula

$$\epsilon_{\text{RMS}}[\%] = 100 \sqrt{\frac{1}{N_W N_H} \sum_{(i,j)=(1,1)}^{(N_W, N_H)} D(i,j)^2} \quad (3.4)$$

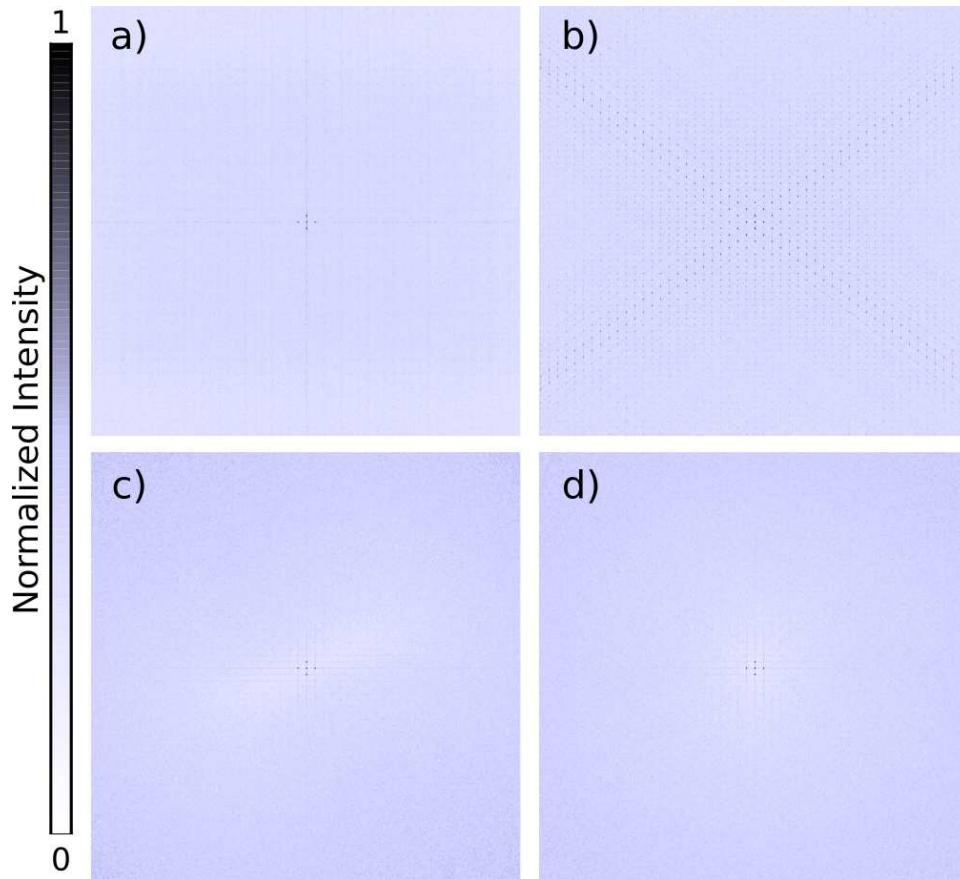


Figure 3.11: a) Discrete Fourier Transform of a lattice having 128 pixels per site. b) DFT of its Rounded version. c) DFT of its standard FS version. d) DFT of its serpentine Floyd-Steinberg version. Every image is an enlargement of 400×400 pixels taken in the central region of the entire Fourier spectrum. This for better appreciating the difference at low frequencies between the spectra.

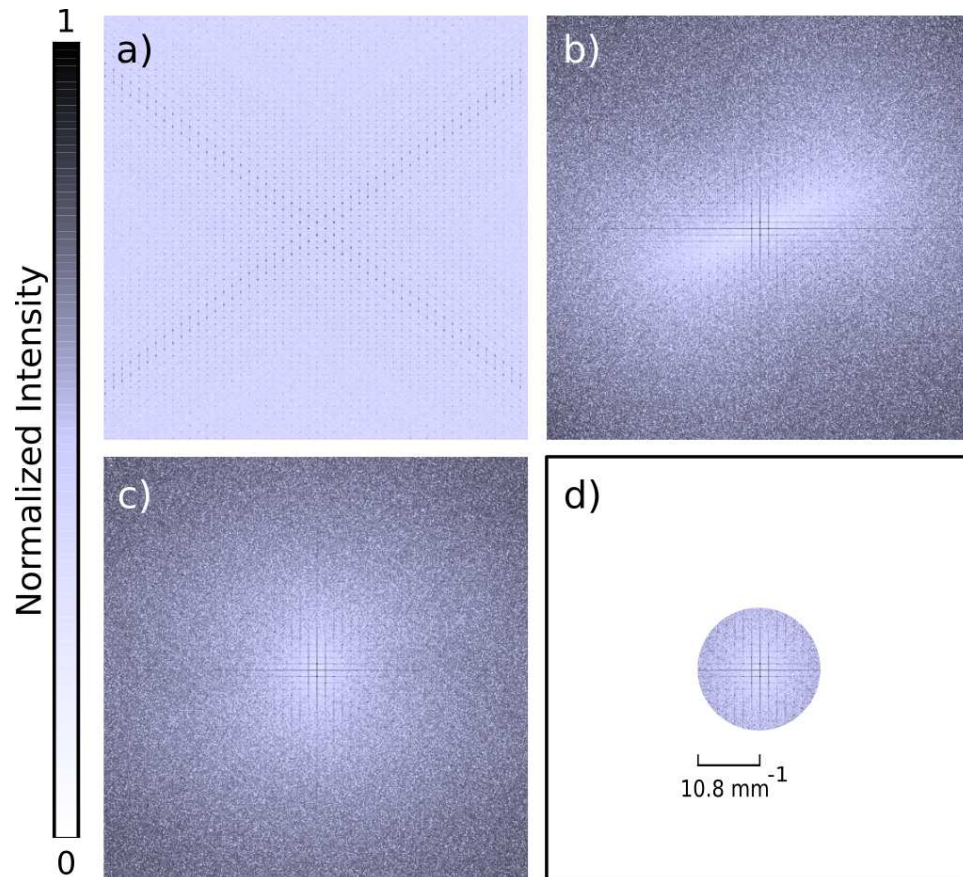


Figure 3.12: DFT of the differences between the lattice image and its three dithered versions. DFT of the difference with the Rounded a), standard FS b) and serpentine FS c) versions. d) Application of a circular low-pass filter to the c) difference spectrum with radius equal to the cut-off frequency corresponding to the set-up diffraction limit. The central (400×400) pixels region of the spectra has been reported.

3.4. Selection of the best dithering algorithm

where N_W and N_H are the pixel numbers along the horizontal and vertical dimension, respectively, and "D" is the data matrix standing for the filtered difference image.

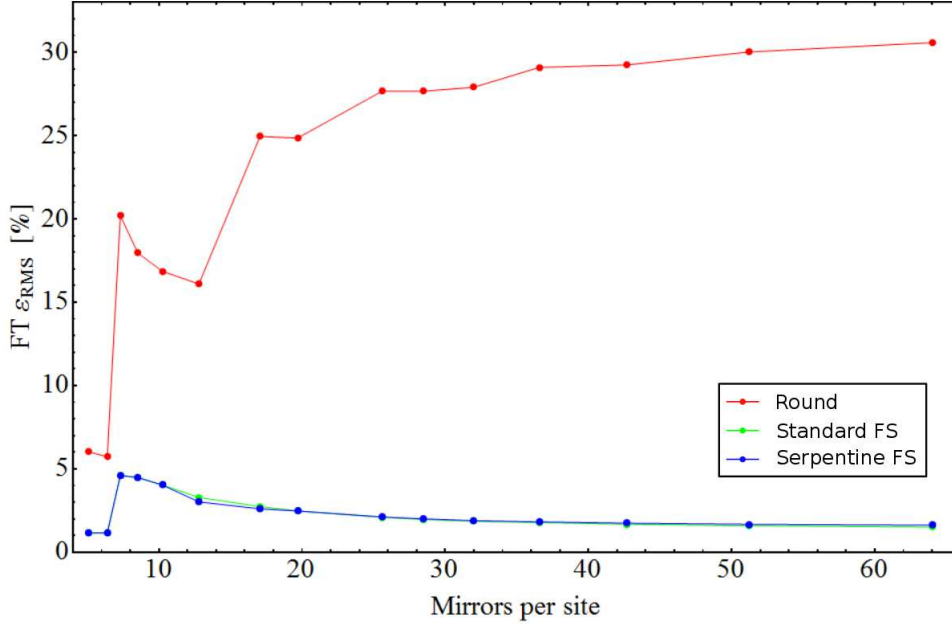


Figure 3.13: Root-Mean-Square errors of DFT difference between a lattice image and its dithered versions.

The ϵ_{RMS} trends for the three kinds of dithering algorithms are reported in Fig. 3.13. It is now clear that the Floyd-Steinberg dithering (in its two versions) is definitely better than the rough Rounded version of the lattice image for applications in atomic physics: for this reason, the serpentine FS version⁵ is the algorithm used in this work for preparing the images to be loaded into DMD Memory Board.

⁵Serpentine Floyd-Steinberg version has been chosen over the classical one for its ability in avoiding the creation of "worm" sub-structures.

Chapter 4

Control program and feedback process

In the first section of this chapter, the program developed during this work in order to control the DMD, the images projection and its features will be presented. Moreover, this program is able to perform a feedback process – described in the second section – on the projected patterns: through this method, images defects and errors due to the experimental set-up can be corrected. In the third section, the calibration procedure of the DMD image on the CCD screen will be explained.

4.1 "DMD Easy"

The DMD comes with a Dynamic-Link Library (DLL) and a stand-alone program. Nevertheless, the latter is not sufficient for the degree of control, both static and dynamic, required in typical atomic physics experiments. Indeed, for example, it is not possible to create sequences with more than five frames and no feedback system is embedded.

In this work, a program provided with a Graphic User Interface (GUI) has been developed on LabWindowsTM/CVI platform, which is an ANSI C programming environment for measurement, designed by National Instruments. This program has been named "DMD Easy". A screen shot of its main interface is shown in Fig. 4.1. The DLL released by ALP contains a set of useful functions which carry out the principal tasks required to a DMD¹: most of these have been implemented in "DMD Easy".

After having read the data matrix of the images to be projected, with the aid of the pre-written functions, "DMD Easy" is able to organize them in sequences to load in the DMD Board Memory. Afterwards it can start and

¹In [30] a complete handbook of the functions present in the DLL can be found with their explanation.

4. Control program and feedback process

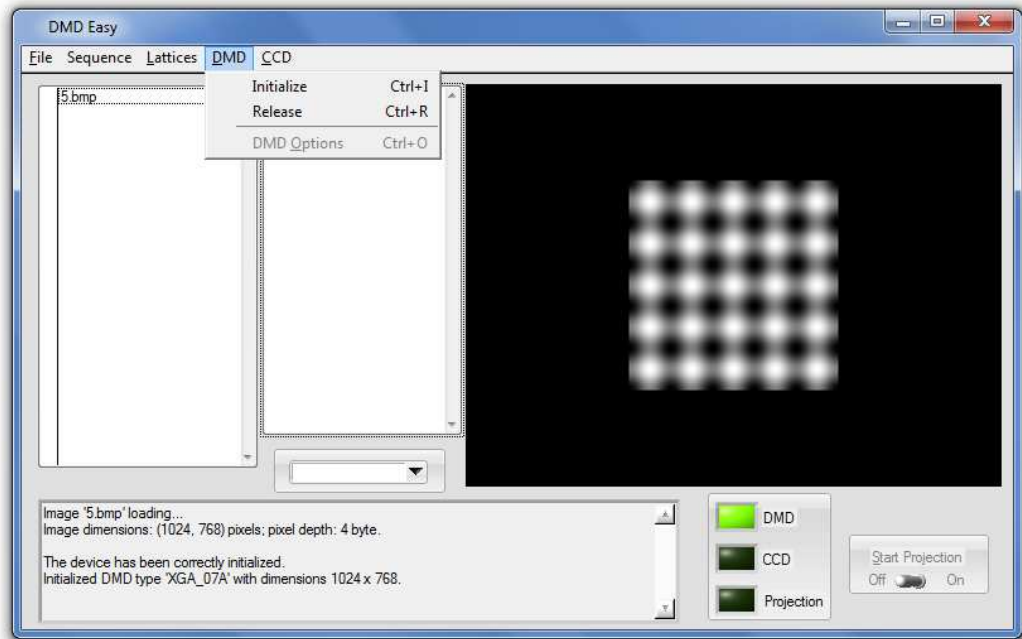


Figure 4.1: "DMD Easy" main interface, developed during this work.

interrupt the projection, as well as delete the sequences or directly free all the memory in order to provide memory for new images. "DMD Easy" can also control the timing options described in Sec. 2.1: the user can choose and set the values of the Illuminate Time and the Picture Time² or decide to select the "uninterrupted projection" mode. The timing option panel is shown in Fig. 4.2.

In this panel two projection options can be chosen by the user: with the "shot" mode on, the different frames in a certain sequence can be projected for $IT \mu s$ in succession, one after another, as slides in a presentation; otherwise, with the "scroll" mode selected, the different frames can flow on the DMD screen in a continuous flux. With the scrolling mode activated, the first frame of the sequence is projected. After an IT, the first "Line Increment" lines are eliminated. Consequently, the remaining rows are shifted to the top of the screen, while the last "Line Increment" lines are occupied by the first "Line Increment" ones of the successive frame.

This features are very important in applications where the dynamic control of the trapping potentials is required, e.g. Bragg scattering or quantum computation experiments (see Chap. 6).

²The Dark Phase is automatically calculated on the basis of IT and PT values.

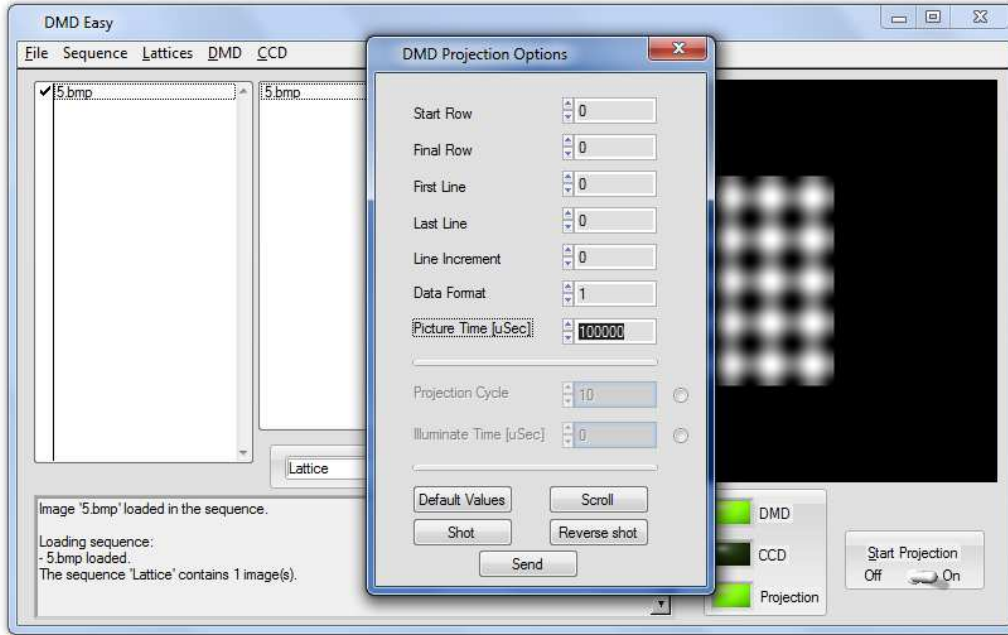


Figure 4.2: "DMD Easy" timing option panel.

4.2 Feedback process

There is no doubt that the greatest challenge in programming "DMD Easy" has been the implementation of a function – with all its satellite sub-functions – which is able to perform a feedback on the static images that are projected. Its dedicated panel is shown in Fig. 4.3. The relevance of this feature is evident in atomic physics applications, where "non-ideal" real beams and optical systems are employed. Deviations from the ideal laser beams could introduce detrimental noise and/or uncontrolled features in the projected potential which can in turn mask or destroy the physical phenomena under investigation.

Generally a beam of light incident on the DMD surface has its own intensity profile. For instance, an ideal TEM₀₀ laser mode has a gaussian shape, whose formula is re-proposed here

$$I(r, z) = I_0 \left(\frac{w_0}{w(z)} \right)^2 e^{-\frac{2r^2}{w(z)^2}} \quad (4.1)$$

where I_0 is the intensity at the center of the beam, r is the radial distance from the center axis, z is instead the axial distance from the beam waist – indicated by w_0 – and $w(z)$ is the radius at which the intensity drops $1/e^2$ of its axial value I_0 .

The DMD allows for a spatial modulation of the intensity profile: it

4. Control program and feedback process

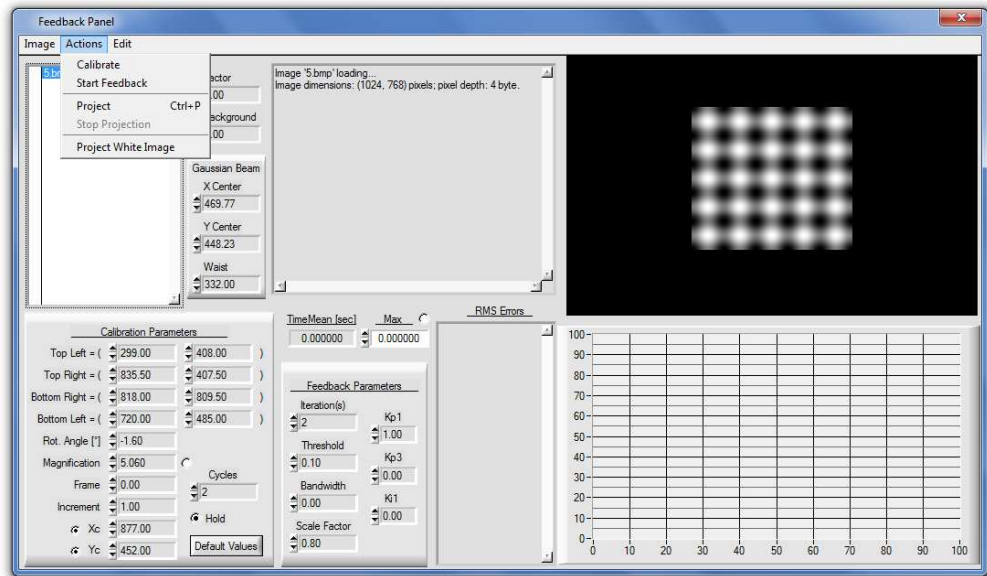


Figure 4.3: "DMD Easy" feedback panel.

can reflect the portion of the beam incident on the single pixel towards the "image" direction or the "dump" one, but it can not redistribute the light on a pixel over the others. For this reason, any preceding shape of the intensity profile remains superimposed on the modulation made by the DMD: for example, this means that loading and projecting a Flat-top will not produce an uniform intensity profile (see Fig. 4.4).

Nevertheless, as said, it is very important to be able to produce such a beam (uniform in intensity) or in general to get rid of the original beam profile, therefore a feedback mechanism has been implemented.

The basic idea of the feedback process is described below.

- After the target image has been projected, a single acquisition of the intensity profile is taken³ by CCD 1, whose model, position and other technical issues have already been discussed in Sec. 2.2.
- Typically the image projected by the DMD does not correspond to the whole active area of the CCD: it is smaller and its axes are not parallel to the CCD ones (see Fig. 4.5). Crop, Rotate and Resize operations are needed to adapt the captured photo to the Target Image: only after these manipulations, the two images (and, especially, the data matrices associated to them) can be compared.

³In order to control the CCD, functions of the relative DLL have been used. The library and its complete manual are freely released by the device producer and available on-line.

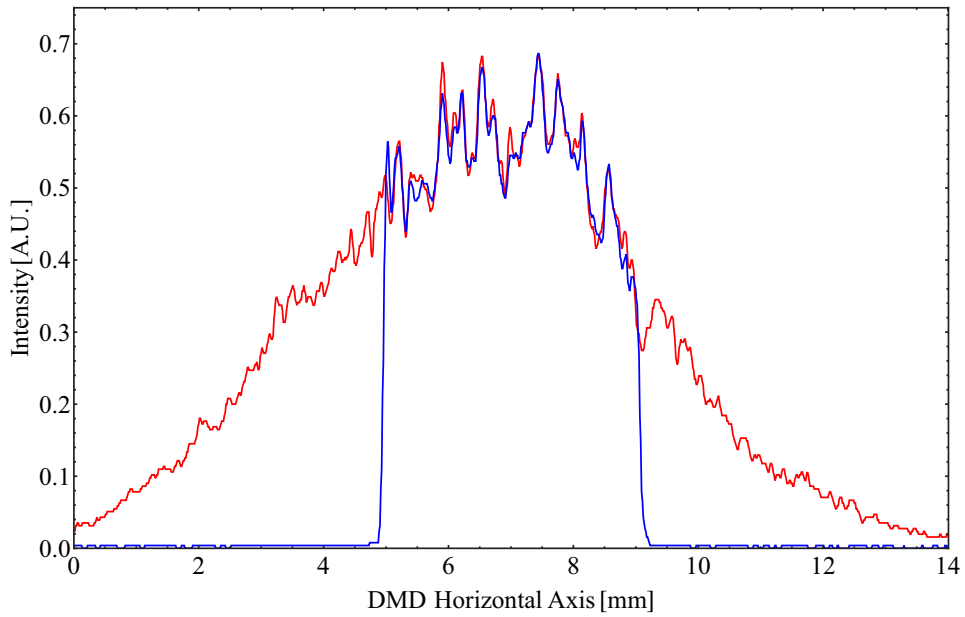


Figure 4.4: Flat-top (blue), squared with 300 pixels per side, and incident gaussian beam (red) profiles. The DMD selects the portion of incoming light to be reflected. As the profiles are related to two images taken at different times, they can slightly be different due to the residual instability of the optical system.

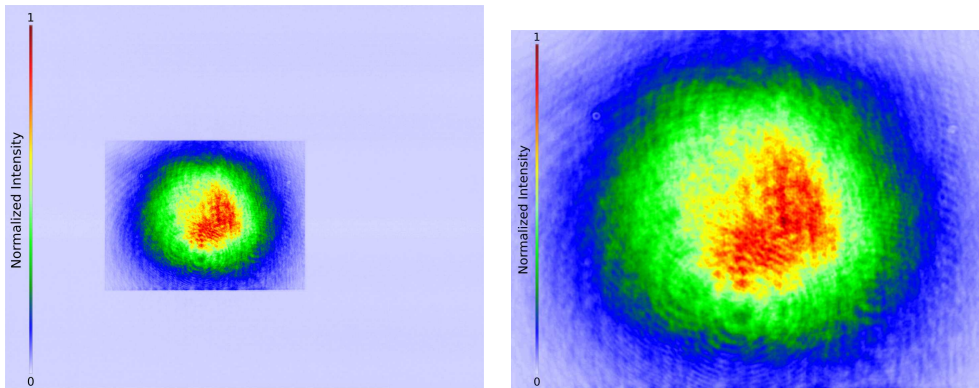


Figure 4.5: Left, an image captured by the feedback CCD is reported. The resulting image from the Cropping, Rotating and Resizing operations is shown to the right.

- Pixel by pixel, a matrix error is calculated as the difference between the target (fixed) and the acquired images matrices.
- The error is applied to each single pixel of the image previously loaded into the DMD Memory Board and currently on projection.
- The new image can be displayed and the feedback process can restart.

I. Image projection At this point, for the sake of clarity, it is worth reminding that the image displayed on the DMD screen represents the amplitude reflection coefficient, not the intensity profile desired. The reflection coefficient is a complex number expressing the ratio of the reflected to incident electric field amplitude, in contrast to the reflectance – the square of the reflection coefficient – which is the fraction of incident optical power that is reflected at the interface. In other words, before the projection, a grey-scale image (from now on named "Target Image") is prepared: it spatially represents the intensity in each point of the desired pattern. Then a squared root is performed on each value of the image data matrix in order to obtain the amplitude reflection coefficient mask. Finally, the image can be dithered, loaded into the memory and projected. Later, "DMD Image" will be the name referring to it.

II. Graphical elaboration of the acquired images As previously said, the frame captured by the CCD is incompatible with the "Target Image": a direct comparing would be impossible because their sizes are different and their sides are not aligned (see Fig. 4.5). Therefore Cropping and Rotating operation (in "DMD Easy" performed together by the function *Rotate*) is applied. In Cod. 4.1, a part of its C-code is reported.

Code 4.1: A section of the function *Rotate*, which performs a rotation of an image via its data matrix.

```

1  for(row=-ySide; row<ySide; row++)
2  {
3      for(col=-xSide; col<xSide; col++)
4      {
5          newCol = col*cos(ang) + row*sin(ang)
6              + cntr.x;
7          newRow = -col*sin(ang) + row*cos(ang)
8              + cntr.y;
9
10         floorX = floor(newCol);
11         floorY = floor(newRow);
12
13         xVal = (Data[floorY][floorX+1]
14              - Data[floorY][floorX]) * (newCol-floorX)
15              + Data[floorY][floorX];
16
17         yVal = (Data[floorY+1][floorX]
18              - Data[floorY][floorX]) * (newRow-floorY)
19              + Data[floorY][floorX];
20
21         xValUp = (Data[floorY+1][floorX+1]
22              - Data[floorY+1][floorX]) * (newCol-floorX)
23              + Data[floorY+1][floorX];

```

```

24
25     yValUp = (Data[floorY+1][floorX+1]
26              - Data[floorY][floorX+1]) * (newRow - floorY)
27              + Data[floorY][floorX+1];
28
29     Rotated[row+ySide][col+xSide] =
30         (xVal+yVal+xValUp+yValUp) * 0.25;
31 }
32 }

```

Through this function, the captured frame is rotated by an `ang` angle and transformed into a new image with width `2xSide` and height `2ySide`. However the two images are still incomparable due to different physical sizes: Resizing is requested. In Cod. 4.2, the core of the function performing this operation is proposed.

Code 4.2: A section of the function `Resize`, which rescales an image to the DMD dimensions.

```

1  stepX = (double) (width-1)/1024;
2  stepY = (double) (height-1)/768;
3
4  for(row=0; row<768; row++)
5  {
6      newRow = row*stepY;
7      floorY = floor(newRow);
8
9      for(col=0; col<1024; col++)
10     {
11         newCol = column*stepX;
12         floorX = floor(newCol);
13
14         xVal = (Data[floorY][floorX+1]
15                - Data[floorY][floorX]) * (newCol - floorX)
16                + Data[floorY][floorX];
17
18         yVal = (Data[floorY+1][floorX]
19                - Data[floorY][floorX]) * (newRow - floorY)
20                + Data[floorY][floorX];
21
22         xValUp = (Data[floorY+1][floorX+1]
23                  - Data[floorY+1][floorX]) * (newCol - floorX)
24                  + Data[floorY+1][floorX];
25
26         yValUp = (Data[floorY+1][floorX+1]
27                  - Data[floorY][floorX+1]) * (newRow - floorY)
28                  + Data[floorY][floorX+1];
29

```

4. Control program and feedback process

```
30     Resized[row+ySide][col+xSide] =
31         (xVal+yVal+xValUp+yValUp) * 0.25;
32     }
33 }
```

Eventually the "Target Image" and the capture frame – now called "CCD Image" – can be analyzed and compared. Nevertheless it could be worth reminding that the three operations introduce in the final "CCD Image" an unavoidable approximation, as could be noticed reading the codes above: actually they are based on the linear interpolation of the data stored in the image matrices. This will surely limit the feedback efficiency.

III. Errors evaluation The "CCD Image" can be now compared with the "Target Image": an error matrix (called `ErrMtrx`) is produced by the difference between the two data matrices, as shown in Cod. 4.3.

Code 4.3: A section of the function Feedback: errors evaluation. `Max` is a multiplicative factor which rescales each value of the `TargetMtrx`.

```
1  for(row=0; row<768; row++)
2  {
3      for(col=0; col<1024; col++)
4      {
5          [...]
6
7          ErrMtrx[row][col] = CCDMtrx[row][col]
8              - (TargetMtrx[row][col] * max);
9
10         ErrMtrxInt[row][col] = ErrMtrxInt[row][col]
11             + ErrMtrx[row][col];
12
13         [...]
14     }
15 }
```

Instead, in the matrix `ErrMtrxInt`, all the errors calculated pixel by pixel during the different iterations of the feedback process are stored.

IV. Errors application Now the errors have to be applied to the "DMD Matrix": this could be made in different ways and combinations.

Pixel by pixel, all the errors are weighted by the same coefficient `Kp1`. Then each error is subtracted⁴ from the value of the corresponding pixel in

⁴This is a negative feedback process, intended to get the "CCD Image" (signal) closer to the "Target Image" (set-point); therefore the errors have to be subtracted.

the "DMD Matrix". This operation is similar to the proportional correction of a PID, where the gain coefficient is just **Kp1**.

"DMD Easy" makes also possible to apply the third power of the errors to each "DMD Image" matrix value, but with a different weight **Kp3**. This could be helpful when large errors are meant to be corrected faster than the smaller ones.

The algorithm can perform another kind of correction, similar to the integral one of a PID. In order to obtain this effect, the errors evaluated in each feedback iteration are summed and stored in a matrix, **ErrMtrxInt**; then, in every feedback cycle, its elements are summed to each corresponding pixel value of the "DMD Image" data matrix.

In Cod. 4.4, the code lines which carry out the error application are reported.

Code 4.4: A section of the Feedback function: the errors distribution. The third power of the **ErrMtrx[row][col]** is an operation expensive in terms of time, therefore it would be better to avoid its computation if **kp3** were null.

```

1  if(kp3 != 0)
2  {
3      for(row=0; row<768; row++)
4      {
5          for(col=0; col<1024; col++)
6          {
7              DMDMtrx[row][col] = DMDMtrx[row][col]
8                  - kp1 * ErrMtrx[row][col]
9                  - kp3 * pow(ErrMtrx[row][col],3)
10                 - ki1 * ErrMtrxInt[row][col];
11          }
12      }
13  }
14
15  else
16  {
17      for(row=0; row<768; row++)
18      {
19          for(col=0; col<1024; col++)
20          {
21              DMDMtrx[row][col] = DMDMtrx[row][col]
22                  - kp1 * ErrMtrx[row][col]
23                  - ki1 * ErrMtrxInt[row][col];
24          }
25      }
26  }

```

V. Creation of a new image Now that the "DMD Image" has been corrected to be more similar to "Target Image", the square root of each single

4. Control program and feedback process

pixel value can be taken in order to create the reflection coefficient amplitude matrix. Later, the corresponding image can be dithered, loaded into DMD Memory and projected. In case, another feedback step can start.

With the typical experimental image parameters, a feedback step has never required more than 10 s on an Intel Core i7-2670QM based system with 8Gb DDR3 on-board RAM.

This kind of feedback correction of static images projected by the DMD has an advantage: there is no need to know *a priori* the spatial intensity profile of the light incident on the device. This means that measurements of the center and the waist of the laser beam on the DMD screen are in principle not necessary.

4.3 Calibration of the DMD on the CCD

In order to perform the Rotating, Cropping and Resizing operations for executing the feedback, it is necessary to know the exact position of the DMD image on the CCD 1 screen, so an initial calibration of the system has to be done. This is a sensitive procedure which constitutes the second limit to the whole image correction process efficiency. For this reason, a calibration cycle is strongly recommended before each feedback process: actually, lenses, mirrors or the CCD misalignments can easily occur due to mechanical vibrations, introducing a systematic error when the error matrix is estimated.

Initially, a first calibration is carried out automatically by the "Calibration" function implemented in "DMD Easy". The position of DMD image on the CCD screen is characterized by ten parameters: the coordinates of the vertices of the DMD image on the CCD, the rotation angle between the CCD major axis and the longer side of the DMD and the demagnification performed by the optical system between the DMD and the CCD⁵.

The Calibration function performs the following actions

- A squared Flat-top image with 300 pixels per side is projected.
- A single frame is capture by the feedback CCD Camera.
- Cropping, Rotating and Resizing operations are applied to the image.
- The values of the image pixels which fall into the Flat-top plateau are averaged to obtain the mean intensity of the figure.

⁵Image distortions are not expected, that is to say that normal imaging of the DMD active area should be possibly performed. The whole optical set-up has been designed (see Sec. 2.2) in order to satisfy this requirement.

- One at a time, all the parameters previously enumerated are varied in order to maximize this mean intensity, calculated for each parameters variation.

After this first step, the center of the DMD image on the CCD screen – previously found thanks to the vertices coordinates – can be "blocked" and manually adjusted for a fine calibration. This could be done for the rotation angle and the demagnification⁶ as well.

⁶The demagnification starting value should be the second telescope one, 5 in this case.

Chapter 5

Static patterns applications in Atomic Physics

In this chapter, the experimental results concerning the projection of static patterns and their feedback corrections will be presented, but before some quantitative parameters useful for their characterization will be introduced and defined, as well as some considerations on the feedback intrinsic errors will be reported. In the last section presents some considerations about the Talbot effect and its possible applications.

5.1 Characterization parameters

Some parameters have been used in order to quantitatively describe the images captured by the CCDs (see Sec. 2.2). They are following presented.

Root-Mean-Square Error provides information about the difference between the ideal target pattern and the image effectively obtained after its projection. It is expressed mathematically as following

$$\epsilon_{\text{RMS}}[\%] = 100 \sqrt{\frac{1}{IJ} \sum_{(i,j)}^{(I,J)} \left(\frac{P[i,j] - T[i,j]}{C} \right)^2} \quad (5.1)$$

where the index i runs over the I rows and j over the J columns of the data matrices standing for the recorded "P" and the target "T" images. "C" (contrast) is the difference between the lowest and the highest values of the matrix T.

This parameter takes into account only the "local" differences between the two images, without considering the effects on the visual quality produced by the diffraction limit of the experimental set-up (see Sec. 3.4).

Flatness is particularly useful to describe patterns like Flat-tops: it quantifies the average variation of the pattern from its mean value. In analytical terms

$$F.[\%] = 100 \left(1 - \sqrt{\frac{1}{I J} \sum_{(i,j)}^{(I,J)} \left(\frac{P[i, j] - M}{M} \right)^2} \right) \quad (5.2)$$

where

$$M = \sqrt{\frac{\sum_{(i,j)}^{(I,J)} P[i, j]}{I J}} \quad (5.3)$$

In both the equations, the sum is extended only over certain pixels: in the case of Flat-tops, for example, only the pixels which compose the squared central plateau are considered.

Mean-Value-Difference measures quantitatively the deviation of a certain area mean value from the target one. Its formula is reported below

$$\text{MVD}[\%] = 100 \left| \text{IM} - \text{TM} \right| \quad (5.4)$$

where "TM" is the theoretical value which should be assumed by the pixels over which the image mean "IM" is calculated.

Light Utilization is a parameter which characterizes the power conversion. It is defined as the ratio of the incoming beam power to the image beam power.

$$L.U.[\%] = 100 \frac{P_{\text{image}}}{P_{\text{incident}}} \quad (5.5)$$

It can not be higher than 37%, which is the percentage of power in the zero-th diffraction order with respect to the overall incident beam power, having displayed a completely white image on the DMD screen (see Sec. 2.1).

Edge Smoothness In the target images there could be an area of switched-off mirrors just next to a bright zone, nevertheless in the projected images this passage can be not so sudden and well-defined as in the original ones. "Edge smoothness" can be a very useful parameter to estimate how much narrow a real image feature is. It is defined as the number of the DMD pixels corresponding to an intensity jump from 20% to 80% of the maximum in the image recorded by the CCD.

Max-Min contrast This parameter can be used to estimate the contrast between maxima and minima of a lattice pattern. Its formula is

$$C [\%] = 100 \frac{1}{N} \sum_{i=1}^N \frac{\text{Max}_i - \text{Min}_i}{\text{Max}_i} \quad (5.6)$$

where N is the number of the maximum-minimum couples taken into account.

Feedback Errors During a feedback loop, the Cropping, Rotating and Resizing operations (described in details in Sec. 4.2) and the dithering algorithm introduce some uncertainties in the evaluation of the errors that will be assigned to each image pixel¹. This problem causes an uncertainty on the Root-Mean-Square Error value, which can be estimated by operating a feedback correction on different patterns without effectively assigning any error to the image pixels, i. e. zeroing the proportional and integral gains. In this case, if the operations of image adjustment were ideal, the ϵ_{RMS} should be constant over all the iterations, instead a fluctuation of that parameter can be noticed. The mean value of these fluctuations, obtained by measurements carried out for several kinds of patterns, is 0.6%. This value is assumed as the error affecting the ϵ_{RMS} estimated during the feedback process.

¹For further details and an experimental manifestation of this problem, see Sec. 5.2.

5.2 Flat-tops

The first pattern taken into account is the Flat-top. As anticipated in Sec. 3.2, it is an uniform white square surrounded by completely black space (image a) in Fig. 5.2). Flat-top is the ideal pattern to be projected with the DMD in order to obtain a laser beam with a flat intensity profile.

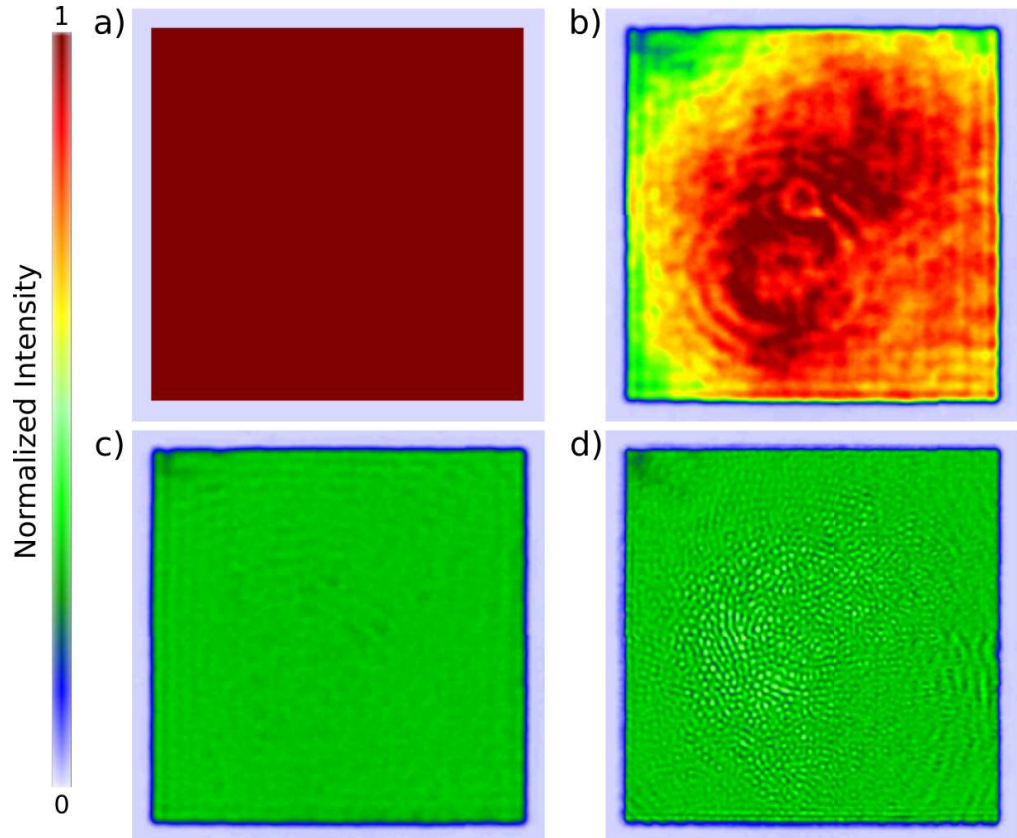


Figure 5.1: Flat-top images. a) The ideal Flat-top, having 400 pixels per side, centred in the DMD screen. b) An image, recorded by the CCD 1, of the Flat-top without any correction. It will be the starting point for the feedback process. c) Flat-top after 10 iterations of the feedback process. A spatial filter has been applied to the beam before the CCD. d) Flat-top after 10 iterations of the feedback process. The iris of the spatial filter is wide open, so any filter is applied. Only the central (500×500) region of the images has been reported.

Due to the original gaussian profile of the beam incident on the DMD, it is necessary to perform a feedback in order to flatten the central part of the figure and eliminate the top of the gaussian (image b) in Fig. 5.2). With this expedient, joined to a spatial filtering (described in Sec. 2.3), a satisfying result can be achieved.

Feedback processes have been applied on the Flat-top image with and

without spatial filtering (performed during the feedback). Images c) and d) in Fig. 5.1 show the results obtained after 10 feedback iterations. The corresponding Root-Mean-Square error trends, estimated via Eq. 5.1, are reported in Fig. 5.2.

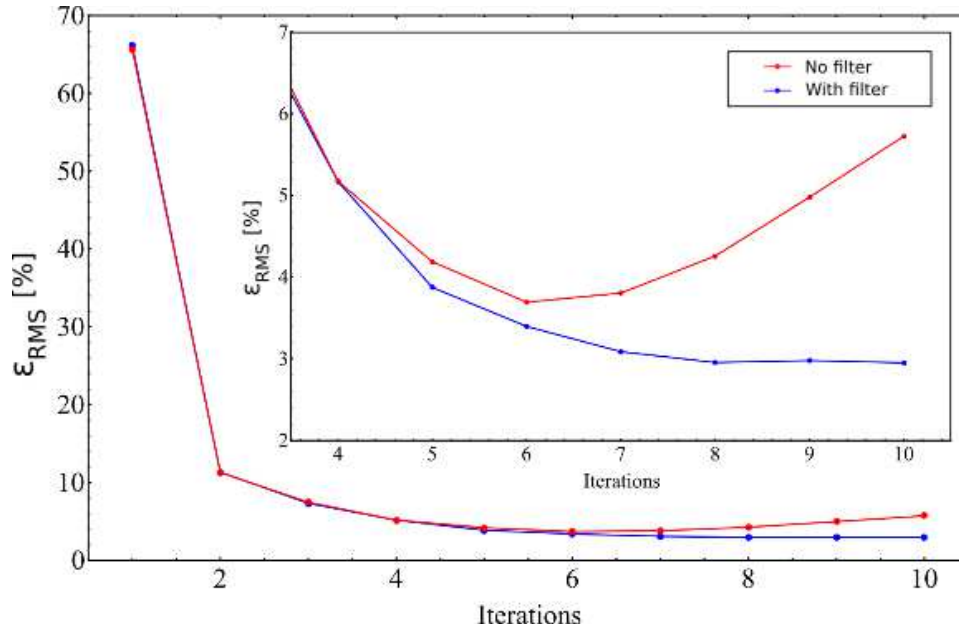


Figure 5.2: Flat-top Root-Mean-Square errors calculated for the Flat-top corrected by the feedback without any spatial filter applied (red track) and with a spatial filter performed by an iris with diameter 3.5 mm (blue track).

As can be seen, the red track in Fig. 5.2 shows a minimum at about 3.7% in the sixth iteration: in the following iterations, the images keep getting worse. The blue one, instead, settles down at less than 3% after a sudden error decreasing. The reason of those different trends lies in the intrinsic systematic errors of the dithering algorithm together with the Cropping, Rotate and Resizing operations. In order to correct the small features affecting the original image, the feedback arranges and assigns similar errors to localized areas (groups of few pixels), whose positions on the image can not be exactly preserved during the graphical elaborations carried out by the adaptive operations and the dithering procedure. In this way, it could happen that the errors introduced by the feedback and weighted by the gain factors (see Sec. 4.2) are added to the wrong pixels values, creating a sort of positive feedback, which works against the image quality improvement. This phenomenon can be noticed in image d) in Fig. 5.1 as the appearance of series of brighter small dots². During an iteration, the intensity of one

²This event, affecting the overall Root-Mean-Square Error, can not be attributed to a bad calibration because it concerns only a part of the image.

of those dots should be lowered by the feedback mechanism, so a negative error is assigned to those pixels. However it can be shifted by the graphical elaboration and hence influence the dark area near the dot, making it even darker, as in a positive feedback correction³. Nevertheless, spatial filtering (see Sec. 2.3) can be used in order to get rid of this highly localized contribution, formed by high frequencies in the Fourier space. Actually, image c) in Fig. 5.1 does not suffer of this problem, therefore the Root-Mean-Square error is lower for the filtered image (blue track in Fig. 5.2).

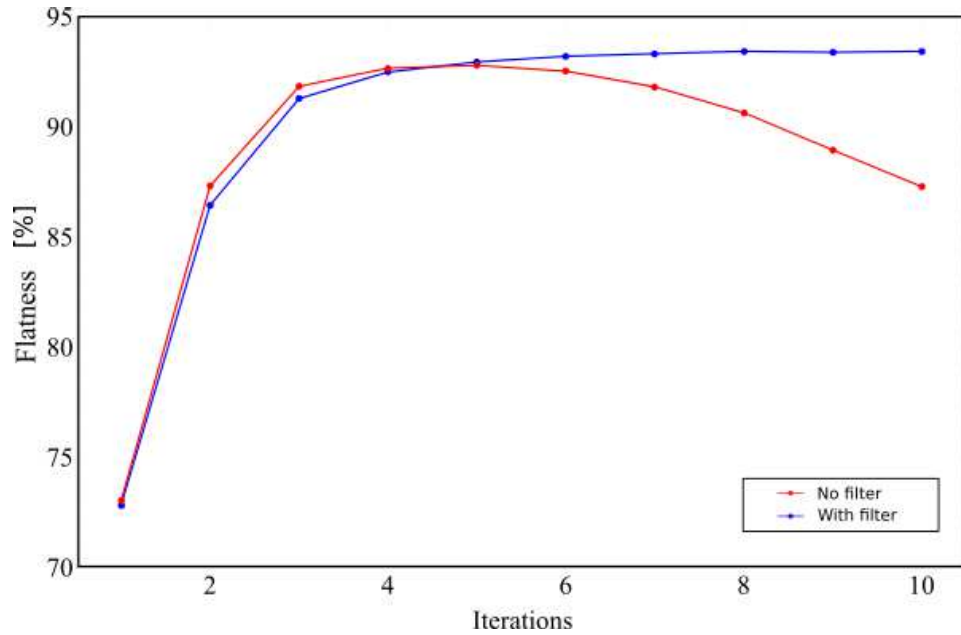


Figure 5.3: Flat-top Flatness. The data are calculated for the Flat-top corrected by the feedback (10 iterations) without any spatial filter applied (red track) and with a spatial filter performed by an iris with diameter 3.5 mm (blue track).

Figs. 5.3 and 5.4 show the Flatness and the Mean-Value-Difference (MVD) graphs as a function of the feedback iterations number, respectively. They are calculated via Eq. 5.2 and Eq. 5.4. These two parameters separate the contributions which form the Root-Mean-Square error: the MVD represents the average variance from the image mean value, so it can reveal the presence of localized peaks on the flat plateau; whereas the Flatness expresses the variance between the image mean and the target value, in other words the "DC" error of the feedback loop. In the two graphs proposed, it can be noticed that the MVD errors have the same trend, while the red track in the Flatness graph gets worse with the increasing iterations number. This means that the problem highlighted before does not affect the achievement of the

³For these reasons, it is strongly recommended to keep low the feedback iterations number.

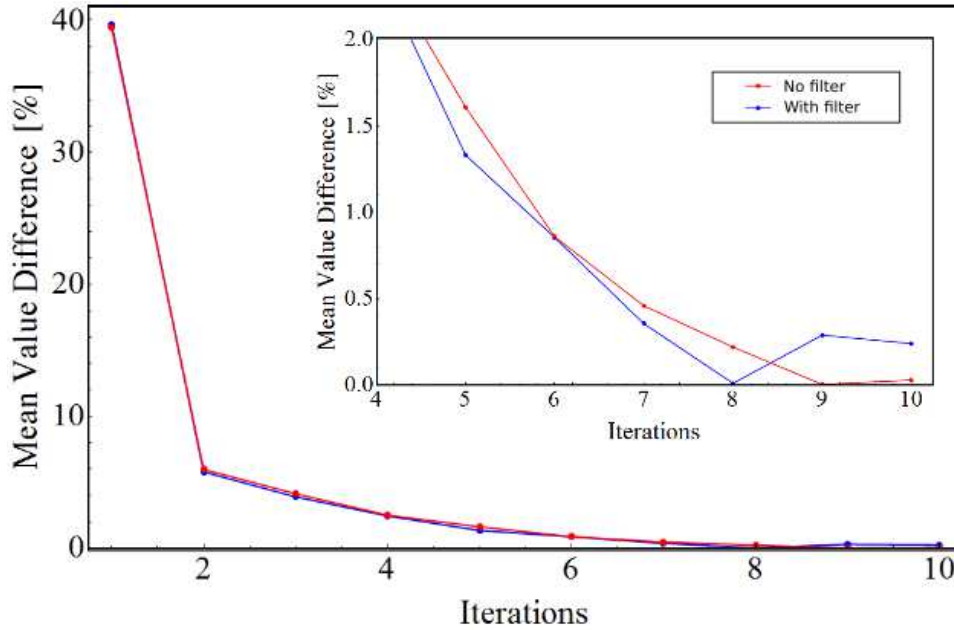


Figure 5.4: Flat-top Mean-Value-Difference. The data are calculated for the Flat-top corrected by the feedback (10 iterations) without any spatial filter applied (red track) and with a spatial filter performed by an iris with diameter 3.5 mm (blue track).

target values as much as it influences the Flat-top flatness through several narrow peaks on the plateau.

In Fig. 5.5 some Flat-top profiles are reported for increasing iterations number. Comparing the first iteration profiles of the two graphs (red higher tracks), the action of the spatial filter can be noticed: even if a common trend can be recognized in both of them, the filtered one is smoother than the other due to the absence of the higher spatial frequencies. With the iteration number increasing, the overall profiles get closer to the target one – as shown by the MVD graph reported in Fig. 5.4 –, but at the same time problems due to the adaptive operations and dithering arise in no-filtered profiles as narrow peaks which have negative consequences on the Root-Mean-Square Error and the Flatness.

In Fig. 5.5 another feature can be inferred, better figured out in Fig. 5.6: actually the spatial filter has negative effects on the structures edge sharpness, as can be noticed in the lower part of the filtered profiles in Fig. 5.5. With the iris diameter decreasing, always lower frequencies are blocked by the spatial filter, therefore particularly narrow or defined structures – as the sides or the vertices of the Flat-tops – are formed with increasing number of micromirrors

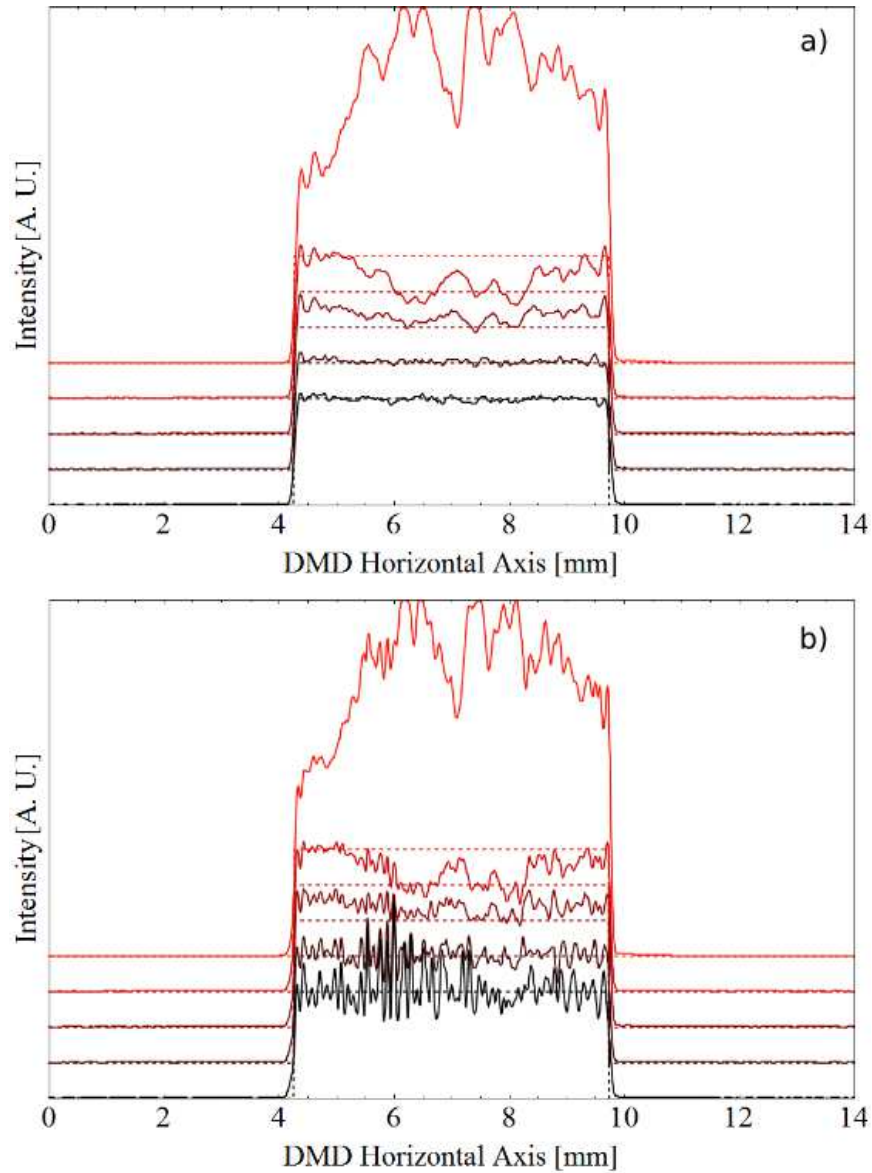


Figure 5.5: Some spatial profiles of a Flat-top with 400 pixels per side are presented. The dashed lines correspond to the target values which have to be reached. Each pair formed by the profile and its own target value is plotted in the same color. Offsets have been added for a better reading of the graphs. In both graphs, the profiles are relative (from the top) to first, second, third, seventh and tenth feedback iteration. The graph a) reports profiles taken from images recorded during a feedback process with the spatial filter iris set to a diameter of 3.5 mm. The graph b) shows profiles taken from images recorded during a feedback process with no spatial filter performed.

(as reported in Fig. 5.6).

To summarize, two different procedures have been adopted for creating a Flat-top. The one which uses the spatial filter exhibits better results in terms of Root-Mean-Square error, Flatness and Mean-Value-Difference.

In order to obtain better images with the other method, the spatial filtering can be applied *after* the feedback process. Different iris diameters have been tested: the Smoothness and the Flatness trends are plotted in Fig. 5.6 as a function of the iris diameter in order to establish the best trade-off between these two parameters. The optimal diameter turns out to be slightly smaller than 2 mm.

Regarding the Light Utilization, the measured DMD optical efficiency is $\eta = 37\%$ for the specific incident beam used in this work, as reported in Sec. 2.1. The Flat-Tops created use only 400^2 pixels of the device, so the *L.U.* expected is

$$L.U. = 0.37 \frac{400^2}{1024\ 768} = 7.5\% \quad (5.7)$$

The L.U. measured for the both Flat-Tops corrected by the feedback process is about 7.2%.

Another method to achieve a Flat-top, presented in details in Etzold, 2010 [22], consists in the calculation of the pattern to be displayed on the DMD, taking into account the gaussian shape of the incoming laser beam and correcting the desired intensity profile according to following relation

$$R[x, y] = \sqrt{\frac{T[x, y]}{G[x, y]}} \quad (5.8)$$

where " $T[x, y]$ " is the ideal intensity pattern, " $G[x, y]$ " is the theoretical incident beam profile – which has the analytical form reported in Eq. 4.1 – and " $R[x, y]$ " is the amplitude reflection coefficient.

This method has the advantage that does not require a feedback process to get rid of the initial light source intensity profile. On the other hand, the parameters of the incoming beam need to be carefully determined and possible defects in the projection optical system, like diffraction of the multiple optical elements and dust, are not considered. For this reason, it is usually necessary to employ a feedback process in order to achieve the best fidelity of the final images to the ideal ones.

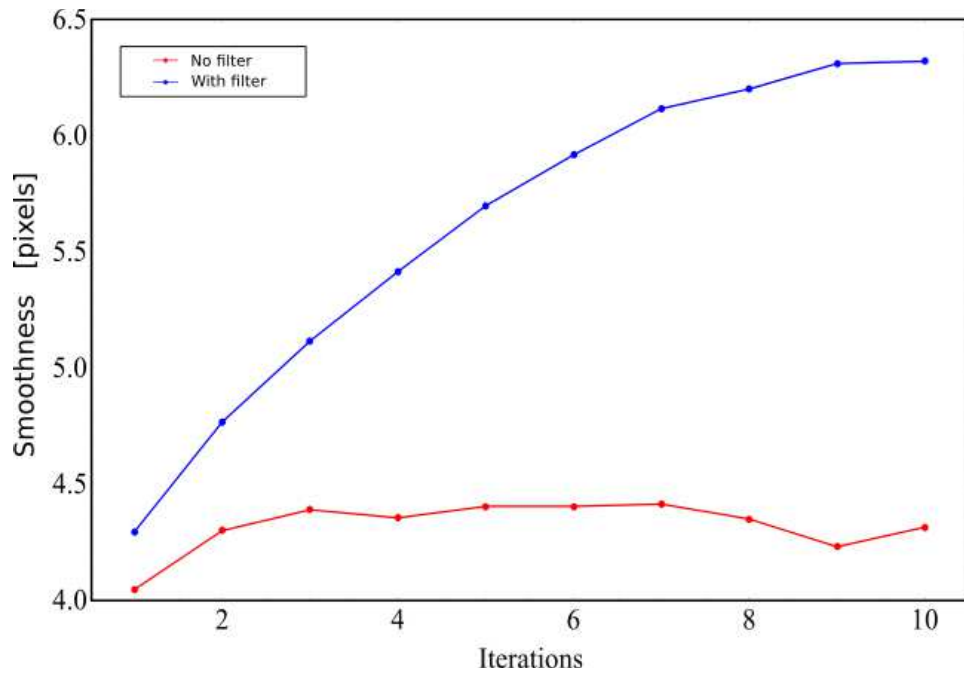


Figure 5.6: Flat-top Smoothness. In red, the Smoothness values for unfiltered images. In blue, the Smoothness values for filtered images. The diameter of the spatial filter iris is 3.5 mm. On the vertical axis the Smoothness mean value (calculated with 200 Smoothness values evaluated on the same image) is reported.

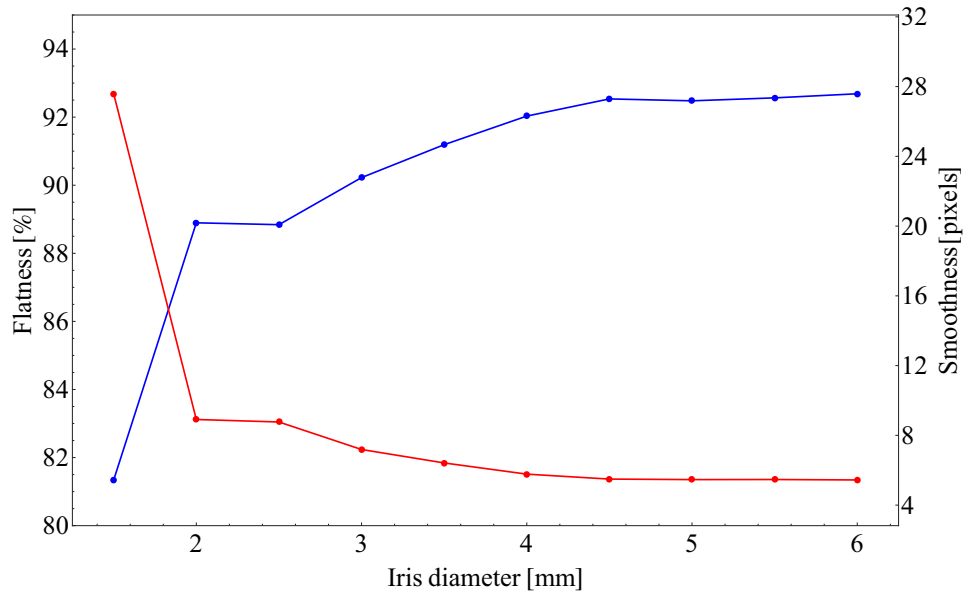


Figure 5.7: Trade-off between Smoothness (in red) and Flatness (in blue) as a function of the iris diameter.

5.3 Lattices

The second pattern taken into account is the "lattice" (see Sec. 3.3). In order to correct the projected images, two different methods have been implemented

- "*Lattice*". It consists in projecting the lattice and correcting it directly through the feedback.
- "*Top-Lattice*". It consists in creating a Flat-top with the DMD, operating a feedback on it and then superimposing the ideal lattice pattern on the flat plateau.

The theoretical calculations reported in Sec. 2.5 show that, in order to achieve a lattice having 30×30 sites, a depth of $s = 30$ and a lattice spacing of $1 \mu\text{m}$ after the projection system⁴ described in the same section, an ideal beam waist of 7.2 mm would be necessary. Anyway, due to the non-optimal illumination condition of the DMD screen by the laser beam – which has a waist that is smaller than the ideal dimension found –, a lattice with the same number of pixels per site (18 pixels) but a different sites number (22 sites per side) has been achieved and characterized. Actually, for the analysis purposes, it is important to maintain the pixels needed to create a single site rather than the overall number of lattice sites. In general, the number of pixels (or, equivalently, micromirrors) per one site side (MPS) is a parameter to be chosen carefully. The higher the MPS, the better the site profile can be achieved: actually, with few micromirrors, the ideal site profile could not be imitated smoothly and accurately because of the discrete nature of the projection system. At the same time, a high MPS would restrict the lattice extension and require a more powerful demagnification system in order to obtain, in the objective image plane, an acceptable lattice pitch for atomic physics applications. Therefore a trade-off has to be reached on the basis of the experimental set-up and the aims of the pattern to be projected.

In Fig. 5.8 the Root-Mean-Square errors as a function of the pixels number are reported. Each experimental point has been evaluated averaging the ϵ_{RMS} of the last four images (over a total number of ten) produced by the feedback process applied on each single lattice. Thus, with 18 pixels per site, an error of about 2% has to be expected.

5.3.1 Lattice

In this section, the experimental results of the "Lattice" projection technique are reported. The pattern has been achieved performing the feedback

⁴This system is basically formed by a telescope 1 : 3 (spatial filtering one) coupled with an objective 80X, which will be soon implemented in the general experimental set-up. Its demagnification is 240.

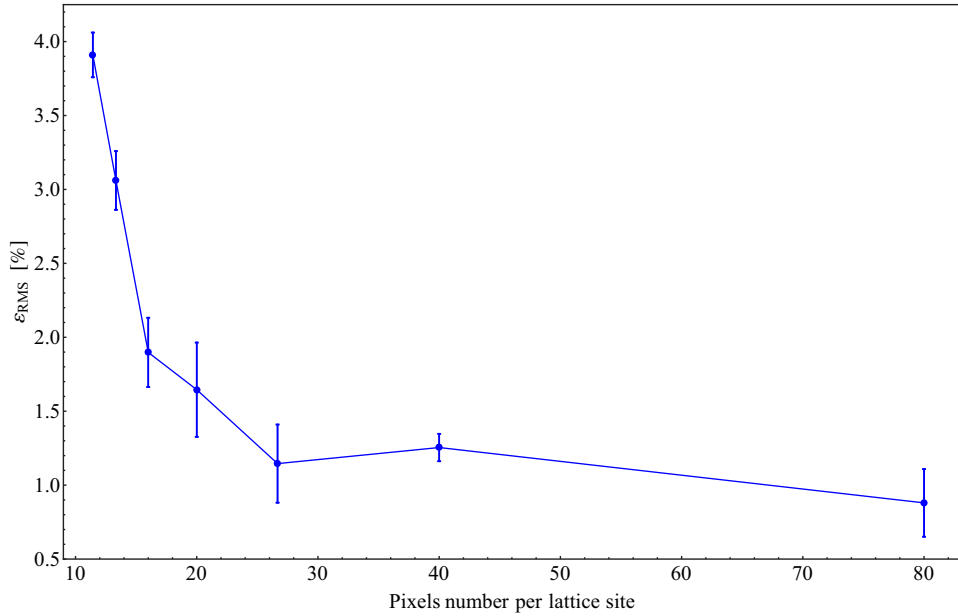


Figure 5.8: Lattice Root-Mean-Square errors as a function of the pixels number per lattice site.

process directly on the ideal lattice image projected by the DMD, as in the case of the Flat-top. In Fig. 5.9 the Root-Mean-Square errors as a function of the iterations number are plotted. The pattern error is $\epsilon_{\text{RMS}} = 1.9\%$. It is evaluated by averaging the image errors of the last four feedback iterations.

In Fig. 5.10, the lattice profile image of the tenth feedback iteration is reported, while in Fig. 5.11 a lattice profile cut along a line of the tenth feedback iteration is plotted. The line represented is parallel to the long side of the DMD and corresponds to a "maxima line", i. e. a maxima series of the lattice lies on it.

In Fig. 5.12, a profile of the lattice integrated along the vertical side is proposed. As can be noticed, the trend is quite smooth and regular in both graphs. The contrast between the local maxima and the adjacent minima of that profile has been averaged in order to obtain a quantitative parameter describing the lattice depth. The value found is $(52 \pm 5)\%$.

The Light Utilization for this pattern is 5.2%. It is expected to be smaller than the Flat-top one (7.5%) because of the lower number of micromirrors switched on.

All of the measurements reported above have been made with the wide-open iris, therefore without operating any spatial filtering. In Fig. 5.13 the

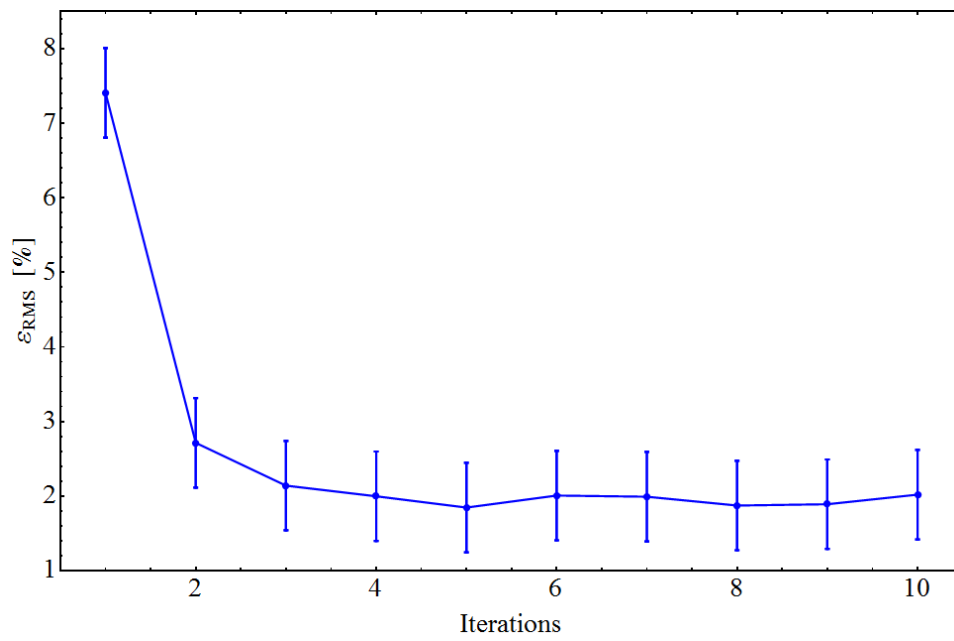


Figure 5.9: Lattice Root-Mean-Square errors as a function of the iterations number.

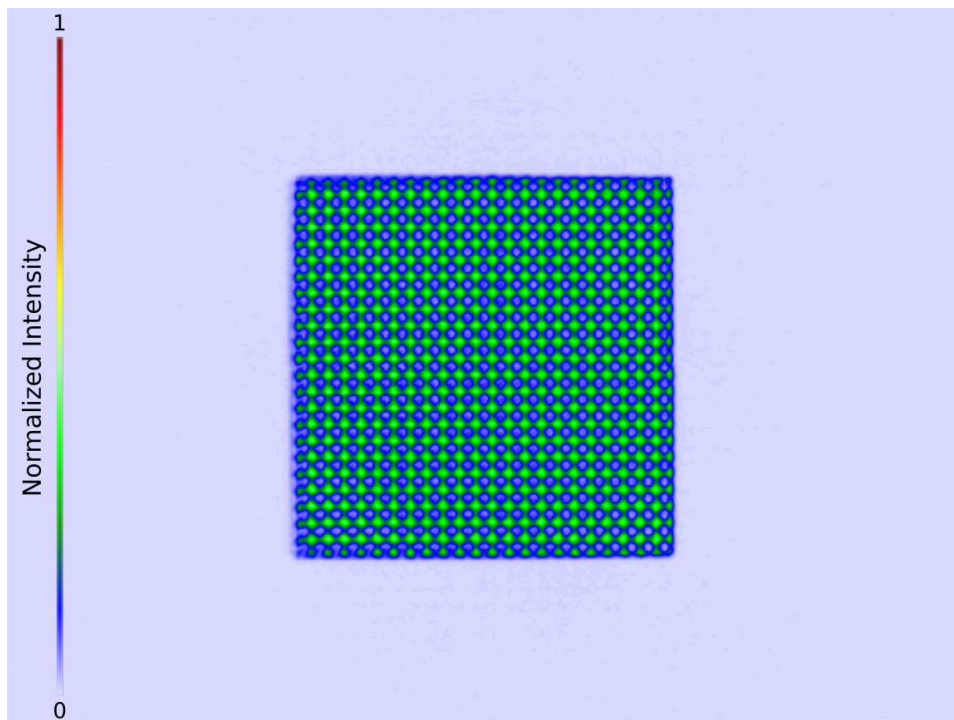


Figure 5.10: Lattice intensity profile corrected at the tenth feedback iteration.

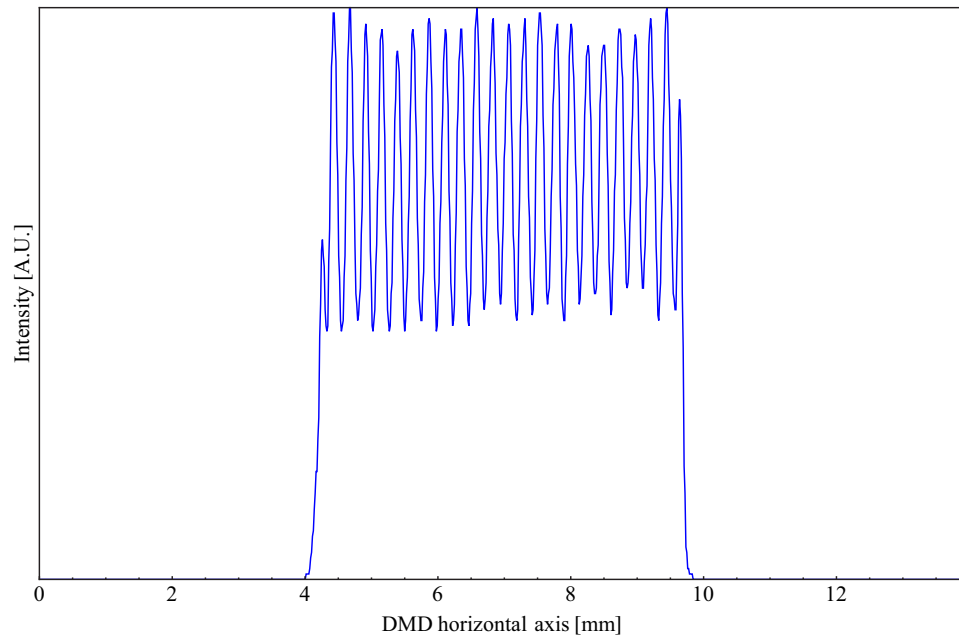


Figure 5.11: Lattice profile, taken along a maxima line.

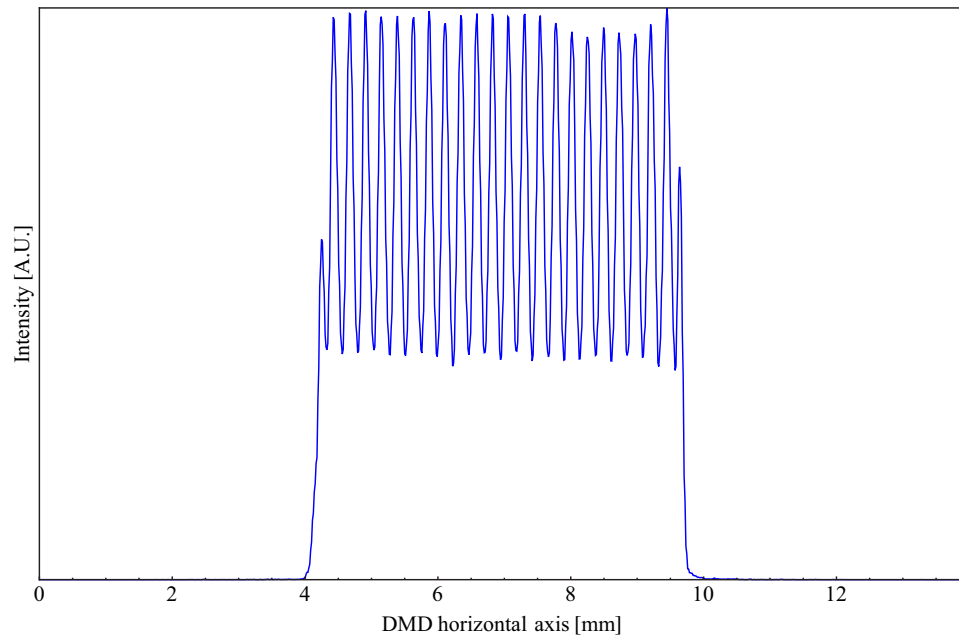


Figure 5.12: Integrated lattice profile.

experimental trend of the Root-Mean-Square errors is reported as a function of the iris diameter.

As can be noticed, ε_{RMS} increases with the decreasing iris diameter.

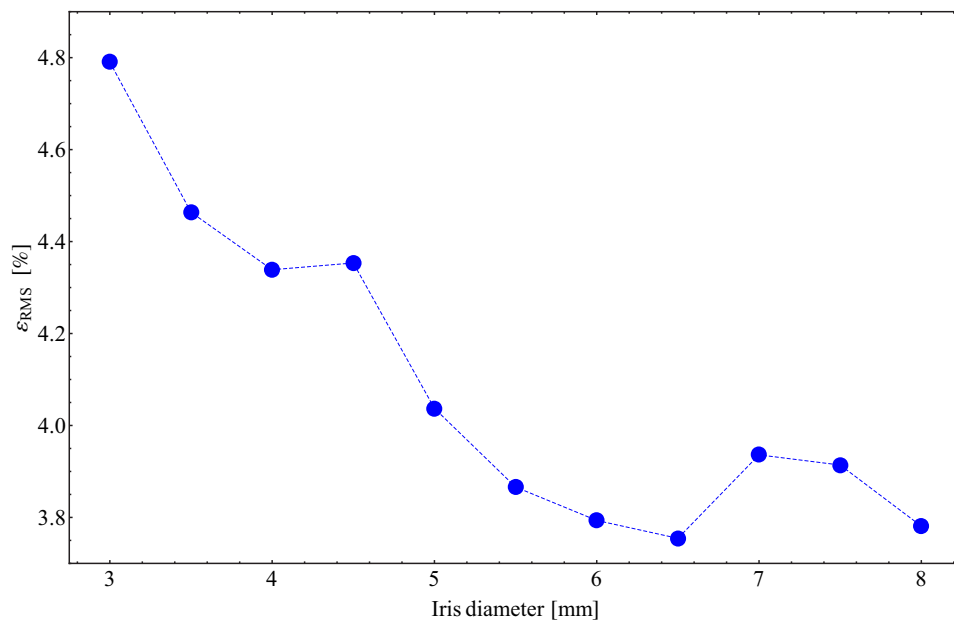


Figure 5.13: Lattice Root-Mean-Square errors as a function of the iris diameter.

Hence, it is not possible to exploit a full filtering (with iris diameter smaller than 6 mm) without hampering the lattice structure itself.

5.3.2 Top-Lattice

In order to obtain an optical lattice corrected for the gaussian beam shape and other defects, another method has been implemented. It consists in creating a Flat-top and then superimposing the target lattice on its corrected plateau without any further feedback. Regarding the details about the application of the feedback process on a Flat-top, see the Sec. 5.2.

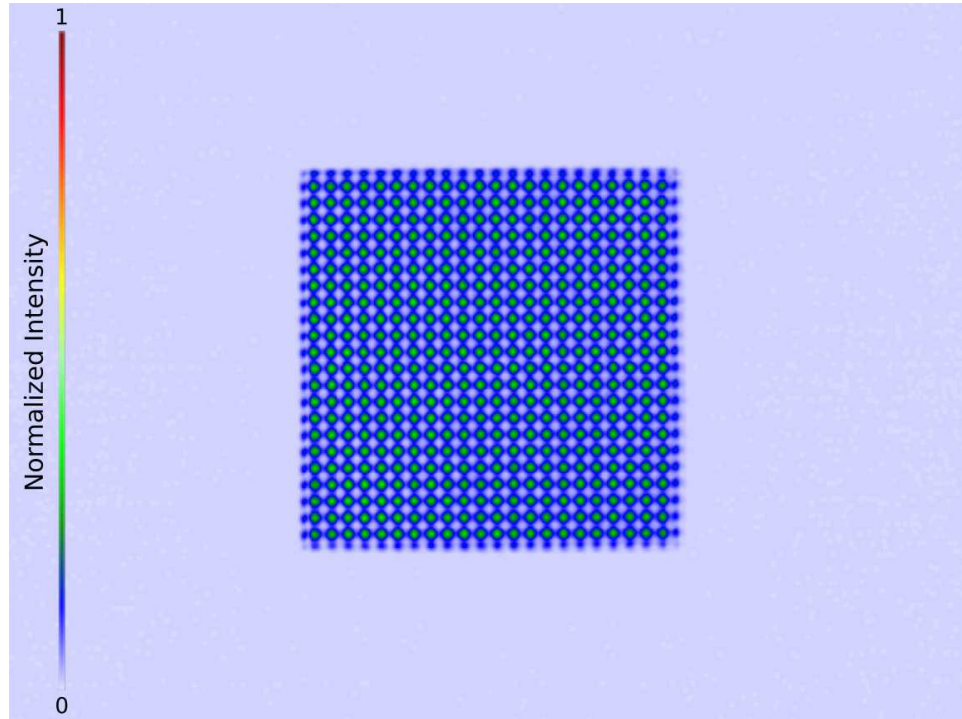


Figure 5.14: Top-Lattice intensity profile.

A squared Flat-top with 400 pixels per side, centred in the DMD Active Area, has been projected and corrected via feedback. Then a lattice with 22 sites per side and 18 MPS has been superimposed on it. This operation can be performed by a function of "DMD Easy", which is able to return the product of the values contained in two different image data matrices, with the same sizes, pixel by pixel. If the two starting matrices are normalized between 0 and 1, the resulting matrix will be normalized too. Therefore, the resulting matrix represents a gray-scale image standing for the superimposition of the two initial ones.

In Fig. 5.14, the intensity profile of the Top-Lattice is proposed, whereas in Figs. 5.15 and 5.16 its profile cut along a maxima line and the integrated profile of the pattern along the short side are respectively reported. As can be inferred from the last two graphs, the Max-Min contrast is greater

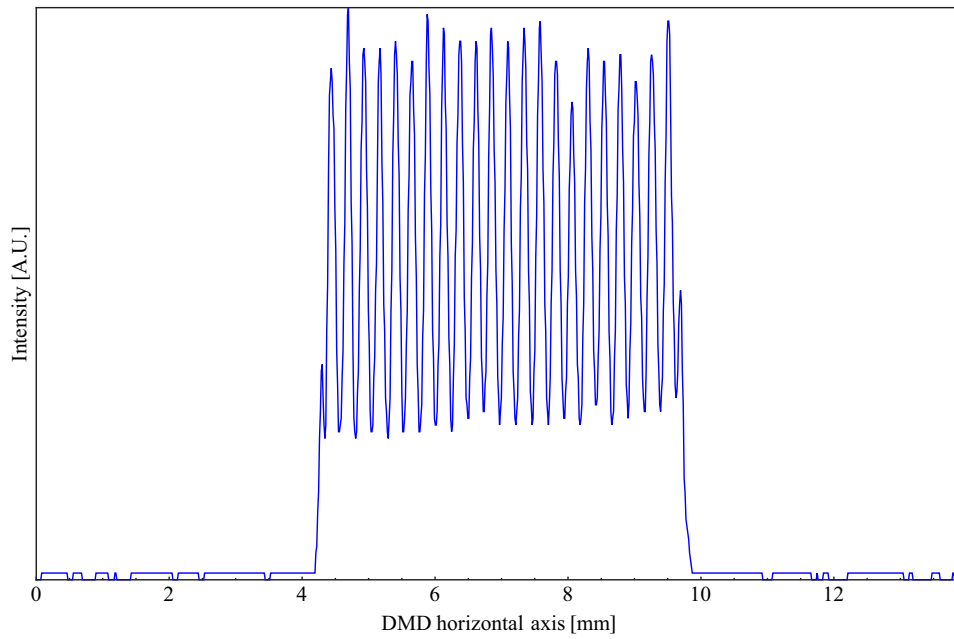


Figure 5.15: Top-Lattice profile taken along a maxima line.

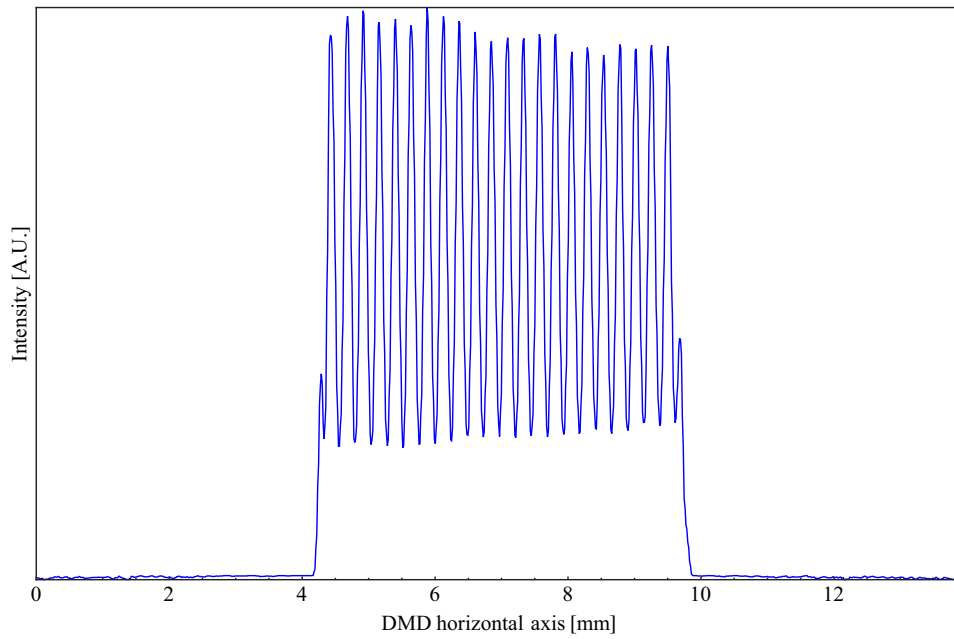


Figure 5.16: Integrated Top-Lattice profile.

than the contrast of the lattice created with the other method. It is calculated as $(71 \pm 3)\%$. This feature allows, for the same incoming laser power, for the generation of a deeper optical lattice with respect to the one created by the

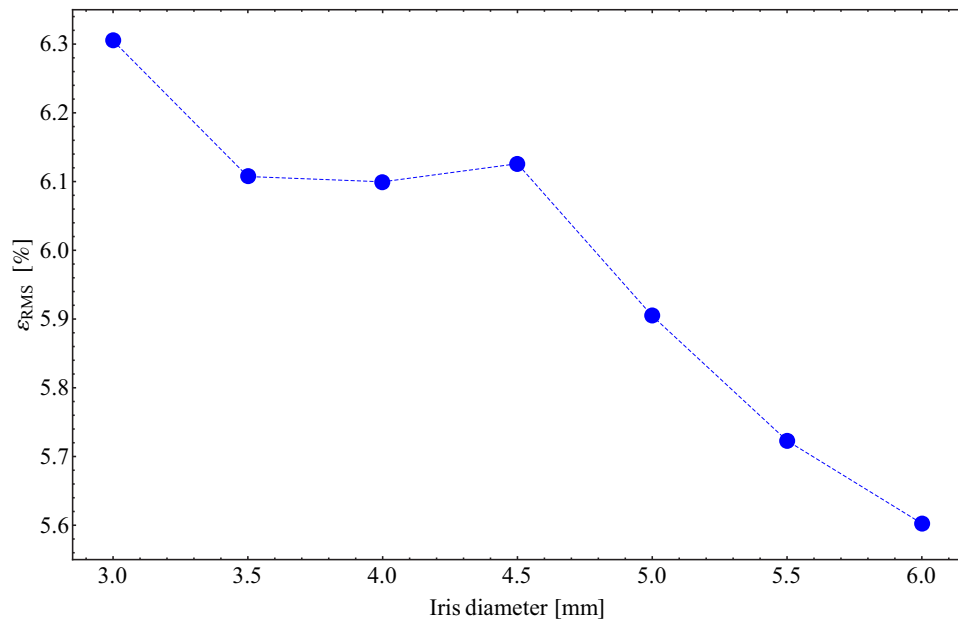


Figure 5.17: Top-Lattice Root-Mean-Square errors as a function of the iris diameter.

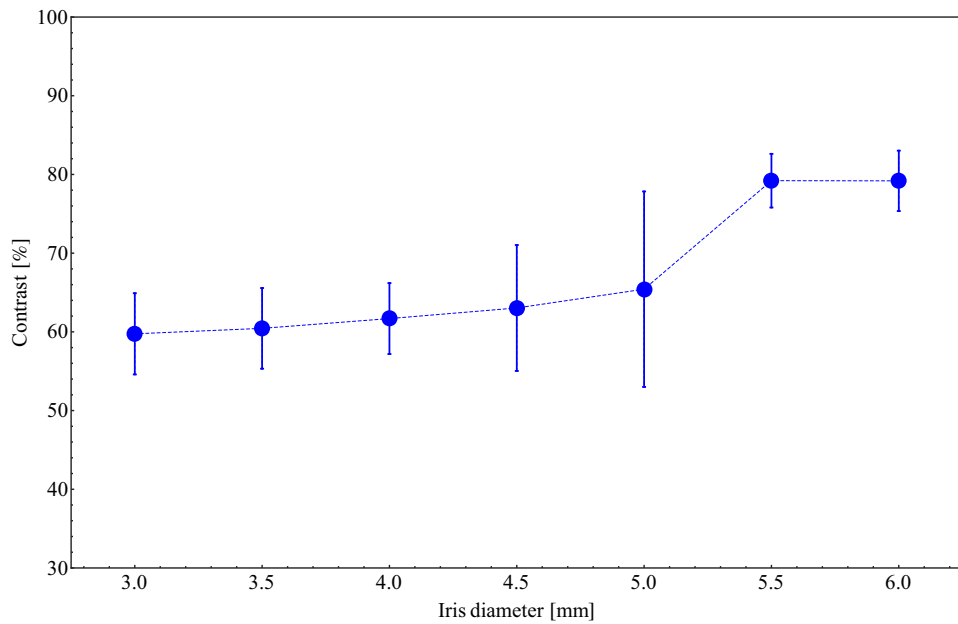


Figure 5.18: Top-Lattice contrasts as a function of the iris diameter.

method previously explained.

Regarding the Light Utilization, for this pattern it is equal to 3.4%.

In this case, there is not a Top-Lattice target image as reference for the

feedback process, so the Root-Mean-Square error can not be easily evaluated for the final image obtained through this method. This parameter has been established by comparing the resulting lattice image with the same lattice pattern (having the same dimensions and MPS) multiplied by a factor (MAX) and minimizing the ϵ_{RMS} errors calculated by varying MAX. The result obtained is 2%.

Regarding the spatial filtering, Fig. 5.17 shows the ϵ_{RMS} – concerning the comparison between the lattice images captured by the CCD and the lattice ideal pattern – as a function of the iris diameter. Instead, in Fig. 5.18, the contrast is plotted as a function of the iris diameter.

5.4 Other patterns

Several different patterns which can be implemented in atomic physics experiments are presented in this section.

- The **Ring**, Figs. 5.19 and 5.20. It is a pattern formed by an uniform empty circle. For example, it can be used to select only a circular portion of the cooled atoms already trapped in a standard optical lattice.
- The **Wire**, Figs. 5.21 and 5.22. This pattern is formed by two Flat-tops with the same gray level linked together by a narrow rectangular structure having a different gray level. If this pattern is created by a laser red-detuned with respect to the atomic transition exploited to trap the atoms, the conditions to study tunneling processes could be simulated, for example. (Krinner et al., 1999 [48]).
- The **Line**, Figs. 5.23 and 5.24. It is a very narrow linear pattern with an uniform gray level. If created by a blue-detuned laser light, it could be used in order to separate the ultra-cold atomic cloud into two different parts, while in case of red-detuning, it creates lines among atoms. A possible application could be the realization of a single particle trapped in a box-like potential. First, the DMD is used to address a single line in a Mott insulator and remove all the other atoms. Afterwards, the lattice perpendicular to the addressed line is ramped up to create one-dimensional tubes containing only one atom. In the end, a box shaped potentials (e. g. a Flat-top) is projected onto this structure. Through this procedure, the atoms are then confined to one dimension with boundaries. Along this dimension the lattice can be ramped down too, allowing the atoms to tunnel along its own tube [7].

Tab. 5.1 resumes the ϵ_{RMS} errors and the Light Utilizations of the patterns presented in this chapter.

| Pattern | ϵ_{RMS} | L.U. |
|-------------|-------------------------|-------|
| Flat-top | 3 % | 7.2 % |
| Lattice | 1.9 % | 5.2 % |
| Top-Lattice | 2 % | 3.4 % |
| Ring | 2.4 % | 4 % |
| Wire | 1.8 % | 4.8 % |
| Line | 1.9 % | 0.4 % |

Table 5.1: Static Patterns Root-Mean-Square Errors and Light Utilization.

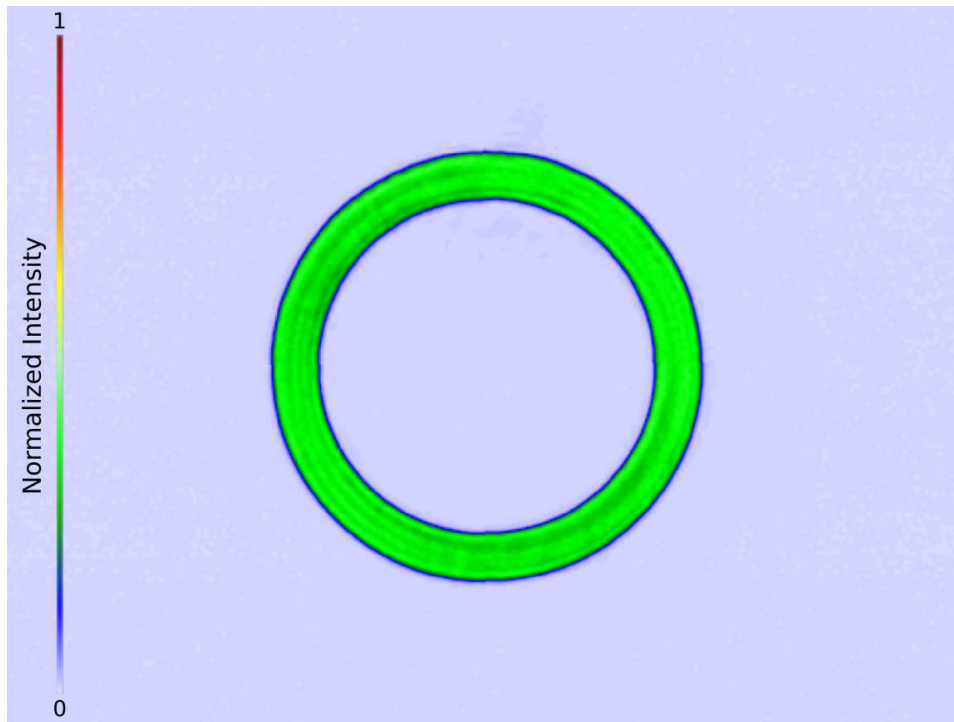


Figure 5.19: Circle intensity profile.

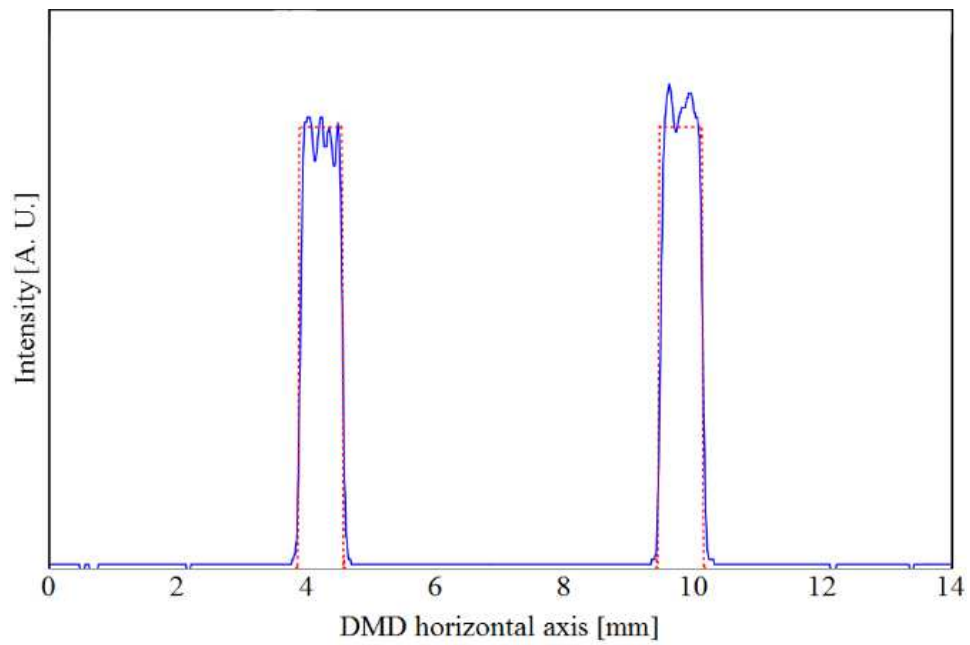


Figure 5.20: Circle profile cut along the diameter parallel to the DMD long side.

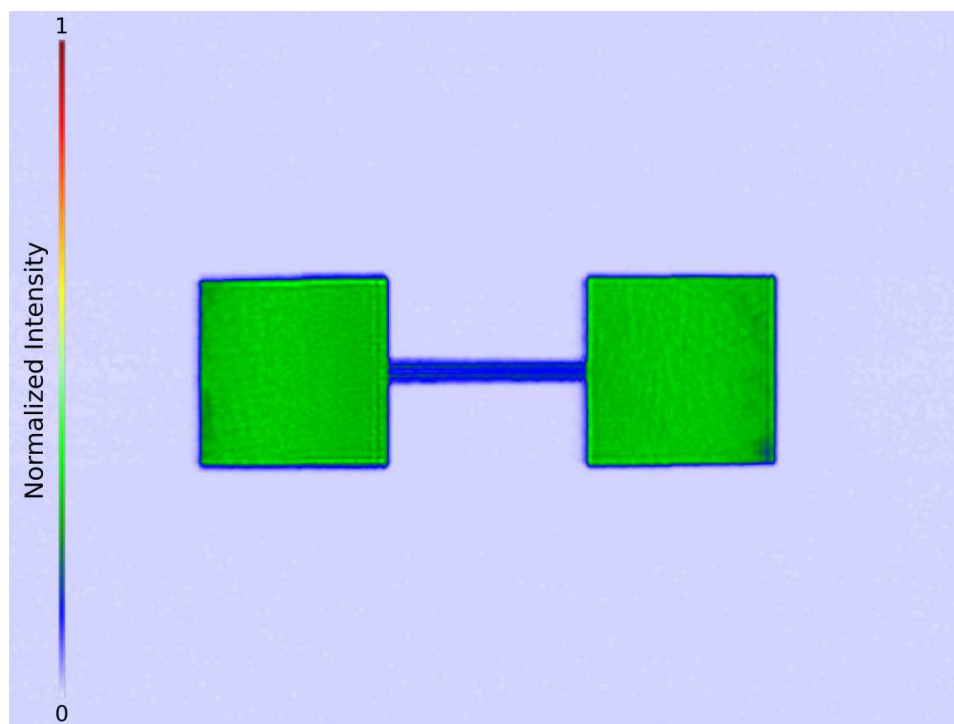


Figure 5.21: Wire intensity profile.

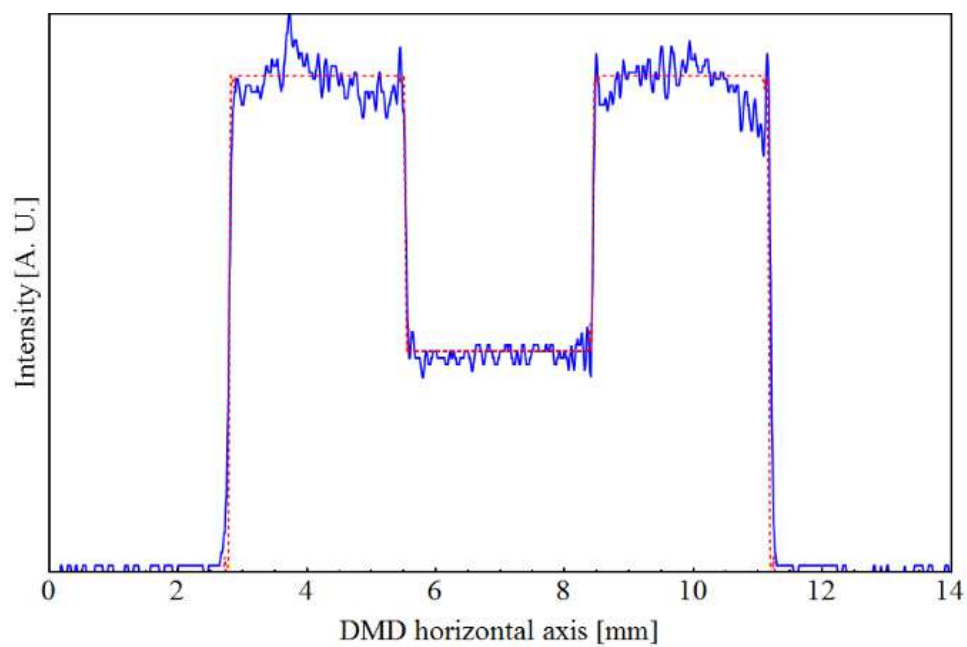


Figure 5.22: Wire profile.

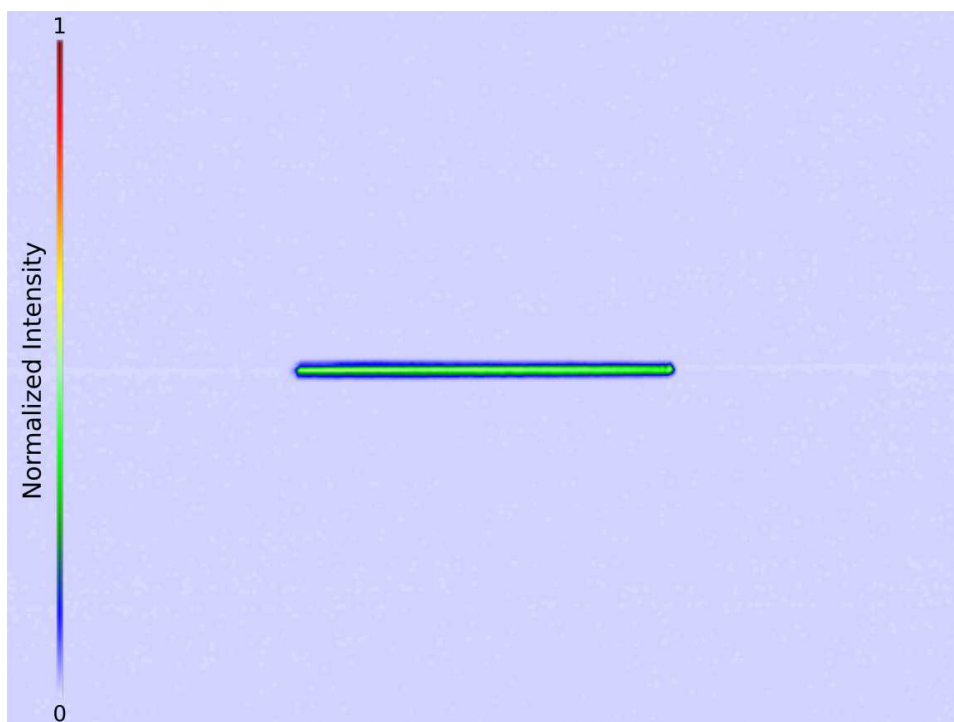


Figure 5.23: Line intensity profile.

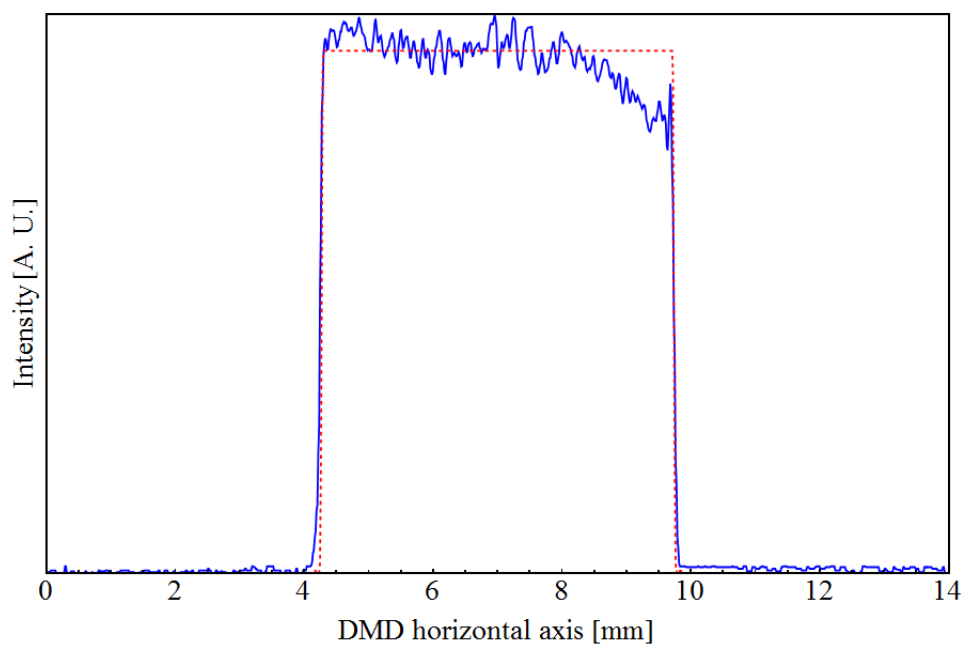


Figure 5.24: Line profile.

5.5 Observation of the Talbot effect

Periodical patterns form an important category of images to be projected by a DMD due to their possibility of creating regular arrangements of potentials which, anyway, are able to trap ultra-cold atoms only in a plane transversal with respect to the modulated laser beam axis. By manipulating the intensity profile of coherent light in periodical shapes, the so-called Talbot effect could arise. It can be exploited in order to create trap potentials able to confine atoms along the laser beam axis as well, without using additional optical lattices or further trapping forces.

The Talbot effect consists in the self-imaging of periodical structures due to near-field diffraction [12]. When a plane-parallel light beam impinging on a transmission diffraction grating, its image is repeated at regular distances away from the grating plane (placed in $L_T = 0$ in Fig. 5.25). This regular distance is called "Talbot length", L_T . At a distance from the grating plane equal to half the Talbot length, a self-image occurs with a phase-shifting of half a grating pitch, while at one quarter and at three quarters of the Talbot length, the self-image is halved in size and appears with half the period of the grating. The so-called "Talbot carpet", that is the spatial evolution of the laser beams which form the images of the periodical diffraction object, is shown in Fig. 5.25.

The theory of the optical Talbot effect was first developed by Rayleigh in the diffraction theory framework in the near-field approximation (Fresnel diffraction). He found the following expression for the Talbot length

$$L_T = \frac{\lambda}{1 - \sqrt{1 - (\lambda/a)^2}} \quad (5.9)$$

where a is the grooves pitch of the diffraction grating and λ is the wavelength of the incident light.

In principle, a collection of gaussian laser beams travelling along the same direction and with their axes arranged in a periodical pattern, provides the requirements for the Talbot effect arising. Thus a diffraction grating can be simulated by a Digital Micromirror Device by displaying on its screen a periodical pattern as a lattice in one-dimension (Eq. 6.12 in Sec. 6.1) or in two-dimensions (Eq. 3.2 in Sec. 3.3).

For a fixed laser wavelength (in this case, the laser used for this experiment has a wavelength of 578 nm), the Talbot length depends only on the lattice spacing. A 2-D lattice with 40 MPP (a pitch equal to 547.2 μm on the DMD screen) has been displayed on the DMD in order to observe the Talbot effect. With the optical system implemented during this work (overall demagnification of 100 and diffraction limit equal to 92.5 μm , see Sec. 2.4),

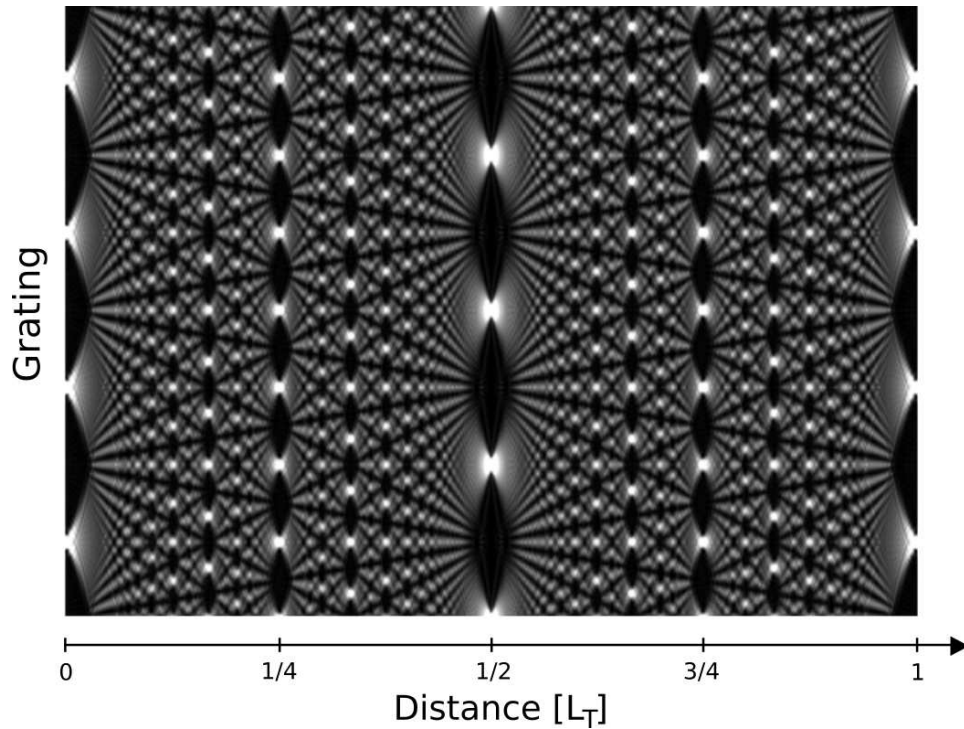


Figure 5.25: Example of Talbot carpet. The distance is expressed in terms of Talbot length L_T .

this pattern can be created on the image plane of the first objective with a pitch of $54.7 \mu\text{m}$, so the associated Talbot length is about $L_T = 103 \mu\text{m}$. The Talbot carpet can be imaged through the second microscope system. Focusing the image plane, the lattice displayed on the DMD should be seen, then by varying the second objective focus position, the patterns which form the carpet should be observed. The Talbot effect imaging requires that the depth of focus of the second objective is smaller than L_T so that the different images of the carpet could be distinguished.

Fig. 5.26 shows several Talbot carpet images captured by the CCD 2. The frames a) and e) refer to a distance d from the first objective image plane equal to $d = 0$ and $d = L_T$, respectively, so they report the same image: actually, after a distance equal to the Talbot length, the same pattern is formed again. At intermediate distances, other carpet points are sampled: for example, in the frame c) the lattice pattern is recorded with a phase-shift of half the lattice spacing; while frames b) and d) show the lattice having half period with respect to the original one.

When periodical patterns are projected or when shadow masks are used for manipulating a laser beam intensity profile, superluminescent diodes

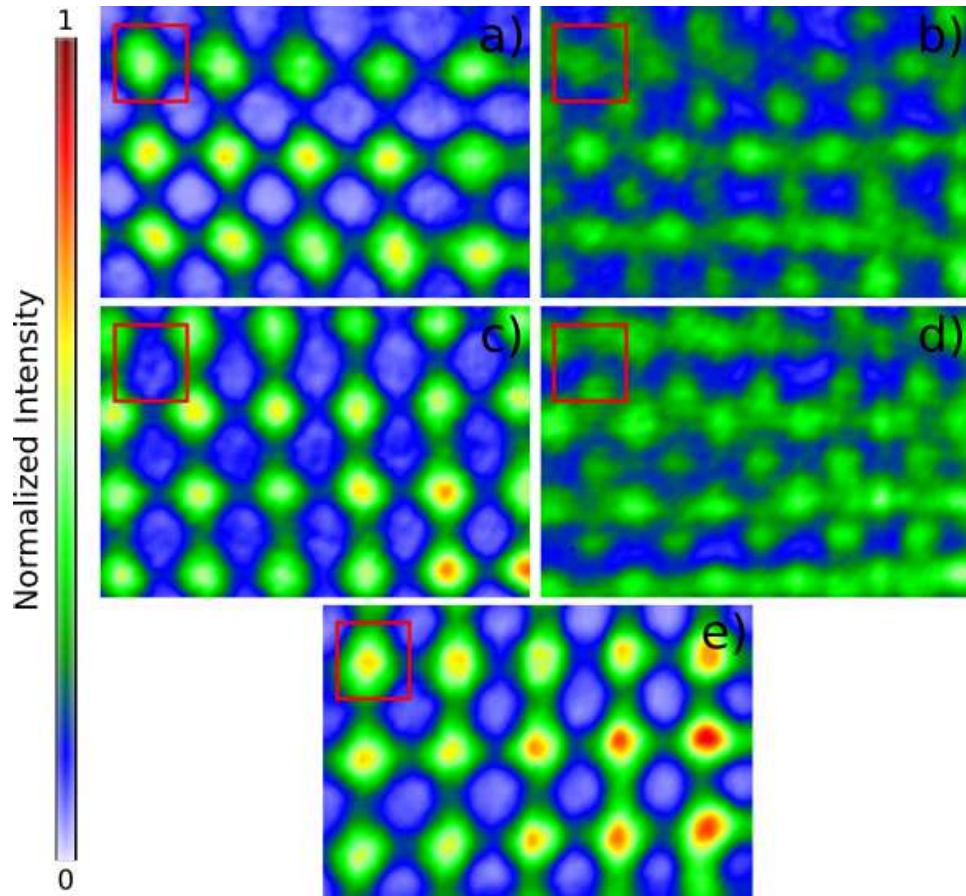


Figure 5.26: Images of the Talbot carpet recorded at different distances d , expressed in terms of L_T : a) $d = 0$, b) $d = 0.25 L_T$, c) $d = 0.5 L_T$, d) $d = 0.75 L_T$ and e) $d = L_T$.

(SLD) – characterized by a low temporal coherence – are often employed as light sources in order to destroy the undesired Talbot effect and other spurious interference effects [28].

Anyway, if the spatial and temporal coherences of the employed source could be preserved, interesting applications based on the Talbot effect could be achieved: e. g. it could be exploited to trap atoms in a normal plane with respect to the laser propagation [60]. If a 2-D sinusoidal-like pattern were displayed on the DMD and projected by an objective in parallel to the table normal, ultra-cold atoms might be confined in a periodical potential and trapped against the gravity. This sets quite strong requirements on the quality of the optical system implemented and on the amount of the available laser power. Anyway, this work demonstrates that a DMD could be successfully employed also in experiments where Talbot-like features are meant to be exploited.

Chapter 6

Dynamic patterns applications in Atomic Physics

A collection of several images, slightly different from each other, can be organized in sorted sequences, loaded into the DMD Memory Board and projected with a very high frame rate in order to simulate the pattern motion, as in a film. Through this method, moving images and dynamic patterns can be created, paving the way to new possible applications of the DMD in atomic physics experiments.

In the first section of this chapter, the realization of the stimulated Raman effect and Bragg scattering with a DMD is investigated. In the second section, instead, the possibility of implementing a quantum register and two-qubits quantum gates is studied.

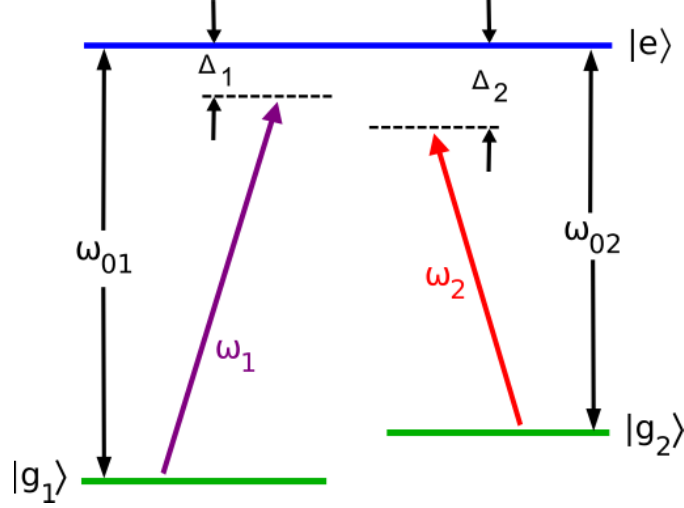
6.1 Stimulated Raman effect and Bragg scattering with a DMD

The stimulated Raman effect is a two-photon process in which a photon is absorbed by an atom and a second one is created by stimulated emission, changing the internal atomic state.

In order to study this effect, it can be useful to consider an atomic energy levels structure in Λ -configuration (see Fig. 6.1): it is a three-level system where two ground states – $|g_1\rangle$ and $|g_2\rangle$ – are both coupled to an excited state $|e\rangle$ by two electromagnetic radiations characterized by two different angular frequencies – ω_1 and ω_2 – far-off-resonant to the excited state, i. e. population transfer to $|e\rangle$ and spontaneous emission are explicitly neglected in this treatment.

Generally, through the stimulated Raman effect, the atomic population can be driven between $|g_1\rangle$ and $|g_2\rangle$ as in an effective two-levels system¹.

¹In classical non-linear optics picture, this process can be thought as if two waves


 Figure 6.1: Atomic Λ -system energy levels diagram.

The stimulated Raman effect is based on the interaction between the atomic system and two laser beams which form – in the intersection zone, where the interaction can occur – an interference pattern depending on the angular frequencies and the wave-vectors differences of the two optical fields (see Fig. 1.4 in Sec. 1.3).

By expressing as follows the electric fields of the optical radiations

$$\begin{aligned}\mathbf{E}_1(\mathbf{r}, t) &= \varepsilon_1 E_{01} e^{i(\mathbf{k}_1 \cdot \mathbf{r} - \omega_1 t)} \\ \mathbf{E}_2(\mathbf{r}, t) &= \varepsilon_2 E_{02} e^{i(\mathbf{k}_2 \cdot \mathbf{r} - \omega_2 t)}\end{aligned}\quad (6.1)$$

the interference pattern can be calculated as

$$\begin{aligned}I(\mathbf{r}, t) &= \frac{c\varepsilon_0}{2} |\mathbf{E}_1 + \mathbf{E}_2|^2 \\ &\sim E_0^2 \cos^2(\Delta\mathbf{k} \cdot \mathbf{r} - \Delta\omega t)\end{aligned}\quad (6.2)$$

where in the last passage the two optical waves are supposed to have the same polarization $\varepsilon_1 = \varepsilon_2 = \varepsilon$ and amplitude $E_{01} = E_{02} = E_0$. In the second step, the following notation has been used

$$\Delta\mathbf{k} = \frac{\mathbf{k}_1 - \mathbf{k}_2}{2} \quad \Delta\omega = \frac{\omega_1 - \omega_2}{2} = \frac{\Delta E}{\hbar}$$

hitting the same atoms were mixed together by non-linearity effects, leading to an effective wave at the difference frequency of the two initial waves, which would drives the atomic transition between the ground states.

$\Delta \mathbf{k}$ and $\hbar \Delta \omega$ are the momentum and energy transferred to the system, respectively².

The Eq. 6.2 describes an interference pattern formed by linear fringes separated by a distance $d = \pi \Delta \mathbf{k}$ which flow with velocity

$$v = \Delta \omega / |\Delta \mathbf{k}| = \frac{\Delta E}{\hbar \Delta \mathbf{k}} \quad (6.3)$$

The hamiltonians describing the atomic system and the interaction between the atoms and the overall external field $\mathbf{E}(\mathbf{r}, t) = \mathbf{E}_1(\mathbf{r}, t) + \mathbf{E}_2(\mathbf{r}, t)$ are respectively

$$\begin{aligned} \mathcal{H}_A &= \frac{p^2}{2m} - \hbar \omega_{01} |g_1\rangle \langle g_1| - \hbar \omega_{02} |g_2\rangle \langle g_2| \\ \mathcal{H}_{AF} &= -\hat{\mathbf{d}}^+ \cdot \mathbf{E}^- - \hat{\mathbf{d}}^- \cdot \mathbf{E}^+ \end{aligned} \quad (6.4)$$

where in the last expression the external field $\mathbf{E}(\mathbf{r}, t)$ and the electric dipole momentum operator $\hat{\mathbf{d}} = -e\hat{\mathbf{r}}$ have been separated into their positive- and negative-rotating components. Moreover the dipole and the Rotating-Wave approximations have been applied (see Sec. 1.2).

After some mathematical manipulation – reported in details in Steck, [63], for instance –, the effective Raman hamiltonian can be found. It is given by

$$\begin{aligned} \mathcal{H}_R &= \frac{p^2}{2m} + \hbar (\Delta_1 + \omega_{AC1}) |g_1\rangle \langle g_1| + \hbar (\Delta_2 + \omega_{AC2}) |g_2\rangle \langle g_2| \\ &+ \frac{\hbar \Omega_R}{2} (e^{i(\mathbf{k}_2 - \mathbf{k}_1) \cdot \mathbf{r}} |g_1\rangle \langle g_2| + e^{i(\mathbf{k}_1 - \mathbf{k}_2) \cdot \mathbf{r}} |g_2\rangle \langle g_1|) \end{aligned} \quad (6.5)$$

where

$$\Omega_R = \frac{\Omega_1 \Omega_2}{2\Delta} \quad (6.6)$$

is the two-photon Rabi frequency, Δ_i is the detuning between the virtual and the excited states, $\Delta = (\Delta_1 + \Delta_2)/2$ and Ω_i is the Rabi frequency describing the coupling between the external field with angular frequency ω_i and the transition $|g_i\rangle - |e\rangle$. Instead,

$$\omega_{ACi} = \frac{\Omega_i^2}{4\Delta} \quad (6.7)$$

is the Stark shift of the energy levels.

It is interesting to remember that $\exp(-i\mathbf{k} \cdot \mathbf{r})$ is the momentum-shift operator, therefore from Eq. 6.5 one can deduce that a transition between

²The maximum and minimum values assumed by $\Delta \mathbf{k}$ and $\hbar \Delta \omega$ depend on the kind of dynamic pattern projected by the DMD.

the two ground states is associated with a momentum kick given by the sum of two photon-recoil momenta.

In the resonance case, the following formula for the "resonance Raman condition" can be derived

$$\Delta_R = 4\omega_R \frac{p_{\parallel} + \hbar \delta k}{\hbar \delta k} + (\Delta_2 - \Delta_1) + (\omega_{AC1} - \omega_{AC1}) = 0 \quad (6.8)$$

where p_{\parallel} is the projection of the the momentum \mathbf{p} along the direction of $\delta\mathbf{k}$ and

$$\hbar \omega_R = \frac{\hbar^2 \delta\mathbf{k}^2}{2m} \quad (6.9)$$

is the Raman recoil energy, which is the kinetic energy of an atom having momentum $\hbar \delta k / 2$.

Thus, the initial system is reduced to a two-levels one with an energy splitting of $\hbar\Delta_R$, coupled with an external optical field having strength $\hbar\Omega_R/2$.

As seen previously, in order to perform a stimulated Raman or a Bragg scattering process³, the atomic system should interact with a moving periodical pattern. This can be represented by the density-plot of the 1-D function reported in Eq. 6.12, which is characterized by the distance λ_P between two adjacent maxima and by the corresponding number of pixels (referred to as "micromirrors per period" or MPP, from now on) needed to create a single period of the pattern.

Such density-plots can be gathered and sorted in sequences where each frame represents the same interference pattern spatially shifted to the same direction by a constant length s . Clearly, these sequences can be loaded into the DMD Memory Board and then projected in order to simulate the presence of two laser beams through their interference.

Due to the periodicity of the interference patterns, the period length λ_P , the number N of frames in a sequence and the shifting length s are bounded among them by the relation $N \cdot s = \lambda_P$. Therefore, depending on λ_P , N should be carefully chosen: actually, a low number of frames would request a high spatial shifting of the patterns, causing a "step motion" of the figure; in the same way, a high N has disadvantages as well in terms of excitation energy transfer, later discussed. The maximum N is bounded by the smallest shift performable, corresponding to a DMD micromirror size, while the maximum shifting velocity is limited by the maximum refresh rate

³The simulated Raman effect can be actually seen as a Bragg scattering process of first order.

of the images on the device screen.

Initially, a static interference figure were supposed to be projected by the DMD: the obtained intensity profile modulation would correspond to a standing wave, the same created by a couple of laser beams with the equal angular frequency ($\Delta\omega = 0$). Since $\lambda_P = \pi/\Delta k$ is the wavelength of the wave displayed on the DMD, the distance between two adjacent maxima is related to the momentum kick that can be transmitted. In general, the accessible range of wave-vectors Δk is bound to the diffraction limit of the optical system, the DMD dimensions and the MPP. The smallest momentum is achieved by the highest λ_P , equal to the whole DMD horizontal dimension in the "DMD frame". Instead, the highest momentum is given by the smallest pattern wavelength, bounded by the largest between the diffraction limit of the experimental set-up and the mirror size (after the demagnification). For the optical systems considered, the smallest attainable λ_P is caused by the diffraction limit.

Hence, taking into account the projection system with an overall demagnification of 100 (the one implemented during this work, see Sec. 2.2), the range of the possible wave-vectors is ($22 \text{ nm}^{-1} - 3.3 \text{ }\mu\text{m}^{-1}$). Instead, for the objective 80X / 0.7 N.A. (that will be used for this aim in future) implemented in an optical system having a demagnification⁴ of 240, the momenta range is ($54 \text{ nm}^{-1} - 4.6 \text{ }\mu\text{m}^{-1}$). In both cases, the iris has been considered wide open.

Regarding the excitation energies, the energy ΔE is carried by a moving interference pattern and is equal to $\hbar \Delta\omega$. The energy transfer, for a certain DMD refresh rate R (its maximum value is 22,727 Hz for the DMD in use, see sec. 2.1), is given by

$$\Delta E = \hbar \Delta k \cdot s \cdot R \quad (6.10)$$

where s is the shifting length made by the pattern in each frame. Manipulating the definitions of the variables, the previous relation can be rewritten as follows in order to evaluate the excitation energy (in frequency unit)

$$\frac{\Delta E}{h} = \frac{R}{N} \quad (6.11)$$

As said previously, the frames number N of a sequence can not be arbitrarily chosen, but is related to the λ_P of the pattern displayed due to its periodicity. A high λ_P requests a high number of frames in order to keep low the value of s and so obtain a smooth movement of the pattern on the DMD

⁴In this set-up, the telescope 1 : 3 has a diffraction limit of $8.9 \text{ }\mu\text{m}$ with the iris completely open; whereas the objective has a diffraction limit of $53 \text{ }\mu\text{m}$ in the back-focal plane. The minimum length revolvable in the "DMD frame" is $159 \text{ }\mu\text{m}$, corresponding to 12 pixels. See Sec. 2.2.

screen, limiting the transferable ΔE .

Regarding the experimental set-up implemented during this work, the periodical pattern which provides the bigger Δk has a period of 7 pixels (100X system), that is the smaller λ_P allowed by the diffraction limit (see Sec. 2.4). Therefore, moving this pattern with a shifting length equal to one micromirror size would demand a sequence of 7 frames. Due to the diffraction limit, the value of s could be higher (so the frames number lower), but not excessively in order to avoid the "step motion" of the pattern. In the case of the seven images sequence, the maximum energy transfer would be about $3.2 \text{ kHz} \cdot \hbar$. For the 240X system (12 frames), the maximum energy is about $1.9 \text{ kHz} \cdot \hbar$.

On the other side, in order to transmit the smallest momentum kick, it is necessary to create a pattern with the maximum possible λ_P , that is equal to 14 mm in the "DMD frame". In this case, it is not convenient to create a sequence having s equal to one micromirror size, because a large N would be requested and the maximum energy transmittable would be small. Therefore a lower N should be chosen with the constraint of projecting a smoothly moving pattern. Reasonably this number⁵ could be 20, so the maximum energy would be about 1.1 kHz , assumed to be the same for the 240X system.

Regardless to the momentum kick, the parameters N and R can be adjusted to achieve small $\Delta\omega$ without losses of the pattern motion quality (or minimizing it).

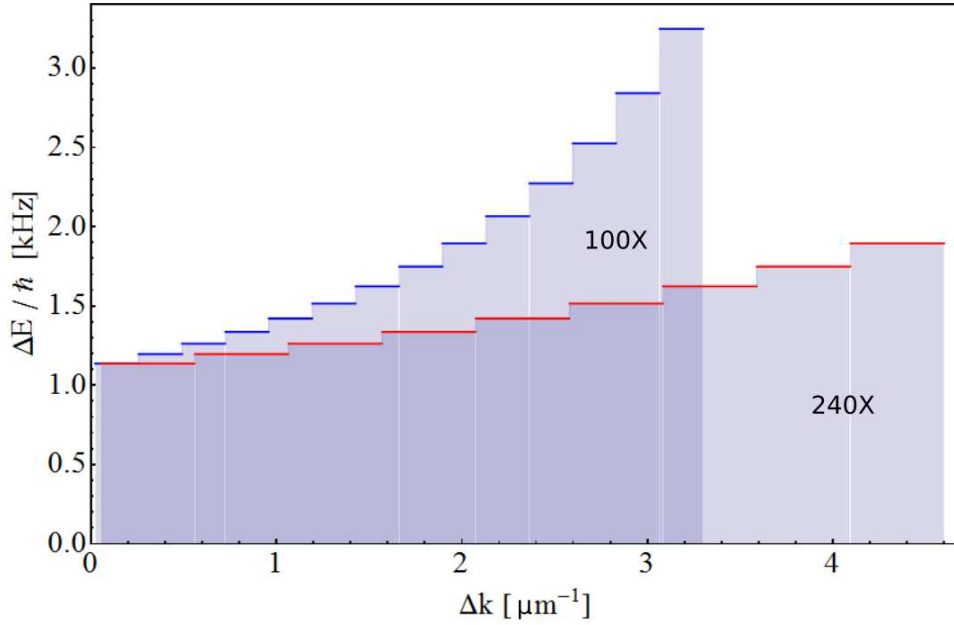
Tab. 6.1 resumes the accessible momentum and energy ranges for the experimental set-up implemented during this work and the future optical system. In Fig. 6.2 the $\Delta k : \Delta\omega$ accessible region is shown.

| System | 100X | 240X |
|-------------------------------|---|---|
| Diffraction limit (DMD frame) | $92.5 \mu\text{m}$ 7 pixels | $159 \mu\text{m}$ 12 pixels |
| Δk range | $(22 \text{ nm}^{-1} - 3.3 \mu\text{m}^{-1})$ | $(54 \text{ nm}^{-1} - 4.6 \mu\text{m}^{-1})$ |
| Max $\Delta\nu$ | $(1.1 - 3.2) \text{ kHz}$ | $(1.1 - 1.9) \text{ kHz}$ |

Table 6.1: Bragg scattering accessible momentum and energy ranges for the two optical systems analysed.

The interference patterns described above can be achieved by the DMD controlled by "DMD Easy". The device control program developed during this work is able to create a collection of images representing the density-plots of the function

⁵A better estimation would require the direct observation of this pattern effects on the atoms.


 Figure 6.2: Accessible $\Delta k - \Delta\omega$ region for Bragg scattering.

$$\text{Int}[x, n] = \sin^2(\Delta k(x + n s)) \quad (6.12)$$

where $\Delta k = \pi/\lambda_P$ is the momentum related the interference pattern, s is the shifting length and n is the considered frame number ($0 \leq n < N$).

These images can be loaded into the DMD Board Memory and projected in sequence in order to create a moving interference pattern.

Fig. 6.3 shows four frames of a 16 images sequence created to test the dynamic properties of the DMD and to achieve the moving interference figure. Comparing the fringes position, the effect of the shifting can be noticed. The fringes number is 18, therefore about 57 micromirrors are dedicated to create a single fringe. This allows for the transmission a momentum kick to the atoms equal to about $0.4 \mu\text{m}^{-1}$ with the optical system having an overall demagnification of 100 or equal to $0.97 \mu\text{m}^{-1}$ for a demagnification of 240.

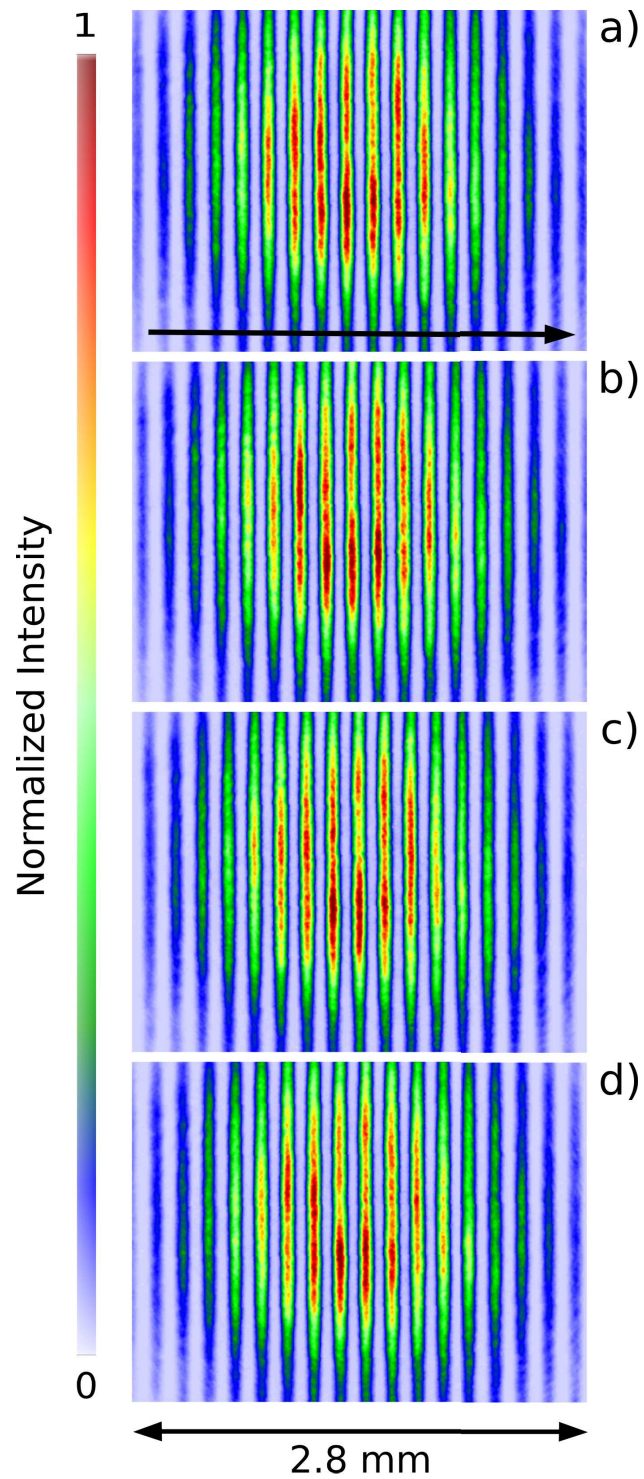


Figure 6.3: Frames from a sequence for Bragg scattering formed by 16 images. The frames are the fourth, the eighth, the twelfth and the sixteenth of the sequence. The interference pattern flows from the left to the right. The overall pattern length is meant on the CCD 1 screen.

6.2 DMD in quantum computing

Quantum computing, which gathers the notions from classical information theory, computer science and quantum physics, mainly studies theoretical computation systems that, exploiting quantum-mechanical effects such as superposition and entanglement, perform operations on data. As classical digital computers work on data stored into binary digits (bits) which can only assume values equal to 0 or 1, quantum computers use "qubits" to encode data. Regardless of the system nature, a qubit is a quantum object which is able to represent the Boolean states 0 and 1 with a pair of normalised and mutually orthogonal quantum states, tagged as $|0\rangle$ and $|1\rangle$. These two states form a computational basis and any other pure state of the qubit can be written as a superposition:

$$|\psi\rangle = \alpha|0\rangle + \beta|1\rangle \quad (6.13)$$

with α and β complex numbers such that $|\alpha|^2 + |\beta|^2 = 1$.

A qubit can be represented by different systems: for instance, polarized photons, nuclear spins or atoms. For Ytterbium atoms, the two states of the qubits can be implemented thanks to the metastable state 3P_0 , which can be considered stable during the experimental cycles and, therefore, seen as a "second" ground state (see Sec. 1.1).

A collection of n qubits is called "quantum register" (of size n). Information can be stored in each of these register components which can be individually addressed or modified.

Any kind of manipulation on qubits can be represented by unitary operations. A "quantum logic gate" is a generic device achieving an unitary operation on selected qubits in a certain period of time. A series of quantum logic gates performing computational steps, ordered or synchronized in time, constitutes a "quantum network". Examples of quantum logic gates working on a single qubit are the Hadamard gate and the phase gate, described in details in Ekert, Hayden, and Inamori, [21]. Any kind of universal operation made on a single qubit can be expressed in terms of these two gates.

A quantum register could be implemented by a sample of ultra-cold atoms trapped in a periodical arrangement of optical dipole potentials, such as an optical lattice. If the parameters of this system (atoms number and lattice site depth) are chosen carefully, the Mott insulator phase can be achieved (see Sec. 1.4) in order to localize one atom per lattice site. This regular arrangement of the atoms, along with the two stable states (with respect to the experimental time-scale) of Ytterbium, provides the basis necessary for the creation of a quantum register: actually distinguishable, coherently

stored and localized atoms which can be addressed by two different internal states can be treated as qubits.

"Cold controlled collisions" can then be exploited as basic mechanism to entangle the neutral atoms states in order to implement a two-qubit quantum gate in the system described above. A brief report of this method theoretical background is now presented. For further details, see Jaksch et al., 1999 [44].

Let two atoms – 1 and 2 – in internal states $|a\rangle_1$ and $|b\rangle_2$ – tagged "a" and "b" – be trapped in the ground states $\psi_{a,b}$ of two lattice sites described by $V_{a,b}$. Initially, at the time $t = -\tau$, the two wells are centered at the positions $\bar{\mathbf{x}}_a$ and $\bar{\mathbf{x}}_b$, far enough to avoid any interaction between the atoms. Then, the site positions are moved in order to make the atoms closer so that their wave packets overlap for a certain time. In the end, they are restored to the initial position, reached in $t = \tau$. This situation is described by the following hamiltonian

$$\mathcal{H} = \sum_{\alpha=a,b} \left[\frac{\hat{\mathbf{p}}_{\alpha}^2}{2m} + V_{\alpha}(\hat{\mathbf{x}}_{\alpha} - \bar{\mathbf{x}}_{\alpha}(t)) \right] + u_{ab}(|\hat{\mathbf{x}}_a - \hat{\mathbf{x}}_b|) \quad (6.14)$$

where $\hat{\mathbf{p}}_{\alpha}$ and $\hat{\mathbf{x}}_{\alpha}$ are the position and momentum operators, respectively, $V_{\alpha}(\hat{\mathbf{x}}_{\alpha} - \bar{\mathbf{x}}_{\alpha}(t))$ describes the trap potentials motion and u_{ab} is the atom-atom interaction term.

Therefore, the transformation implemented would be

$$\begin{aligned} \psi_a(\hat{\mathbf{x}}_a - \bar{\mathbf{x}}_a(t)) \psi_b(\hat{\mathbf{x}}_b - \bar{\mathbf{x}}_b(t)) &\rightarrow \\ \rightarrow e^{-i\phi} \psi_a(\hat{\mathbf{x}}_a - \bar{\mathbf{x}}_a(t)) \times \psi_b(\hat{\mathbf{x}}_b - \bar{\mathbf{x}}_b(t)) &\end{aligned} \quad (6.15)$$

where the atoms stay in the trapping potential ground state ψ and do not change their internal state (adiabatic limit). The contribution of the interaction is contained in the phase ϕ . In the adiabatic limit and in absence of interaction ($u_{ab} = 0$), the "kinetic phase" can be evaluated as follows

$$\phi_{a,b} = \frac{m}{2\hbar} \int_{-\tau}^{\tau} \dot{\mathbf{x}}_{a,b}(t)^2 dt \quad (6.16)$$

Whereas, with the presence of the interaction, the additional contribution to the phase ϕ can be calculated as

$$\phi_{ab} = \frac{1}{\hbar} \int_{-\tau}^{\tau} \Delta E(t) dt \quad (6.17)$$

where $\Delta E(t)$ is the time-dependent kinetic energy shift due to the atom-atom interaction, expressed by

$$\Delta E(t) = \frac{4\pi a_s \hbar^2}{m} \int \prod_{\alpha=a,b} |\psi_{\alpha}(\hat{\mathbf{x}}_{\alpha} - \bar{\mathbf{x}}_{\alpha}(t))| \quad (6.18)$$

with a_s the s-wave scattering length.

In this way, the cold controlled collisions can be used as a coherent mechanism in order to induce a phase shift in two-atoms collisions. This method can be exploited to implement a quantum logic gate.

Actually, for example, if the collision were possible only if the first atom 1 is in the $|a\rangle_1$ state and the second in the $|b\rangle_2$, the possible results – depending on the initial states – of the described process would be

$$\begin{aligned}
 |a\rangle_1|a\rangle_2 &\rightarrow e^{-2i\phi_a} |a\rangle_1|a\rangle_2 \\
 |a\rangle_1|b\rangle_2 &\rightarrow e^{-i(\phi_a+\phi_b+\phi_{ab})} |a\rangle_1|b\rangle_2 \\
 |b\rangle_1|a\rangle_2 &\rightarrow e^{-i(\phi_a+\phi_b)} |b\rangle_1|a\rangle_2 \\
 |b\rangle_1|b\rangle_2 &\rightarrow e^{-2i\phi_b} |b\rangle_1|b\rangle_2
 \end{aligned} \tag{6.19}$$

where the motional states do not vary during the process. Eqs. 6.19 represent the "truth table" of the quantum gate implemented. A truth table is a matrix containing all the possible outputs of the gate depending on the initial parameters setting.

In order to create this kind of two-qubit quantum gates, a dynamic lattice is requested: actually, at a certain time, two adjacent sites have to be able to get closer, merge and separate again. This moving pattern can be obtained with the aid of the DMD controlled by "DMD Easy", which can generate a sequence of frames that simulates the motion of the desired lattice. In each frame, the density-plot of the function Eq. 6.20 is plotted.

$$G(x, y) = \frac{1}{2} \left(A \sin^2\left(\frac{\pi}{2\lambda_P} x\right) + (1 - A) \sin^2\left(\frac{\pi}{\lambda_P} x\right) + \sin^2\left(\frac{\pi}{\lambda_P} y\right) \right) \tag{6.20}$$

Here the factor A can vary in the range $(0, 1)$, adjusting the mixing between the first two terms of the function "G".

Fig. 6.4 shows some examples extracted from a sequence of twenty frames where the parameter A is varied from 0 (standard lattice) to 1 (lattice with couples of sites are "melted" together) at step of 0.05 for each plot. The projection time of each images can be chosen via "DMD Easy" and it should be large enough to allow for the adiabatic approximation. At the end of the sequence projection, the lattice sites are overlapped in couples. The projection of the same sequence with the frames order inverted will bring the system back to the starting conditions.

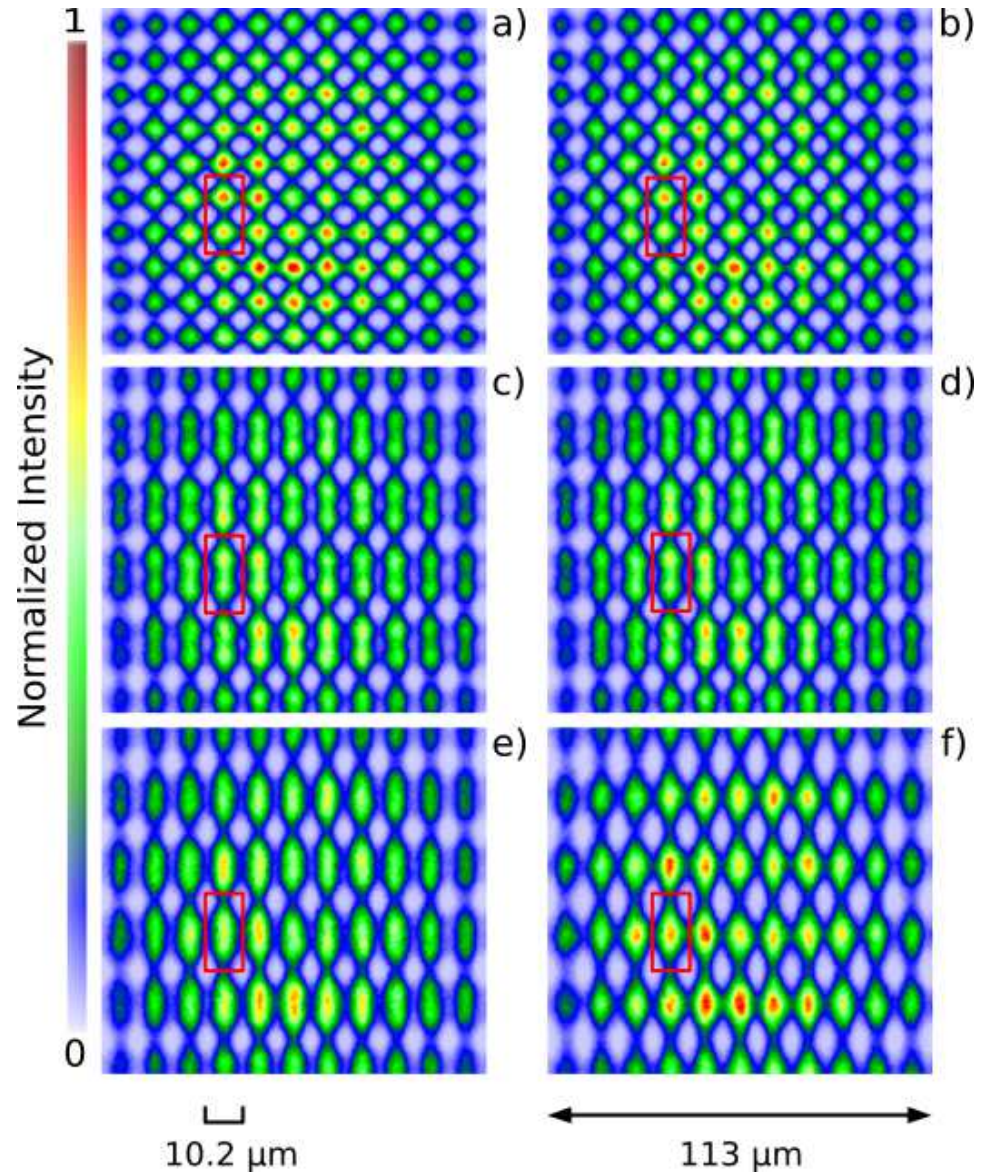


Figure 6.4: Frames from a "Gate" sequence. The value assumed by A are: 0 in a), 0.2 in b), 0.4 in c), 0.6 in d), 0.8 in e), 1 in f). The area delimited in red on the frames shows the evolution of a single quantum gate and the involved lattice sites. The reported lengths are meant on the CCD 1 screen.

Summary and outlook

This thesis work analyses and investigates the possibility to employ a Digital Micromirror Device in atomic physics experiments, where the capability to control atoms through optical potentials is typically requested. Though many optical potentials have been implemented by exploiting interference of multiple laser beams, a tool able to increase the degree of control, both static and dynamic, of such potentials would be highly desirable. Actually, a DMD is able to manipulate the intensity profile of an incident laser beam in arbitrary shapes, providing a powerful tool to create arbitrary optical potentials in order to trap atoms, control their motion or address their internal state. Moreover, the DMD offers a simple solution to generate moving and dynamic potentials, still maintaining the freedom of shaping the intensity profile in any form.

During this work, an experimental set-up has been implemented in order to characterize the device and its properties (e. g. grating behaviour, effects on the laser polarization and timing features).

Several dithering algorithms have been taken into account for obtaining images to be loaded into the DMD Memory Board. The "Serpentine Floyd-Steinberg" error diffusion algorithm has been proven to be the best method for digitizing the initial image without remarkable loss in terms of visual fidelity.

"DMD Easy", a program provided with a Graphic User Interface, has been created and developed entirely throughout this work in order to control the device and its timing properties. Beyond the possibility of digitizing raster images, organizing the loaded frames in sorted sequences and setting the projection timing features, "DMD Easy" is able to perform a feedback process on the projected patterns for correcting the defects due to the optical system and the original shape of the laser beam intensity profile.

Static patterns, which play a major role in atomic physics applications, have been produced and studied with the aid of physical parameters defined during this work. For instance, Flat-tops and lattices have been projected and corrected via the feedback algorithm. The former can be used in order to create a box-like optical potential, while the latter offers the possibility to build a periodical arrangement of trap potentials.

By using a coherent laser source, the Talbot effect generated by displaying

periodical patterns has been observed. Generally, this effect is eliminated by employing superluminescent diodes as light sources. Nevertheless, it could be exploited in order to achieve at the same time, beyond a trapping lattice, a confinement of the atoms against the gravity without using any other trapping potential.

Several dynamic patterns have been tested as well, along with their possible applications in atomic physics experiments. Thanks to the high degree of control on timing and shape of the beam that is delivered by the DMD, stimulated Raman effect and Bragg scattering could be performed using this system. The energies and momentum kicks accessible ranges are studied as a function of the device features.

The possibility to exploit a DMD in the field of quantum computation has been studied as well. Actually, ultra-cold atoms trapped in a deep lattice can simulate a quantum register. Moreover, dynamic lattices, suitable in order to create two (or more) qubits quantum gates, have been implemented by merging adiabatically the lattice sites at couples and then bringing them back to the initial state, a logic gate can be achieved where the atoms states (which contain the encoded information) are modified on the basis of the tunable atom-atom interaction.

In conclusion, this master thesis work proves that Digital Micromirror Devices are powerful and versatile tools which could be integrated in actual atomic physics experiments, providing an enhanced degree of control in the manipulation of atoms through the projection of arbitrary optical potentials.

Bibliography

Articles and On-line Publications

- [1] C. S. Adams, M. Sigel, and J. Mlynek. *Atom Optics*. Tech. rep. Phys. Rep., 1994.
- [2] B. P. Anderson and M. A. Kasevich. “Macroscopic quantum interference from atomic tunnel arrays.” In: *Science* (Nov. 1998).
- [3] M. H. Anderson et al. “Observation of Bose-Einstein condensation in a dilute atomic vapor”. In: *Science* (1995).
- [4] E. Arimondo, H. Lev, and T. Oka. “Deflection of a Na beam by resonant standing-wave radiation”. In: *Physical review Letters* (1979).
- [5] A. Ashkin et al. “Observation of a single-beam gradient force optical trap for dielectric particles”. In: *Optical letters* 11.5 (May 1986).
- [6] A. Aspect et al. “Laser cooling below the one-photon recoil energy by velocity-selective coherent population trapping”. In: *Physical Review Letters* (1988).
- [9] M. P. Bradley et al. “Penning trap measurements of the masses of ^{133}Cs , $^{87,85}\text{Rb}$ and ^{23}Na with uncertainties < 0.2 ppb”. In: *Physical Review Letters* (1999).
- [10] S. Burger et al. “Superfluid and dissipative dynamics of a Bose-Einstein condensate in a periodic optical potential”. In: *Physical Review Letters* (May 2001).
- [12] William B. Case et al. “Realization of optical carpets in the Talbot and Talbot-Lau configurations”. In: *Optical society of America* (2009).
- [13] F. S. Cataliotti et al. “Josephson junction arrays with Bose-Einstein condensates”. In: *Science* (2001).
- [15] P. Cladé, E. de Mirandes, M. Cadoret, et al. “Determination of fine structure constant based on Bloch oscillations of ultracold atoms in a vertical optical lattice”. In: *Physical Review Letters* (2006).
- [17] M. B. Dahan et al. “Bloch oscillations of atoms in an optical potential”. In: *Physical Review Letters* (1996).
- [18] Andrew J. Daley et al. “Quantum Computing with Alkaline-Earth-Metal Atoms”. In: *Physical Review Letters* (2008).
- [19] Dana Dudley, Walter Duncan, and John Slaughter. “Emerging Digital Micromirror Device (DMD) Applications”. In: *SPIE Proceedings* 4985 (2003).
- [23] R. F. Feynman. “Simulating physics with computers”. In: *International journal of theoretical physics* (1982).

-
- [24] R. Floyd and L. Steinberg. “Adaptive algorithm for spatial gray scale”. In: *Proc. Society for information display* 17.2 (1976).
- [25] Marco Frasca. “A modern review of the two-level approximation”. In: *Annals of Physics* 306 (2008).
- [26] Takeshi Fukuhara et al. “Quantum dynamics of a mobile spin impurity”. In: *Nature physics* (2013).
- [27] Fabrice Gerbier and Jean Dalibard. “Gauge fields for ultracold atoms in optical superlattices”. In: *New Journal of Physics* (2010).
- [29] D. M. Giltner, R. W. McGowan, and S. A. Lee. “Atom interferometer based on Bragg scattering from standing light waves”. In: *Physical Review Letters* (1995).
- [30] ViALUX GmbH. *ALP-4: Application Programming Interface*. 2005.
- [31] Phillip L. Gould, George A. Ruff, and David E. Pritchard. “Diffraction of atoms by light: the near-resonant Kapitza-Dirac effect”. In: *Physical review letters* 56.8 (Feb. 1986).
- [33] Rudolf Grimm and Matthias Weidemüller. “Optical dipole traps for neutral atoms”. In: *Adv. At. Mol. Opt. Phys* (2000).
- [34] V.A. Grinchuk, E. F. Kuzin, M. L. Nagaeva, et al. “Scattering of an atomic beam by a short light pulse”. In: *Physics Letters A* (1981).
- [35] G. Grynberg et al. “Quantized motion of cold cesium atoms in two- and three-dimensional optical potentials”. In: *Physical Review Letters* (1993).
- [36] Li-Chung Ha et al. “Roton-maxon excitation spectrum of Bose condensates in a shaken optical lattice”. In: *Physical Review Letters* (2015).
- [37] A. Hemmerich and T. W. Hänsch. “Two-dimensional atomic crystal bound by light”. In: *Physical Review Letters* (1993).
- [38] A. Hemmerich et al. “Trapping atoms in a dark optical lattice”. In: *Physical Review Letters* (1995).
- [40] Texas Instruments. “DLP 0.7 XGA 2xLVDS Type A DMD”. In: *DLPS026B* (2013).
- [41] Texas Instruments. “DLP Discovery 4100 Chipset Data Sheet”. In: *DLPU008A* (2013).
- [42] Texas Instruments. “Using Lasers with DLP DMD technology”. In: *TI DN 2509927* (2008).
- [43] D. Jaksch et al. “Cold Bosonic Atoms in Optical Lattices”. In: *Phys. Rev. Lett.* 81 (15 Oct. 1998), pp. 3108–3111.
- [44] D. Jaksch et al. “Entanglement of Atoms via Cold Controlled Collisions”. In: *Phys. Rev. Lett.* 82 (9 Mar. 1999), pp. 1975–1978.

-
- [45] O. S. Jessen et al. “Observation of quantized motion of rb atoms in an optical field”. In: *Physical Review Letters* (1992).
- [46] M. Kasevich and S. Chu. “Laser cooling below a photon recoil with three-level atoms”. In: *Physical Review Letters* (1992).
- [47] Goldy Katal, Nelofar Tyagi, and Ashish Joshi. “Digital Light Processing and its Future Applications”. In: *International Journal of Scientific and Research Publications* 3.4 (Apr. 2013).
- [48] Sebastian Krinner et al. “Observation of quantized conductance in neutral matter”. In: *Nature* 517 (7532 Jan. 1999).
- [49] Benjamin Lee. “DMD 101: Introduction to Digital Micromirror Device (DMD) Technology”. In: *Texas Instruments Application Report* (2013).
- [50] N. D. Lemke et al. “Spin-1/2 Optical Lattice Clock”. In: *Phys. Rev. Lett.* 103 (6 June 2009), p. 063001.
- [52] Jinyang Liang et al. “1.5% root-mean-square flat-intensity laser beam formed using a binary-amplitude spatial light modulator”. In: *Applied Optics* 48.10 (Apr. 2009).
- [53] S. Lloyd. “Universal quantum simulator”. In: *Science* (1996).
- [54] P. J. Martin et al. “Bragg scattering of atoms from a standing light wave”. In: *Physical Review Letters* (1988).
- [55] N Masuhara et al. “Evaporative cooling of spin-polarized atomic hydrogen”. In: *Physical Review Letters* (1988).
- [56] O. Morsch et al. “Bloch oscillations and mean-field effects of bose-einstein condensates in 1d optical lattices”. In: *Physical Review Letters* (2001).
- [57] E. Moskowicz et al. “Diffraction of an atomic beam by standing-wave radiation”. In: *Physical Review Letters* (1983).
- [60] Rafael Piestun et al. “3-D interferometric optical tweezers using a single spatial light modulator”. In: *Optical Society of America* (2005).
- [61] N. Poli et al. “Frequency evaluation of the doubly forbidden $^1S_0 \rightarrow ^3P_0$ transition in bosonic ^{174}Yb ”. In: *Phys. Rev. A* 77 (5 May 2008), p. 050501.
- [62] E. M. Rasel, M. K. Oberthaler, H. Batelaan, et al. “Atom wave interferometry with diffraction grating of lights”. In: *Physical Review Letters* (1995).
- [64] Robert Ulichney. “A Review of Halftoning Techniques”. In: *SPIE* 3963 (2000), pp. 378–391.
- [65] P. Verkerk et al. “Dynamics and spatial order of cold cesium atoms in a periodic optical potential”. In: *Physical Review Letters* (1992).
-

-
- [66] Peixin Zhu et al. “High-resolution optical control of spatiotemporal neuronal activity patterns in zebrafish using a digital micromirror device”. In: *Nature protocols* (2012).

Books and Theses

- [7] David Bellem. “Generation of spatially and temporally varying light potentials in optical lattices”. Master thesis. Ludwig-Maximilians-Universität München, 2011.
- [8] Max Born and Emil Wolf. *Principles of Optics*. 1970.
- [11] Giacomo Cappellini. “Sviluppo di un sistema laser per la codifica di qubit su atomi degeneri di Itterbio”. Master thesis. University of Florence-LENS, 2012.
- [16] C. Cohen-Tannoudji and David Guéry-Odelin. *Advances in atomic physics*. World scientific publishing, 2011.
- [20] Roger L. Jr. Easton. “Fundamentals of Digital Image Processing”.
- [22] Fabian Etzold. “Laser Beam Shaping with a Digital Micromirror Device”. Master Thesis. Institut für Physik Johannes Gutenberg-Universität, Mainz, 2010.
- [28] Jonathon Isaiah Gillen. “The quantum gas microscope”. Harvard University, 2009.
- [32] Markus Greiner. “Ultracold quantum gases in three-dimensional optical lattice potentials”. PhD Thesis. Ludwig-Maximilians-Universität, München, 2003.
- [39] Massimo Inguscio and Leonardo Fallani. *Atomic Physics*. Ed. by Oxford University Press. 2013.
- [51] M. Lewenstein, A. Sanpera, and V. Ahufinger. *Ultracold atoms in optical lattices*. Ed. by Oxford University Press. 2012.
- [59] Guido Pagano. “Raffreddamento e intrappolamento di atomi di Itterbio”. Master thesis. University of Florence-LENS, 2011.
- [63] Daniel Adam Steck. “Quantum and Atom Optics”.

Ringraziamenti

Davvero non avrei mai immaginato che il momento di scrivere queste poche righe di ringraziamento sarebbe arrivato "così presto", eppure...

Desidero innanzitutto ringraziare il mio relatore, il Dr. Jacopo Catani, senza il quale questo lavoro molto probabilmente non avrebbe mai visto la luce. Le sue indicazioni, i suoi consigli, il suo supporto ed impegno nel seguirmi durante il percorso di ricerca sono stati preziosissimi ed irrinunciabili. Grazie mille.

Il secondo in lista non può essere altri che Giacomo, il miglior dottorando supporter-per-tesisti di sempre. La sua contagiosa simpatia unita ad una grande conoscenza della fisica, teorica e tecnica, hanno reso piacevole e stimolante il mio lavoro in laboratorio.

Ringrazio inoltre il Prof. Leonardo Fallani per avermi accolto nella sua "famiglia universitaria" e proposto di sviluppare questo argomento di tesi, l'internazionale Dr. Carlo Sias per la sua gentile disponibilità e Guido, Marco e Pietro per le loro indispensabili conoscenze tecniche.

La conclusione del lavoro di tesi magistrale, specie nel mio caso, rappresenta anche il termine di una fase molto più lunga dell'attività in laboratorio, dunque vorrei ricordare in questa sede tutti coloro che hanno reso unico ed indimenticabile il mio "periodo fiorentino".

Ringrazio la mia famiglia che sempre mi pensa e mi sostiene. I miei genitori in special modo, che mi hanno accordato la possibilità di vivere questa grande esperienza in questa incredibile città. Mia madre per la sua presenza ed il suo affetto, fondamentali e costanti, mio padre per la forza e la tranquillità che sempre mi trasmette. Ringrazio tanto anche la mia adorabile sorellina Linda, di cui proprio non saprei fare a meno.

Davvero non so come ringraziare le mie preziosissime amiche "brianzole", Silvia e Alessia. Non c'è stato un giorno in due anni e mezzo in cui non mi abbiano fatto sentire amato, importante e speciale. Con loro è tutto più bello, più semplice. Grazie di cuore. Allo stesso modo, ringrazio Deborah, collega ed amica del mio "periodo milanese", per il suo supporto incondizionato.

Ringrazio tutti i miei colleghi ed amici della facoltà di fisica, anzi... del polo! Fiorentini, pratesi, toscani e fuori-sede, tutti quanti! Sono stato fortu-

nato ad averli conosciuti e frequentati, dentro e fuori l'ambiente accademico. Abbiamo condiviso veramente tanto in questi anni e vissuto molti bellissimi momenti assieme che ricorderò sempre con affetto e commozione. Mi hanno accolto qui a Firenze facendomi sentire a casa... e non è poco! Grazie ragazzi!

Vorrei ringraziare i miei amici Claudio e Giacomo per il loro incredibile aiuto nei momenti critici e per aver condiviso con me la passione per la storia dell'arte: la fisica non è tutto!

Ringrazio tantissimo anche *mis amigas* del corso di spagnolo per l'energia ed i sorrisi che la loro compagnia e presenza mi hanno regalato, così come i miei amici Gianluca e Tommaso che, con la loro travolgente simpatia e forza d'animo, mi hanno dato la carica necessaria per affrontare questi ultimi mesi di grandi stress.

Infine desidero ringraziare tutti gli amici, nuovi o "storici" che siano, fiorentini o brianzoli, che hanno colorato i miei giorni in questa splendida città che porterò sempre nel cuore.

Grazie a tutti!